A new filter wheel architecture

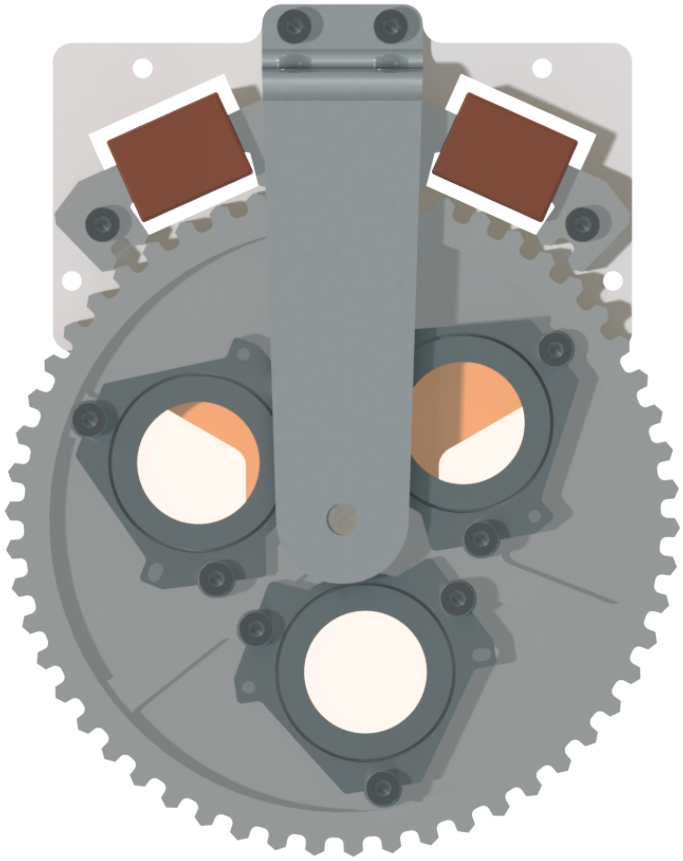

Designing a
rotating hybrid linear stepper motor
for space-based optical systems

by
Martin Kooper

2019

TU Delft TNO innovation for life

A new filter wheel architecture

Designing a rotating hybrid linear stepper motor for use in space-based optical systems

by

Martin Kooper

to obtain the degree of Master of Science
at the Delft University of Technology,
to be defended publicly on Wednesday July 31, 2019 at 13:30 AM.

Student number:	4208641	
Project duration:	October 16, 2018 – July 31, 2019	
Thesis committee:	Ir. J. Spronck	TU Delft, supervisor
	S. Kuiper	TNO, supervisor
	Dr. D. Dodou	TU Delft
	N. Saikumar	TU Delft

An electronic version of this thesis is available at `http://repository.tudelft.nl/`.

TU Delft

Preface

This is the report of my nine month long graduation project. With this projects ends a ten year long period as a student in the Netherlands, and sometimes abroad. This achievement would not have been possible without the help, tutoring and wisdom I received from many teachers over the years. To these people I would like to say thank you. For the knowlegde, guidance, wisdom and time received during this project, I would like to say thanks to my supervisors Stefan Kuiper en Jo Spronck and committee members Niranjan Saikumar and Dimitra Dodou. Thanks for reading!

Martin Kooper
Delft, July 2019

Abstract

This report presents a new filter wheel design for use in space-based optical systems. The design integrates a hybrid linear stepper motor into the wheel's rim to generate rotation, leading to a Rotating Hybrid Linear Stepper Motor (RHLSM). Unpowered this motor generates a holding force that can keep the wheel in position during system vibrations. A model was made and simulations were done to investigate motor behaviour and the effect of design parameters. A breadboard was developed to validate motor performance and investigate manufacturability. Design considerations are summarized. The report demonstrates that the RHLSM driven filter wheel is a mechanically simple, robust and compact design. The design shows great potential for a long life time and component cost reduction, and might find use in applications beside filter wheels as well.

Contents

1 Introduction

This report is about investigating a possible new actuator to rotate filter wheels in future space-based free space optical communication (FSO) terminals. This technology is part of a new generation of communication network technology that uses lasers to transmit data. Data is sent up from ground to satellites, who may relay this information to other satellites in orbit, before sending the data down to earth. FSO offers an order of magnitude higher bandwidth, uses less power, is more secure and does this at lower cost. This technology is used to create new global high speed communication networks, such as the European Data Relay System (EDRS). TNO is actively developing components used in FSO terminals to accelerate the laser communications market [16].

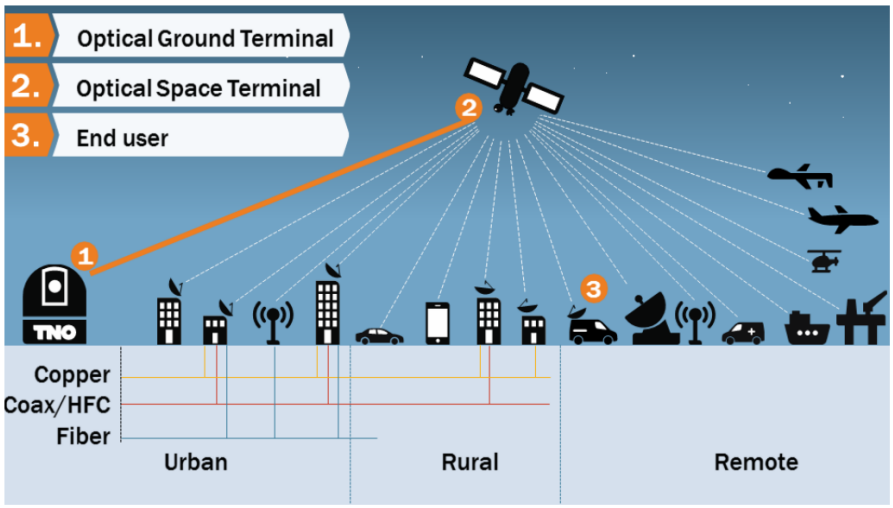

Figure 1.1: FSO network topology [16].

Figure 1.2a shows one of these FSO terminals, developed by German company Tesat-Spacecom. Part of the optical system of this terminal is a filter wheel. Its function is to insert quarter-wave plates in the laser beam's path. Filter wheels' repeatability and lifetime requirements contribute to the presently high costs for space-based FSO terminals [12]. As bringing down costs is a major development driver, TNO is developing a novel filter wheel architecture that offers better performance, longer lifetimes and lower component cost. This is achieved by integrating a hybrid linear stepper motor (HLSM) into the structure of the filter wheel, that will both rotate the wheel and hold it once positioned. This architecture is named a Rotating Hybrid Linear Stepper Motor (RHLSM). An image of the proposed architecture is shown in figure 1.2b.
The goal of this research is to design, build and test a rotating hybrid linear stepper motor, to be used in space-based filter wheels. Next to FSO terminals, filter wheels are present in all space-based optical systems. A new architecture with these benefits will therefore find application in science missions as well.

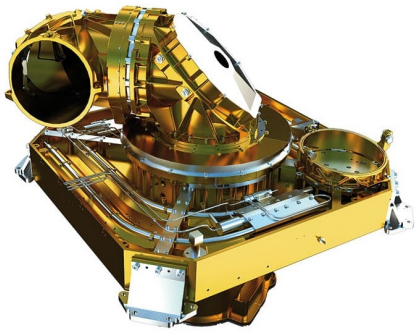

(a) FSO communication terminal.

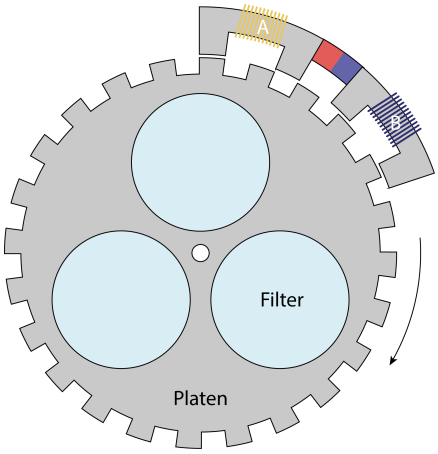

(b) RHLSM architecture.

Figure 1.2: ()a) TESAT's LCT 135 free space optical communication terminal. Its maximum communication range is 80.000Km [4]. (b) The rotating hybrid linear stepper motor (RHLSM) filter wheel concept architecture. The actuator is integrated with the wheel's structure.

The use of a HLSM to actuate filter wheels in space has several key advantages:

- **Lower component cost.**
  Current filter wheels use space-grade stepper or DC motors that cost up to 100K euro [12]. The proposed HLSM architecture has the potential for a vastly lower component cost.
- **Low mechanical complexity and faster testing and certification.**
  Filter wheels often face difficulties reaching the required service life-time, because of wearing out of mechanical contacts. The HLSM architecture has no gears or sliding contacts and only one central bearing, making this an extremely durable mechanism. Its mechanical simplicity will also make this concept easy to certify for launch and use in satellites. This will bring down the component's cost further, as these are dominated by the testing and certification of moving parts such as bearings.
- **A scalable design for a flexible design process and applicability.**
  Europe has only two suppliers that offer a limited selection of models, sizes and power ratings for space-grade stepper motors [12]. This puts actuator selection at the start of the design process, after which long testing cycles begin to verify part choice [9]. This offers zero flexibility to accomodate changing requirements. A HLSM's dimensions can easily be changed during a design process to accommodate changing needs and requirements. If the required actuation force has to go up, the motor can be made slightly bigger. This scalability also makes the motor a potential candidate for different systems, such as antennae pointing.
- **High detent force.**
  When unpowered a HLSM exerts a holding force on the freely spinning rotor, a normally unwanted phenomenon called cogging. This force acts as a brake, which will prevent spinning of the rotor during vibration. As this requires no power, a HLSM is ideal for applications where short periods of movement are alternated with periods of inactivity.

1.1. Research questions and approach

The main research question of this thesis is:

Is rotating a filter wheel using an integrated HLSM a viable system architecture for filter wheels and possibly other space-based mechanisms?

This question is broken up into several smaller questions, that will be answered separately throughout this report.

1. How does a hybrid linear stepper motor generate force?
2. Which principles generate cogging and what does that mean for our application?
3. How do the design parameters influence the motor's characteristic, specifically the actuation and cogging force?
4. What is possible a HLSM actuated filter wheel design?
5. Can this actuation concept be extended to other applications?

The approach in this research comprises four parts: a literature study, analytical modelling, finite element analysis, breadboard testing. The literature part has been reported in a separate document, but is included in the list for clarification. The results of the literature study are summarised in chapter 2.

- **Literature study**
  The literature study provides a base for all research. This includes the context and application of filter wheels, an overview of linear stepper motors, governing principles and behaviour of electric motors, and how to model these machines.
- **Analytical model**
  The analytical model gives insight into what principles govern the HLSM actuator. What do each of its components do? What behaviour do they cause? This knowledge is also required to interpret any finite element analyses results.
  Additionally, the model can be used to investigate scaling laws and the specific effect design parameters have on the motor output.
- **Finite elemtent analysis**
  The finite element analysis (FEA) helps study behaviour that the analytical model did not capture. Saturation of material and fringing of flux are hard to model phenomena, whose effect can best be investigated by a full simulation.
  FEA also lets us investigate how different tooth geometries influence the RHLSM output.
- **Breadboard**
  The main purpose of the bread is to validate the model and FEA results. Does a real motor behave as in the model and simulations? Some difference is to be expected; but the question is how much.
  Designing and constructing a breadboard will also show how easily a RHLSM motor can be manufactured. Since component cost is a key driver, this experience will be very relevant.
  Constructing a breadboard will also help in finding any hidden behaviours a HLSM might have.
  Finally the breadboard may serve as a demonstrator for potential clients.

The results from this will be used to develop a RHLSM actuated filter wheel concept design, that shows how this architecture may look in practice.

2

The rotating hybrid linear stepper motor concept

2.1. Application of filter wheels and the proposed new actuator principle

In a space-based FSO terminal, the filter wheel's function is to insert quarter-wave plates into the laser beam's path. This allows separating the up- and downlink channel [15]. Next to FSO terminals, filter wheels are used in space science missions such as NASA's James Webb telescope, ESA's Euclid mission and ExoMars Rover [3] , [10], [5]. As FSO terminals are in a mostly conceptual phase, these science missions serve as an example of filter wheel construction.

Generally a filter wheel consists of a lightweight caroussel containing radially arranged optical elements, mounted on a central axle. A DC or stepper motor is used to rotate the disk, moving different elements into the light's path. The motor may be mounted axially as in figure 2.1, or at the rim of the wheel shown in figure 2.2a. Axle mounting is a simple architecture, but needs a large motor for heavy filter wheels. Mounting at the rim means a flatter system architecture, a smaller motor and a higher precision of the system.

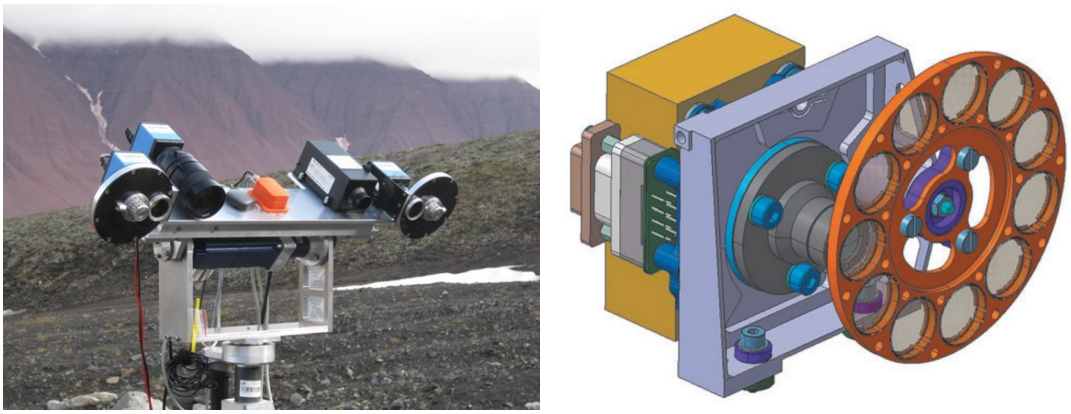

Figure 2.1: Filter wheels used in ESA's ExoMars rover - the PanCam instrument. These are driven by two axle mounted Faulhaber stepper motors [5], [7].

Actuation is typically done using stepper motors. Stepper motors can be driven in open loop mode, have a high power density and can generate a holding torque that keeps the wheel in position during vibrations. The resulting low cost system makes stepper motors a very attractive option to actuate filter wheels.

(a) NIRESS Dual wheel cryogenic instrument slated to fly on James Webb Space Telescope.

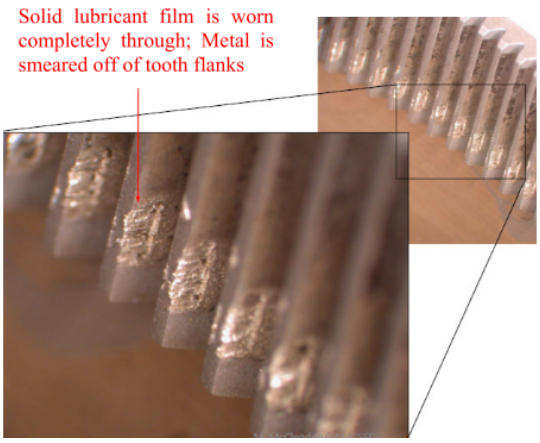

(b) FW ring gear wear at motor pinion contact.

Figure 2.2: 2.2a: NIRESS's filter and pupil wheels are both driven by a stepper motor with a planatary gearhead and a pinion to ring gear. 2.2b: The anti-backlash wheel completely wore through the dry lubricant on the ring gear, leading to a premature failure of the mechanism [9].

The main disadvantage of stepper motors is wear of the gear train. This decreases the mechanism's torque ratio over time and generates debris that will foul the optical elements. As the life time for typical FSO terminals is in the order of 15 years, life time of the drive system is a central challenge in filter wheel design.

The proposed actuator combines the open loop control, power density, low cost and holding force of the stepper motor without suffering from the same wear issues.

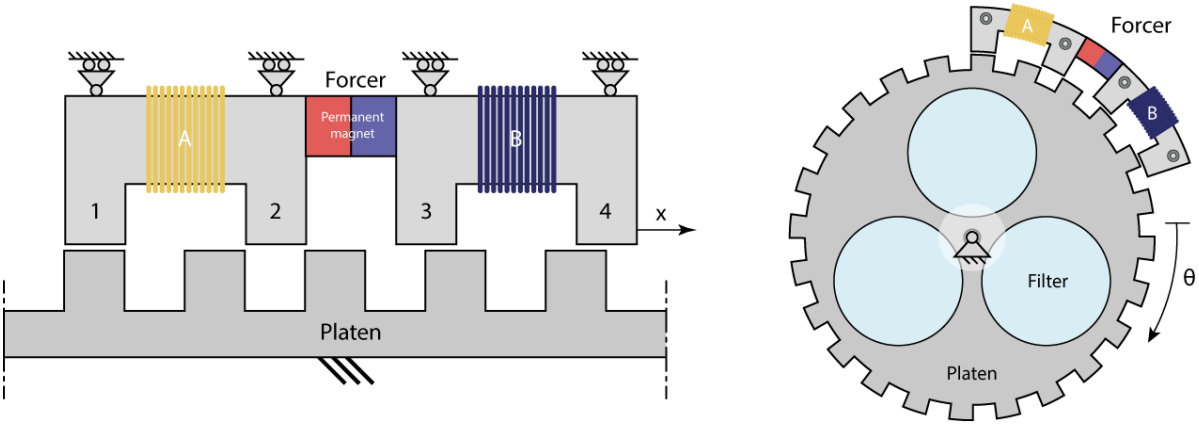

Figure 2.3: The proposed actuation concept adapts a classic HLSM architecture and integrates this with the filter wheel. In this study we assume a 2D linear situation as shown on the left, and extrapolate the results to torque exerted on the filter caroussel.

The basic HLSM design consists of a moving *forcer* and a static *platen*. The forcer consists of two yokes made out of iron, each having two *poles* and one coil, with a permanent magnet (PM) in between. A pole may consist of one or more teeth. The forcer is constrained by a bearing system, allowing only sideways motion. The platen is static and consists of the same iron as the forcer yokes. The proposed actuator fixes the forcer and moves the platen instead. By wrapping the motor's platen around the rim of the wheel, and fixing the forcer, the forcer can exert a torque on the wheel. This flips the arrangement of static and moving parts from the standard HLSM, with a static forcer and a moving rotor.

2.2. Working principle of hybrid linear stepper motors

Hybrid linear stepper motors are a variety of (switched) reluctance motors.

> "Reluctance motors operate on the principle that forces are established that tend to cause iron poles carrying a magnetic flux to align with each. " – Britannica.

When modelling and discussing the actuator concept, we assume a 2D linear situation as sketched in figure 2.3. Because of this simplification, the actuation, or horizontal *actuation force* Fx must be translated to torque the forcer exerts on the filter wheel. The vertical or *normal force* Fy is the attractive force between forcer and platen/rotor. All further analysis will see a static platen and a moving forcer.

The permanent magnet of the HLSM design generates a *cogging force* Cx, which will let the forcer snap to one of four preferred positions, without needing current on the coils. This cogging force stands central to this actuator design and will keep the filter wheel from rotating under vibrations.

The poles of a HLSM may be subdivided into several teeth, as shown in figure 2.10. The *pitch* is defined as the distance of one tooth and gap taken together. In our system, this is twice the width of a tooth. A HLSM has four poles spaced $1/4$ of a pitch length apart. Force is generated by switching on a coil so that its flux will increase- and decrease the permanent magnet flux flowing through poles 1-2 or 3-4. The pole with the highest flux will try to align with the nearest platen tooth. Because of the pole spacing, steps are $1/4$ of the pitch length.

Figure 2.4 shows how turning on coil B will let the forcer move one step to the right. When the forcer has moved 4 steps, the motor has completed a full *phase*. After traversing a phase, the geometry of the forcer and platen repeats and the energising sequence repeats as well. This sequence of a HLSM is the same as a regular bi-polar stepper motor.

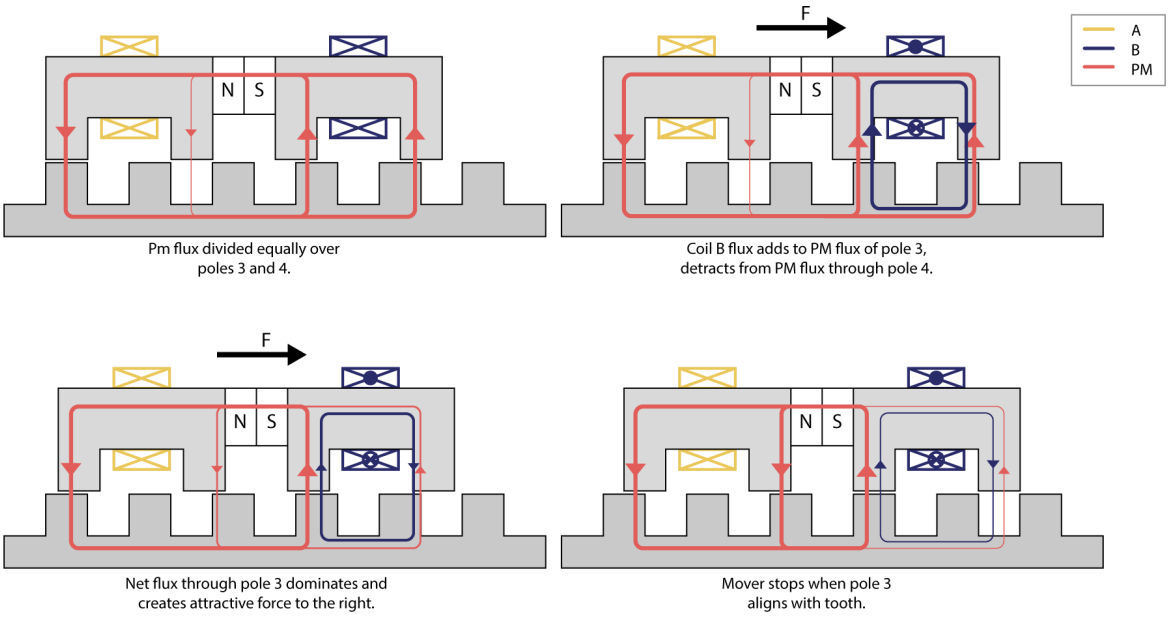

Figure 2.4: Locomotion of the hybrid linear stepper motor. Permanent magnet flux divides itself over poles 1-2 and 3-4. Switching the coils will either contribute or detract from this flux. The pole with the highest amount of flux will align with the nearest platen tooth. In order to take another step to the right in figure 2.4, coil A is energised to generate a clockwise flux, and pole 2 will try to align with a platen tooth.

2.3. Modeling of hybrid linear stepper motors

HLSM motors are typically modelled by the magnetic coenergy present in a machine's equivalent magnetic circuit (EMC). In this circuit, *magnetomotive force (MMF)* and *reluctance* together determine what flux is flowing. The reluctance is used to calculate the induction, which is then used to calculate coenergy. The theory and formula of this section are taken from Fitzgerald's *Electric machinery* [8]. The force output of a HLSM motor is the derivative of its coenergy with respect to forcer position.

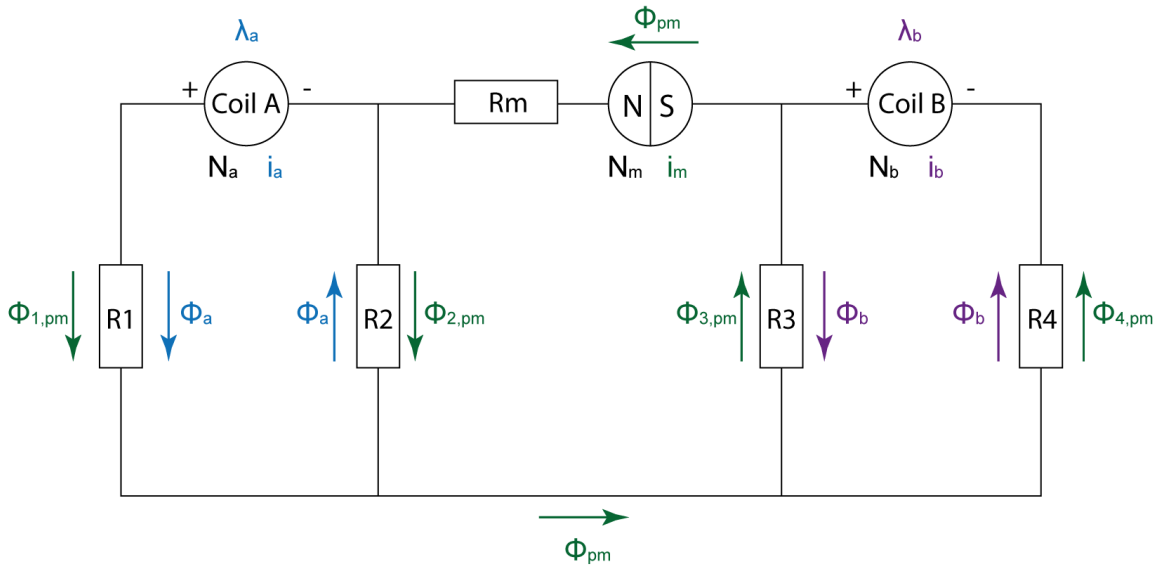

Figure 2.5: Equivalent magnetic circuit (EMC) of the HLSM motor concept. The air gaps between each pole and the platen are modeled as 4 reluctances. The reluctance of the yoke magerial is neglected. The coil circuits are considered separate, because the permanent magnet acts as a magnetic insulator. The magnet itself is modeled as a coil with a large air gap.

Coenergy is defined by the induction of its active elements times current squared.

$$W_f = \frac{1}{2} L_i^2 \tag{2.1}$$

with:

$$L = \frac{N^2}{R} \tag{2.2}$$

N is the amount of windings in a coil, and R the magnetic reluctance of this particular phase. Permanent magnets are modelled as air coils with a constant equivalent current. Each inductive element contributes to the coenergy of the total. Written out this yields the expression for coenergy as:

$$W_f = \frac{L_{\mathrm{pm}}\, {i_p}^2}{2} + \frac{L_a i_a^2}{2} + \frac{L_b\, i_b^2 +}{2} + \frac{L_{a,\mathrm{pm}} i_a i_p}{2} + \frac{L_{b,\mathrm{pm}}\, i_b i_p}{2} \tag{2.3}$$

The first three terms are the self-induction of permanent magnet coils. The last two terms are the mutual inductances, which are the PM flux flowing through the (active) coils. With constant current, force is the derivative of induction, itself dependend on the change in reluctance. Hence the name *reluctance motor*.

$$F_x = \frac{\partial}{\partial x} W_f = \left(\frac{1}{2} \frac{\partial}{\partial x} L_i^2 i_i^2 \right) = \frac{1}{2} N^2 i^2 \frac{\partial}{\partial x} \left(\frac{1}{R} \right) \tag{2.4}$$

When a coil is energised, the forcer will start moving in the direction that decreases reluctance, as shown in figure 2.4. Reluctance decreases when a pole starts overlapping more with a platen tooth.

Because even vacuum has a magnetic permeability, flux will not be completely confined to the forcer and platen material, but will fringe around the air gaps. The effect is that the reluctance that the PM flux encounters will not be completely constant for all forcer positions, and certain forcer positions will have a higher coenergy. The forcer therefore experiences a force to move towards these positions; the so called cogging. Cogging is thus caused by fringing effects, leading to non-constant PM inductance and a varying coenergy.

Because the motor has four poles, each phase has 4 stable cogging positions of the cogging force.

To correctly describe motor behaviour, an accurate reluctance (or it's inverse, permeance) model is needed. Reluctance in EMC models can be modelled using permeance tubes, which are assumed paths flux takes with a mean length and normal surface area. Their reluctance (or permeance) can be calculated using:

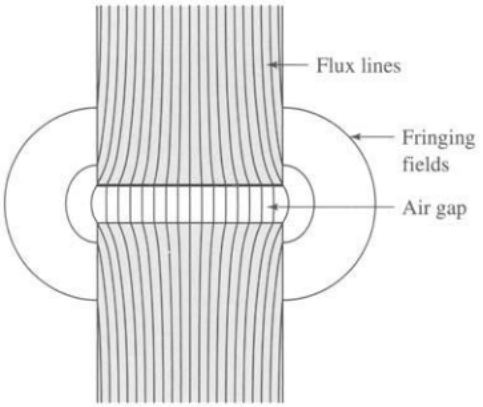

Figure 2.6: Because all materials and even vacuum permit flux, flux will fringe around an air gap [8].

$$R_i = \frac{l_i}{A_i \mu_0} \tag{2.5}$$

With l_i the mean path length, and A_i the normal cross section of the tube. However, this method relies on many assumptions and requires evaluating the flux tubes for every forcer position. Altogether *"permeance evaluation at each translator position is a cumbersome task"* [6].

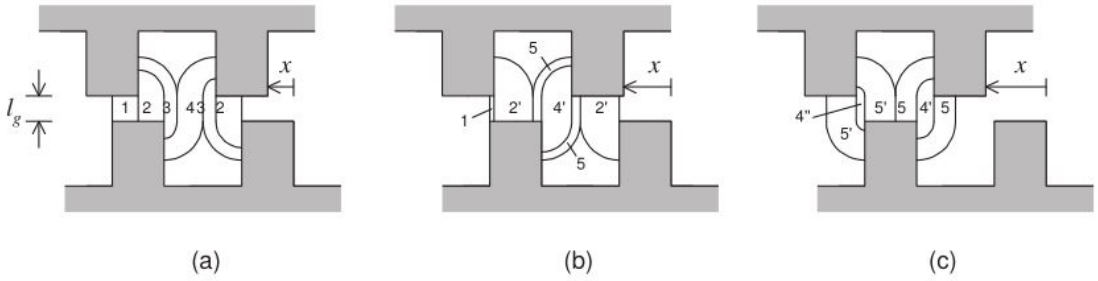

Figure 13: Assumed flux paths between toothed structures at different displacement values: (a) $0 \leq x \leq 0.5w_v$, (b) $0.5w_v \leq x \leq 0.5w_t$ and (c) $w_t \leq x \leq 0.5(w_t + w_v)$.

Figure 2.7: Flux tubes assumed for a variable reluctance machine using the method of [6], by [1].

Because each forcer and platen geometry will require its own permeance model, this method does not generalise at all. Because of the amount of effort this requires, most design methods use reasoning, intuition and FEA models to validate instead [13], [11], [2].

2.4. Motor characteristics and design parameters

The main motor performance characteristics investigated in this research are the cogging force, actuation force and normal force. Plotting the cogging, actuation and normal forces over forcer location creates a set of *force/displacement curves* Cx/x, Fx/x, Fy/x. The literature part of this study shows several finite element analyses (FEA) done in FEMM 4.2 software and an analytical model based on the equivalent magnetic circuit from figure 2.5.

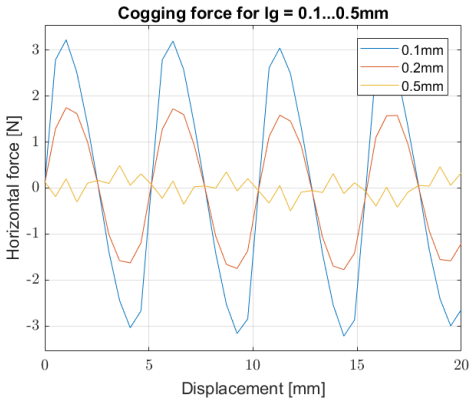

(a) Cogging force at different forcer positions.

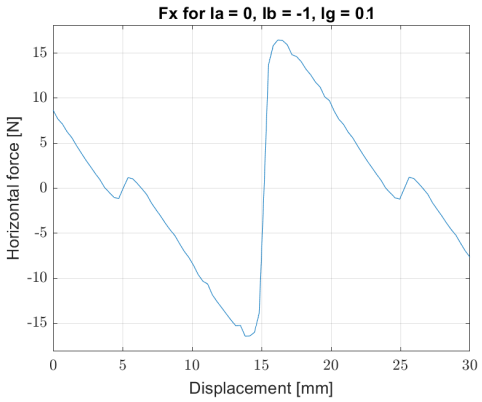

(b) Actuation force at different forcer positions

Figure 2.8: Cogging force and actuation force at different forcer positions, calculated by FEMM 4.2 in the literature study. Cogging shows as a horizontal force that wants to move the forcer to positions spaced $1/4$ of the pitch length apart. Actuation force is linear, but shows extra forcer positions where no actuation force is generated.

The literature's FEA results in figure 2.8 show that the forcer indeed experiences a cogging force to positions spaced $1/4$ pitch length apart.

The shape of the actuation force/displacement curve changes linearly over position, and shows forcer positions where no torque is generated. This disagrees with literature, which states that the actuation force of HLSM varies sine-like with forcer position as in figure 2.9a [14].

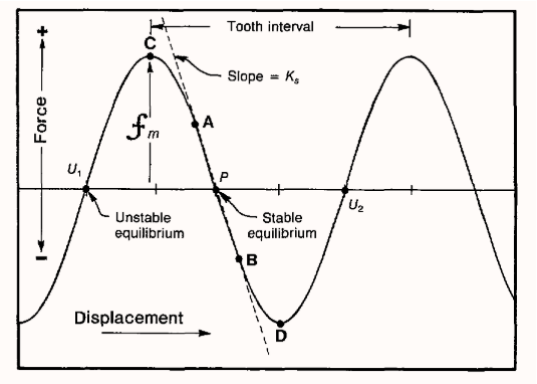

(a) Actuation force at different forcer positions by Pelta [14].

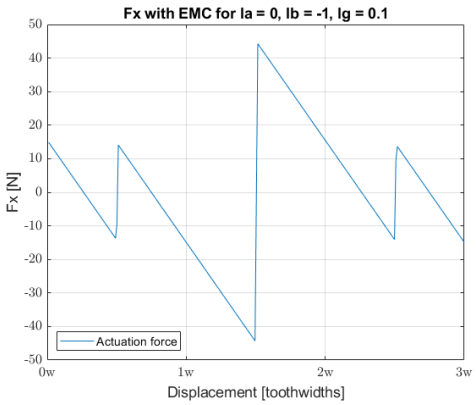

(b) Actuation force calculated using the EMC model shown in figure 2.5 model.

Figure 2.9: Actuation forces as predicted by Pelta varies sine-like with forcer position. The analytical model of the literature study yields a different Fx/x, and shows extra forcer positions where no actuation force is generated. Both images show that a HLSM has both stable and unstable forcer positions.

The EMC model shown in figure 2.5 was calculated with a reluctance model of only the first flux tube taken from figure 2.7, whose length and area were entered into equation 2.5. This neglects the fringing effects of figure 2.6, but nevertheless yields the same results to the FEA studies: that there are some parameter combinations leading to forcer positions where $Fx = 0$.

The EMC model does not capture the important cogging behaviour that our application needs, and does not take material properties into account. A more thorough finite element analysis and breadboard

tests will have to show what exactly is the HLSM's output.

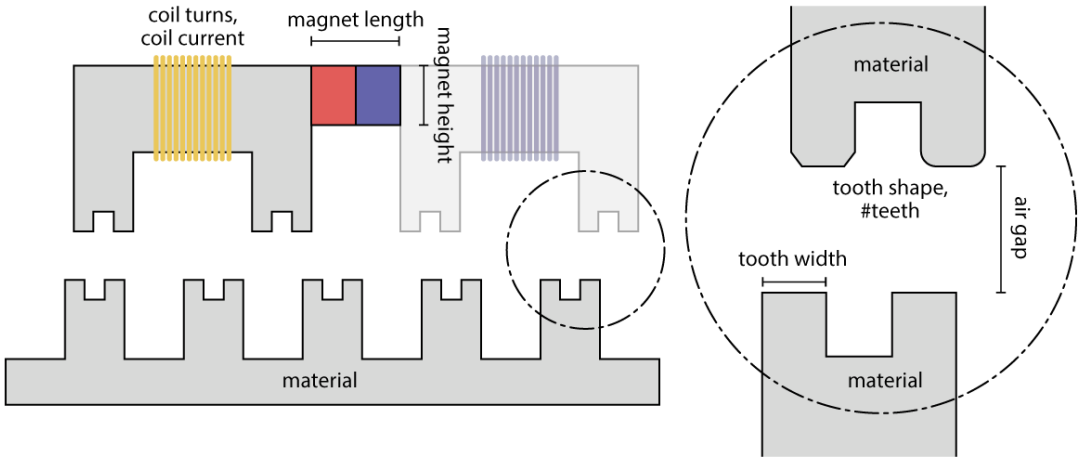

Figure 2.10: Important design parameters of the hybrid linear stepper motor. Machine depth scales the system linearly and is not displayed or investigated.

Equation 2.3 shows that all design parameters have an effect on the inductance, reluctance and the change of these during forcer movement. Hence they also have an effect on the force/displacement curves of cogging, actuation and normal forces. A variable that is not in this equation, but has a large influence on the shape and length of the air gap, is tooth shape. Some studies show that non-square teeth not only lead to different behaviour, but perform better overall [17]. Hence this study investigates many HLSM design parameters, that are displayed in figure 2.10:

- **Air gap distance.**
  Vertical distance between forcer teeth and platen. This directly influences the reluctance in the EMC, so is one of the most important parameters of the HLSM design.

- **Tooth shape.**
  The shape of tooth, e.g. square, round, circular. This influences the air gap geometry and thus also the reluctance in the EMC.

- **Tooth width.**
  The horizontal distance between the leftmost and rightmost edge of a tooth.

- **Number of teeth per pole.**
  How many teeth of a certain width comprise one pole. Tooth width and number of teeth together define pole surface area. The surface area of the poles directly influences the reluctance of the EMC.

- **Magnet length.**
  The distance between the two magnetised surfaces of the permanent magnet.

- **Magnet surface area.**
  Surface area of a magnetised face of the magnet. In this study, this is determined by the machine depth and the magnet height.

- **Machine depth.**
  In this study we consider a 2D model of the HLSM. The output of this model scales linearly with depth.

- **Coil turns.**
  Number of (copper) wire turns of the two coils.

- **Coil current.**

- **Yoke and platen material.**
  The yoke and platen material are considered the same. The material has a certain maximum flux density before it saturates.

2.5. Performance metrics

To better quantify the motor performance and behaviour, several performance metrics are devised. These are used to discuss and to compare data between analytical, FEA and breadboard. All performance metrics are calculated with the complete forcer output during one motor phase. The following metrics are created and are shown in figures 2.12, 2.13 and 2.11.

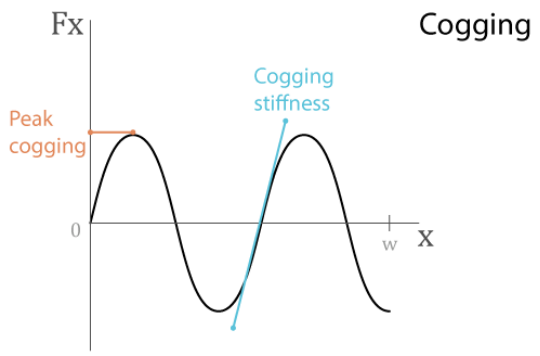

Figure 2.11: Metrics of cogging force.

- **Peak amplitude of cogging force**
  If the peak amplitude of the cogging force is higher than the lock force required to keep the rotor still, the filter wheel will become resistant to vibrations and attitude changes, which is critical for the viability of the RHLSM concept.
- **Stiffness of cogging force**
  The stiffness of the cogging determines the repeatability of the filter wheel when unpowered. It also determines to what extent the filter wheel moves under typical vibrations or attitude changes.

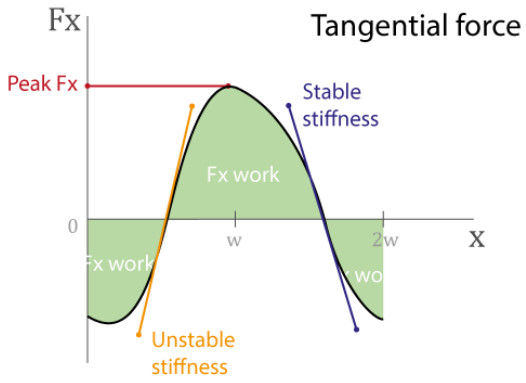

Figure 2.12: Metrics of actuation force.

- **Peak actuation force**
  A crude measurement of force output.
- **Fx work done**
  Work done by actuation force during forcer movement through one phase. Because the shape of the Fx/x varies with motor parameters, the complete energy output of the motor during one phase is a more objective metric to compare motor performance at different parameters.
- **Stiffness of actuation force**
  The stiffness of the actuation force determines the repeatability of the motor. The stiffer the motor, the closer the forcer can move to its target position before the bearing friction brings the wheel to a stop.
- **Power density**
  The work done metric divided by the volume of the forcer. This shows which configuration is the most space efficient and allows comparison with other motor types. The calculated coil volume will scale with current. Wire thickness will be scaled to have a current density of $10 A/mm^2$, and a packing factor of 2.

- **Peak normal force**
  The peak normal force determines how much force the bearing system must be able to cope with.
- **Peak to peak normal force**
  If the normal force changes greatly during moving, fast motions will create vibrations in the system. Ideally the normal force is constant.

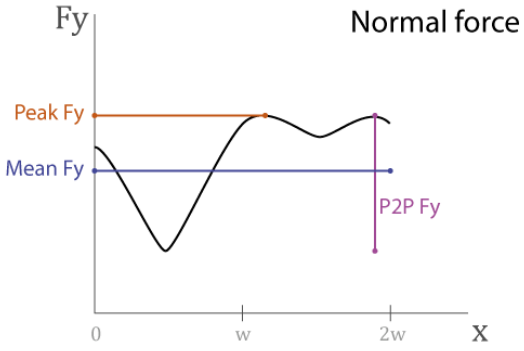

Figure 2.13: Metrics of normal force.

3

Understanding hybrid linear stepper motors by modelling

An equivalent magnetic circuit model as shown in figure 2.5, with an assumed 1D flux tube reluctance model as in 2.7, already behaves like FEA results from figure 2.8b. However, the model does not capture cogging behaviour and does not show the sinusoidal actuation force as mentioned by Pelta [14]. A better analytical model of the HLSM motor can help us in several ways:

- It gives a deeper understanding of the HLSM working principle.
- It gives a framework to interpret FEA results.
- The model can be used to investigate the effect of design parameters.
- A model can show how design parameters scale the motor output. The model can estimate the required dimensions for a breadboard.

Several research questions and their hypotheses are formulated:

- **What components generate force and how do the design parameters influence this?**
  The coil and the magnet-coil interaction create the actuation force. The PM alone generates the cogging.
- **Do some parameter combinations have to be avoided? Are some better than others?**
  Figure 2.8b shows that under some conditions unwanted extra forcer positions with no actuation force occur. The analytical model can show us when and why this happens.
- **Where does cogging come from?**
  The 1D flux tube model from figure 2.7 leads to a reluctance that varies with the reciprocal of pole-platen tooth overlap $R(x) \sim 1/A(x)$. This model shows no cogging. Cogging must therefore come from second order effects such as fringing.
- **Can cogging be modeled by using a different reluctance model? Is this other model better at describing motor behaviour?**
  Introducing non-linearities to the 1D flux tube reluctance model can simulate fringing induced cogging behaviour. This is faster than implementing more flux tubes.
  Pelta's description of a sine-line force/displacement in figure 2.9a also leads to believe that reluctance does not vary with the reciprocal of pole overlap area, but that $\partial R/\partial x$ is sine-like instead of linear. This sine model can be fit to FEA data and might prove to be more accurate.

3.1. Approach

The analytical model uses the EMC model shown in figure 2.5. The investigation into force components is done by deconstructing the coenergy equation into force generating terms. The effect of each term is explained and parameters for stable motor behaviour are derived. An algorithm is written that finds the parameter set that yields any desired motor characteristic. The different motor characteristics are then compared on the metrics which shows us what combination of current and magnet size is optimal for our application.

Secondly the 1D flux tube model reluctance model $R(x) = 1/A(x)$ is compared with a sine model $R(x) = A\,sinx$, that scales a base reluctance to any value between R_{min} and $A * R_{min}$. A non-linearity is introduced to both functions to model fringing effects. This will lead to a non-constant PM inductance, which in turn generates cogging. The strength of the non-linearity will determine the magnitude of the cogging force.

All the calculations shown in this section use the same motor dimensions as the breadboard, which are displayed in D.3.

- 10mm problem depth
- 0.15mm air gap
- 3x3mm wide tooth
- 950 KA/m coercivity magnet
- 20x10x5mm magnet
- 1600 coil turns
- 0 to 0.3A current for sweep

3.2. Force generation in HLSM

The force in HLSM is generated by the derivative of coenergy. Actuation force is calculated with $\partial E/\partial x$, normal force with $\partial E/\partial y$. Equation 2.3 will be deconstructed to investigate the contribution of each part.

$$W_f = \frac{L_{\mathrm{pm}}\, {i_p}^2}{2} + \frac{L_a i_a^2}{2} + \frac{L_b\, i_b^2 +}{2} + \frac{L_{a,\mathrm{pm}} i_a i_p}{2} + \frac{L_{b,\mathrm{pm}}\, i_b i_p}{2} \tag{2.3}$$

In this investigation only coil B is powered, so the terms with i_a drop out. The 1D flux tube model leads to a constant PM inductance. Therefore the only terms with a non-zero derivative are coil self-induction L_b and mutual coil-PM induction L_{bpm} (mutual induction for short).

Mutual induction L_{bpm} is generated by PM flux flowing through coil B. This varies with the pole 4's overlap area with platen teeth. This yields a triangular shaped induction with a period of 1 pitch length. The self-induction of coil B has a period twice as fast, because either one of poles 3-4 can go out of phase.

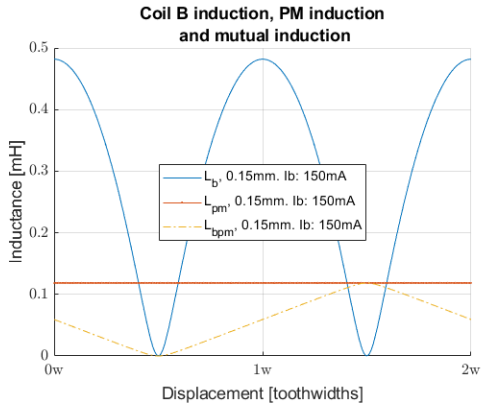

(a) Coil B self-induction, PM self-induction and coil B-PM mutual induction.

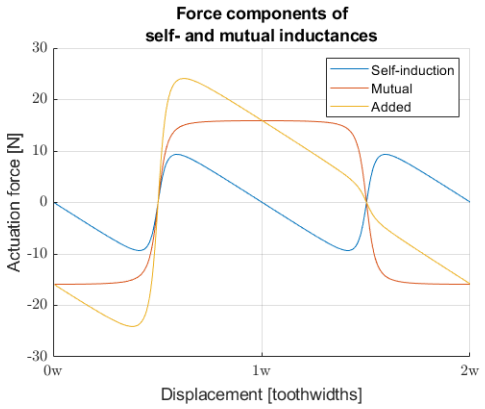

(b) The force contributions of the self- and mutual induction, taken from equation 2.3. Coil B self inductance is sensitive to air gap. PM and mutual induction is not.

As force is the derivative of induction, the force components are block and triangle wave shaped. Because of the different periods, half the time the forces generated by these changing inductances oppose each other. This is best seen in figure 3.1b, where the force components of mutual and self-induction are plot separately. When

$$\frac{\partial L_b}{\partial x} i_b > \frac{\partial L_{bpm}}{\partial x} i_{pm} \tag{3.1}$$

extra forcer positions with no actuation force occor.

In other words: if the coil force component becomes bigger than the mutual force component, the motor becomes unusable. When the current increases, this occurs earlier in the phase. This shows that actuation force does not scale exponentially with current as in other motor types. Instead only the peak force at $x = \pi/2$ grows, together with the occurrence of extra forcer positions where $Fx = 0$.

To increase A HLSM's force output the magnet size will have to increase in tandem with current, which will quickly lead to saturated yoke material. Figure 3.1b also shows that the high stiffness of the actuation at forcer position $3/4$ in the phase is generated by the mutual induction only. Motor stiffness can therefore best be increased with a bigger magnet.

3.2.1. The effects of different MMF ratios on actuation force

Coil B's self inductance in figure 3.1a is sensitive to air gap, while the PM and mutual inductances are not. Therefore every parameter combination of current, magnet size and air gap leads to a different ratio of force contribution, which will yield a different force/displacement characteristic.

The analytical model is used to calculate at what coil current and magnet size the motor characteristic will have extra forcer positions where $Fx = 0$. This is derived in detail in appendix A.1.

For $R_{pm} >> R_{gaps}$ a usable actuation force is guaranteed when the force contribution of the coil equals the force contribution of the mutual inductance. These terms are rearranged to create a ratio between magnet and coil MMF:

$$\frac{\frac{d}{dx}\left(\frac{1}{R_3 + R_4}\right)}{\frac{d}{dx}\left(\frac{R_3}{R_3 + R_4}\right)} = \frac{\mu_m H_c A_m}{N_b i_b} \tag{3.2}$$

The left side is the ratio of change of reluctance between coil B's self-induction and mutual coil B-PM induction. The right side is the ratio between PM and coil MMF, *MMF ratio*. A large magnet yields a large ratio and vice versa. When the two sides of equation 3.2 are equal, Fx/x will be linear and has the highest peak force. If the MMF ratio then decreases the motor characteristic will have extra forcer positions where $Fx = 0$, which is highly undesired. If the MMF ratio increases, the mutual inductance force component start to dominate. The Fx/x then becomes block like and has an extra stiff actuation force.

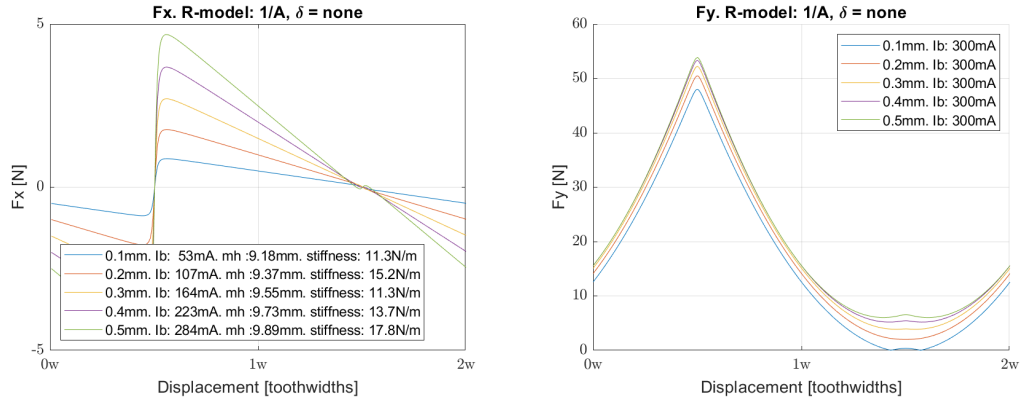

(a) Acutation force. (b) Normal force .

Figure 3.2: Acutation and normal forces for several air gaps with the same ratio of magnet to coil flux, at the same flux density. Because the force generated by the mutual inductance increases with current, larger air gaps -that need a higher current for the same MMF ratio- yield a higher acutation force. Because the flux density at all air gaps is the same, normal force is also the same.

An algorithm has been written that finds the current and magnet size for which the force contributions of the coil and mutual induction are equal. A control factor (CF) in the algorithm increases the mutual force component relative to the coil's, by increasing the magnet size relative to the current. The algorithm then scales current and magnet so that flux density in the air gaps is at saturation level.
With a control factor of 1, the algorithm calculates a magnet size and current that yield a linear Fx/x. A higher control factor gives a block shaped Fx/x with a higher stiffness. This is shown in figure 3.3

Mutual induction is mainly determined by the PM's internal reluctance, so hardly changes with increasing air gaps. Because coil induction does change with air gap, the MMF ratio required for the same Fx/x goes up with air gap length. The same motor behaviour can thus be created at different air gaps, with larger air gaps requiring a higher coil MMF.

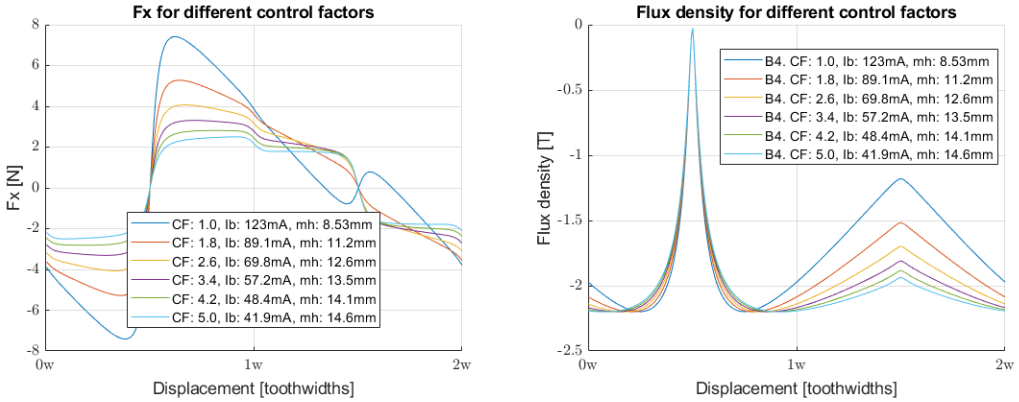

(a) Actuation force.

(b) Flux density.

Figure 3.3: Acutation force and flux density for different PM/Coil MMF ratios, scaled to a maximum flux density of 2.2T. The deviation from linearity in figure 3.3a is caused by assuming $R_m \; l_m$. Scaling the MMF so a flux density is reached yields an actuation- and normal force magnitude similar to FEA studies in figure 2.8b.

3.2.2. Rating different combinations of PM size and coil current on performance metrics

The algorithm is used to investigate what MMF ratio and air gap scores best on 4 performance metrics: Fx work done, power density (Fxwork/volume), electrical efficiency (Fxwork/power) and actuation force stiffness. The system volume scales up with higher PM and coil MMF. Metrics are shown for multiple air gaps.

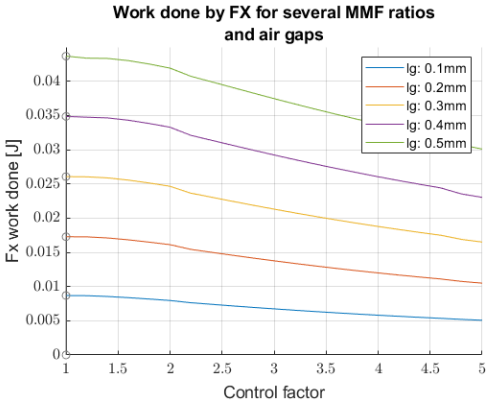

Figure 3.4: Work done by acutation force in one phase for different MMF ratios.

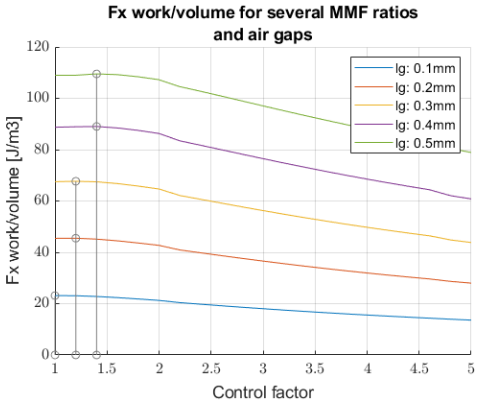

Figure 3.5: Power density of acutation force for different MMF ratios.

Fx work done decreases with MMF ratio, but increases with air gap.
For a constant air gap, work done by the actuation force is highest when the coil and mutual force components are equal. Or: a higher MMF ratio leads to a lower work done by the actuation force.
For the same MMF ratio, larger air gaps increase the work done by the actuation force.

A larger air gap has a higher reluctance, so the current and PM can be increased to generate the same flux density in the air gap. This higher reluctance decreases the coil force component's $\partial L_b/\partial x$, but hardly affects the mutual induction's $\partial L_{bpm}/\partial x$. At the same time the currents increase squared with i_b^2 and $i_b\, I_{pm}$ respectively. Together the higher force caused by the increase in current i_b and PM equivalent current i_{pm} outweighs the decrease in change of induction $\partial L_i/\partial x$. A larger air gap and higher coil and magnet MMF will therefore lead to a higher actuation force, for the same flux density.

In reality $\partial L_i/\partial x$ will decrease faster than the model, because the difference in gap lengths between in- and out of phase becomes smaller. At some point this balances out the increase in acutation force.

This indicates that the highest actuation force output with a fixed amount of yoke material may be generated at a medium length air gap. FEA confirms this behaviour, but the currents and magnets required scale much faster than in the analytical model.

Power density decreases with MMF ratio, and increases with air gap.
For constant air gap, a lower MMF ratio can make do with smaller coils, reducing system volume and potentially increasing power density.

What MMF ratio has the highest power density depends on how fast the coil volume scales with coil MMF. If the coil volume grows quickly with current, the optimal MMF ratio for power density increases with air gap length. This will depend on wire current density, packing factor, etc.

For constant MMF ratio, power density increases with air gap.

This extends the finding for the Fx work done metric. Because coils make up only part of the system, increasing the coil MMF will not linearly scale the total system volume. This allows power density also increase with air gap length. Depending on how the coil volume scales with coil MMF, the most power dense MMF ratios will change with air gap length. Further research will have to clarify what combination of PM MMF, coil MMF and air gap yield the highest power density.

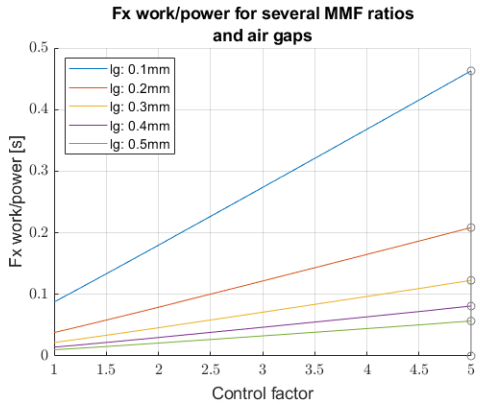

Figure 3.6: Electrical efficiency increases with MMF ratio. Larger air gaps lead to a lower efficiency.

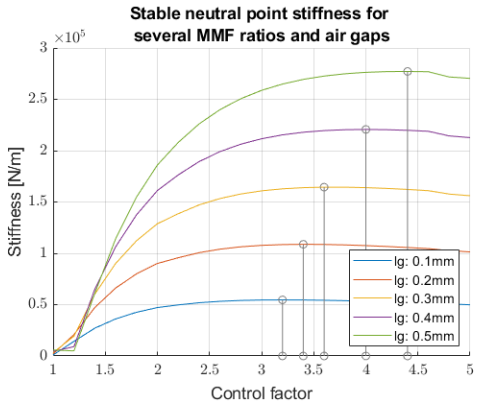

Figure 3.7: Stiffness of the acutation force increases with MMF ratio.

FxWork/power increases linearly with MMF ratio, and decreases with air gap.
For constant air gap, if a greater part of the work is done by the magnet, the electric efficiency will go up. This effect will be limited by increasing cogging forces, until the motor is no longer usable.

For all MMF ratios, a bigger air gap makes energy conversion from electrical to magnetic more difficult, leading to a decrease in electrical efficiency.

Stable neutral point stiffness increases with MMF ratio to an optimum, and increases with air gap.
For constant air gap, the actuation force stiffness has an optimum MMF ratio.

The mutual induction force component generates a high stiffness, so the stiffness increases with PM size. The exact best MMF ratio is sensitive to magnet length. If magnet length goes to infinity, the optimal MMF ratio for stiffness converges to the same value for all air gaps. This value depends on design parameters of tooth width, number of teeth, machine depth.

For all MMF ratios, a larger air gap has a greater actuation force stiffness.

As with the Fx work done, larger air gaps need bigger magnets to saturate the teeth. The mutual force component increases for the same flux density.

3.3. Modeling motor cogging with different reluctance models

Pelta's description of a sine-line force/displacement in figure 2.9a leads to believe that reluctance does not vary with the reciprocal of pole overlap, but that $\partial R/\partial x$ is sine-like instead of linear.

This section compares different reluctance models for the EMC motor model in figure 2.5. The reciprocal-of-overlap reluctance model $R \sim 1/A$ is compared with a sinusoidal reluctance $R \sim sinx$, that varies between R_{min} and R_{max}, depending on the phase of the motor.

Fringing around teeth is approximated in both reluctance models by adding a small non-linearity to the reluctance function. R_{min} is calculated using a 1D flux tube from when a pole is completely in phase,. This should yield a realistic minimum value, as fringing effects are minimal when poles are in phase and one flux tube approximates total reluctance best.

Minimum air gap reluctance, calculated from a flux 'tube' with a finite length and area:

$$R_{min} = \frac{l_g}{\mu_0 A} \tag{2.5}$$

With A a pole's total surface area.

The flux tube model is implemented with:

$$R(x) = R_{min} * 1/s(t)^{1+\delta} \tag{3.3}$$

$$s(t) = \frac{acos(\lambda\, sin(t + \frac{\pi}{2}))}{\pi} \tag{3.4}$$

with $s(t)$ a triangle wave that varies from 0 to 1. For $\delta = 0$ this models reluctnace the same as the 1D flux tube model in figure 2.7, letting it vary between $l_g/\mu_0 A$ and infinity. The rounding factor λ determines the sharpness of the force jumps this generates.

The sine reluctance model is implemented as:

$$R(x) = R_{min} * A\, sin^{2+\delta}(t/2) \tag{3.5}$$

This function will yield a reluctance that varies sinusoidally between R_{min} and $A * R_{min}$. The amplitude is set at a starting value of 8, but can be fit to FEA data. Appendix A.2 goes into more detail about these functions.

By increasing δ, non-linear fringing can be approximated. A small value for δ lets the reluctance of the PM vary, which leads to cogging. If a small value for δ already generates a high cogging, it means that our HLSM prototype will be very sensitive to manufacturing errors, as even a small deviation of the intended reluctance profile will show up in the force/displacement characteristic.

Results of different reluctance models

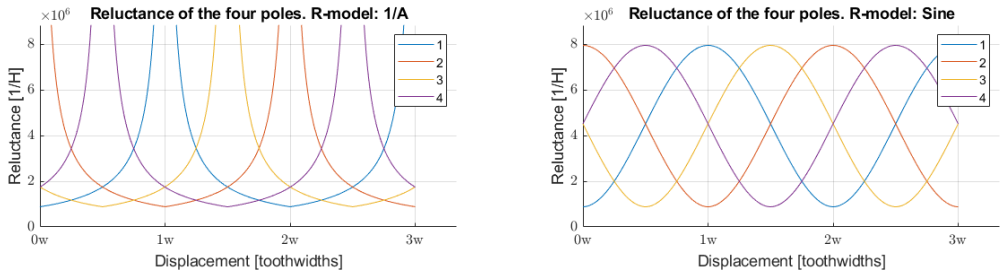

(a) 1D lux tube reluctance.

(b) Sinusoidal reluctance.

Figure 3.8: The two different reluctance models side by side, plot for the 4 poles. The 1D flux tube model sees reluctance going to infinity. The amplitude controls maximum reluctance in the sine model.

When we start to increase δ in the reluctance models, figure 3.9 shows extra harmonics appear that are insensitive to current and scale with δ. These are of similar nature and magnitude as cogging seen in the FEA studies. Only a slight non-linearity is enough to generate cogging of similar magnitude as in the FEA studies, shown in figure 3.10.

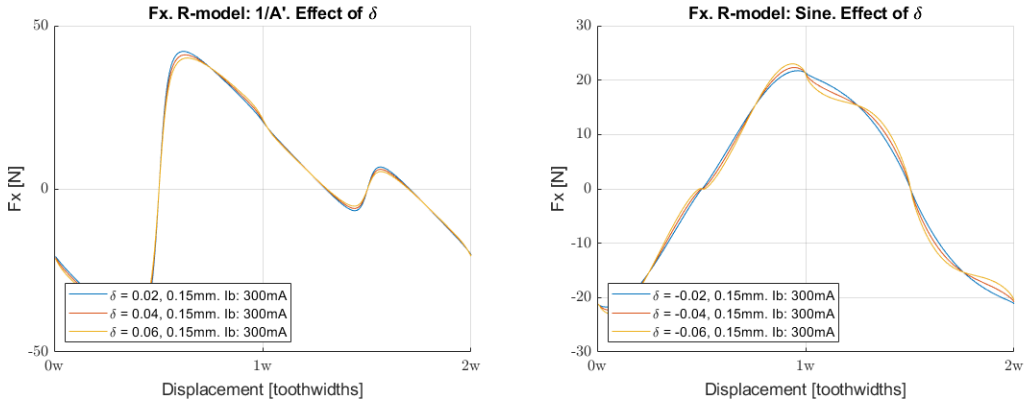

(a) 1D flux tube model.

(b) Sine model.

Figure 3.9: Acutation and forces in both models for several values of δ. Increasing values of δ show as extra harmonics in the force/displacement curve.

For the 1D flux tube model we see a similar result to the early FEA studies: linear force/displacement with some parameter configurations having extra points where no force is generated. For higher air gaps the Fx/x becomes block like, with an extra stiff stable neutral point.

The sine model shows a sinusoidal actuation force/displacement curve as described by Pelta [14]. However, it shows no hint of extra forcer positions where actuation force might be zero. The magnitude of the actuation force differs considerably from the flux tube model. This is because with sinusoidal reluctance $R_3 + R_4 = C$, which leads to a constant coil B induction. Hence coil B does not contribute to the acutation force and only the mutual induction does. The magnitude of mutual induction is dominated by the PM reluctance, so the actuation force scales only slightly with modulating function amplitude, with an optimum at $A = 15$ (not shown).

Normal force is shown in figure A.5 in A.2 and is much much higher than FEA indicates. This is likely because in reality fringing lowers the flux density.

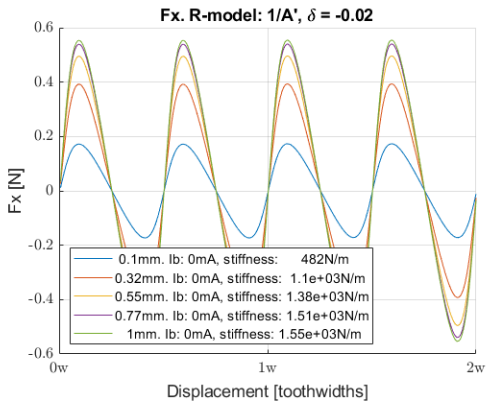

Figure 3.10: Cogging force in the flux tube model for several air gaps.

The introduced cogging harmonic increases with air gap up to an optimum. At larger air gaps, the R_{min} value is higher and $\partial R/\partial x$ increases in the model, leading to a higher cogging. However, figure 2.8a shows that at larger air gaps cogging force quickly drops to zero. A better model can capture this by making the non-linearity a function of the air gap distance and saturation.

The sine model yields similar cogging and behaviour and is not shown. The effect of the factor δ on normal force is too small and is not shown.

3.4. Conclusion modeling HLSM

- Force in a HLSM is generated by the changing coil self-induction and coil-PM mutual induction. The slight variations in PM self-induction generate the cogging force. All design parameters will either increase- or decrease the force that the coil, mutual and PM induction contribute. The combination of these three determines the shape of the cogging and actuation force/displacement curves Cx/x and Fx/x.
- If the coil force contribution becomes bigger than the mutual force contribution, the forcer has extra positions where no actuation force is generated. The exact point at which this occurs is when the ratio between magnet and coil MMF becomes too small:

$$\frac{\frac{d}{dx}\left(\frac{1}{R_3+R_4}\right)}{\frac{d}{dx}\left(\frac{R_3}{R_3+R_4}\right)} < \frac{\mu_m H_c A_m}{N_b i_b} \tag{3.6}$$

  This is undesirable in any application and should be avoided.
- The combination of force components can be tuned for different metrics by changing the ratio between coil and magnet MMF. This is best done by increasing the current or magnet size.
- A high stiffness in the actuation force is generated by the PM mutual induction force only. A stiff actuator will have a large magnet.
- Electrical efficiency increases when the air gap becomes smaller.
- Peak force and power density are highest when the coil and mutual induction force contributions are equal. The MMF ratio to achieve this can be determined from the reluctance models. Because flux will fringe at higher MMFs, this ratio is best determined using FEA.
- The results in section 3.2.2 suggest that actuation force may be further increased by increasing the air gap length. A larger air gap will have a higher reluctance, so the coil and magnet MMF have to increase to reach the same flux densities. The increased current and magnet size increases actuation force faster than $\partial L/\partial x$ will decrease. In reality $\partial L/\partial x$ will decrease faster than in the model, because the difference in gap lengths between in and out of phase becomes smaller. Depending on how the coil volume scales with coil MMF, the highest power density may thus be achieved using a medium length air gap. Further study will have to validate this result.
- Two reluctance models describe reality in a useful way. A sine model leads to literature's described sine-like force/displacement curve, which can be fit to FEA results. When fit properly, this predicts motor output better than the 1D flux tube model. A 1D flux tube model explains the behaviour seen in FEA and sheds light on what parameter combinations are desireable, and what should be avoided.
- Cogging can be added to both reluctance models by introducing non-linearities to the reluctance function. However, this does not behave as cogging from FEA studies so its value is limited.

4

Understanding the HLSM motor through finite element parameter sweeps

The goal of the parameter sweeps is to investigate the things that the analytical model did not. This includes saturation, fringing and material properties. The best way to achieve this is by using finite element analysis and a non-linear material model.

The research questions of the finite element parameter sweeps are:

- **What is the effect of fringing on motor behaviour, specifically cogging?**
  Fringing causes cogging. If we can increase fringing, cogging will be increases as well.
- **What is the effect of material saturation on motor behaviour?**
  Saturation limits the maximum power output of the motor. A higher saturation leads to more fringing, so more cogging.
- **Does the yoke material reluctance have an influence?**
  Szabo and Viorel note that this motor architecture suffers from a difference between the inner- and outer poles [17]. The effect of this is not mentioned.
- **What is the effect of air gap, magnet surface area, current, teeth size, number of teeth and material saturation on cogging, actuation and normal forces. Can we summarize this?**
  Behaviour ought to be similar to that of the analytical model. The most interesting is what happens when the teeth saturate.
- **Do certain combinations of PM and coil MMF have to be prevented in order for a stable motor characteristic?**
  The analytical model shows that this occurs when the force contribution of coil and mutual inductions is equal. The effects of material reluctance and fringing will likely make this much harder to achieve in FEA.
- **Are there optimal dimensions or ratios for this motor type and architecture?**
  Tooth width/air gap will have an optimum ratio. Saturation level will likely have an optimum level for power density as well.

4.1. Approach

A parameter sweep is done using the FEMM 4.2 software. This is an open source, easy to use FEM package used in 2D magnetics modelling. The software is controlled using MATLAB, which generates a fully parametric forcer model based on all design parameters such as tooth width, pole height, magnet size, etc.

In each sweep one parameter is changed, while the others are kept constant. A sweep constists of the forcer moving through a full phase twice: once with both coils unpowered and a second time with 0.3A on coil B. Moving further will repeat the geometrical arrangement of forcer and platen teeth, so will not yield more information. To speed up calculation a pole consists of one large tooth.

In the teeth size sweep, the 10mm pole surface is divided over increasing numbers of teeth, so that the pole surface area remains constant. In the number of teeth sweep, teeth of 10mm wide are added for each successive pass, so that the pole surface area linearly increases. Since the normal force is much higher than the actuation force, the normal force plots are often very similar to those of the coenergy. Hence, only some sweep results show coenergy to explain the results.

The parameters used in the sweeps are again the same as the breadboard displayed in D.3, but with poles having only 1 large tooth. This speeds op calculation:

- 10mm problem depth
- 0.15mm air gap
- 1x10mm wide tooth
- 950 KA/m coercivity magnet
- 20x10x5mm magnet
- 1600 coil turns
- 0.3A on coil B for a powered sweep

4.2. Results of finite element parameter sweeps

The result of the current sweep is shown in figure 4.1. All other parameter sweep plots can be found in appendix B.

Current sweep

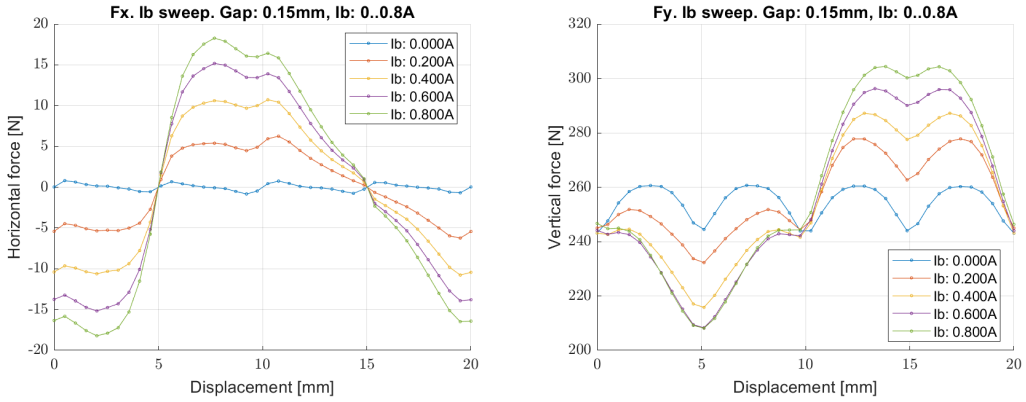

(a) Actuation force.

(b) Normal force.

Figure 4.1: Current sweep. Actuation force increases linearly with current until saturation.

At increasing current the horizontal force increases linearly. Saturation of the yoke material shows as diminishing returns for higher currents. The cogging harmonic persists for all current levels and can be considered to be 'added' to the actuation force. This means that a motor with a high cogging, as is our design brief, will always have harmonics in the actuation force. This could make the RHLSM concept suffer from vibrations.

The effects that design paramters have on motor output are summarised below:

Air gap distance

- For the same tooth width, cogging decreases exponentially with air gap length until a minimum base cogging is left. This base cogging is caused by a difference of reluctance between the inner- and outer yoke's flux paths.
- Actuation force decreases little with air gap and will not go to zero. This decrease is linear. The mutual induction force component is insensitive to air gap, so the force decreases little.
- The stiffness of actuation force does not change with air gap. This is because the stiffness is generated mainly by the mutual induction force component.
- Normal force decreases linearly with air gap.

Permanent magnet surface area

- For square teeth, cogging only occurs when the yoke material saturates, after which flux will start fringing around the air gaps. This requires a minimum magnet surface area.
- After a minimum flux density, cogging increases exponentially with magnet area up to saturation.
- Below a certain magnet size, the motor Fx/x shows extra points where $Fx = 0$, as in the analytical model. The MMF ratio at which this happens is much lower than in the analytical model.
- Increasing the magnet size increases actuation force linearly until saturation.
- Normal force grows linearly with magnet surface area until saturation.

Current

- Actuation force increases linearly with current until saturation.
- Peak normal force also increases linearly with current until saturation.

Tooth width – constant pole surface area

- With constant pole surface area and air gap, having more, smaller teeth linearly decreases cogging.
- Actuation force increases with smaller teeth up to a maximum, before decreasing again. The optimal ratio between tooth width and air gap lies between 8 and 11.
- Stiffness of the actuation force increases until the optimal tooth width/air gap ratio is reached.
- Normal force decreases with tooth width to a minimum value.

Number of teeth – increasing pole surface area

- Increasing the pole surface area by adding more teeth of the same size, lowers cogging until the base cogging is left.
- Once present the base cogging increases with the pole surface area, as yoke reluctance becomes more dominant.
- Peak actuation force increases with the pole surface area to a maximum. If the surface area becomes too big, extra positions where $Fx = 0$ occur.
- Normal force reduces with the pole surface area.

Material and saturation

- A material with a lower saturation density will yield a higher cogging, up to a point where teeth are permanently saturated.
- The actuation force and normal force both reduce linearly with saturation density.

4.3. Conclusion of finite element parameter sweeps

- At low flux densities the analytical model explains the motor behaviour well.
- When teeth become saturated, flux will start fringing around the air gaps and even cross between teeth. This fringing causes PM inductance to vary, generating cogging.
- With square teeth a minimum level of PM flux is required, in order to induce enough fringing to generate cogging. Cogging force is limited by the tooth material's saturation limit. The cogging harmonic will always show in the actuation force.
- Potential force output increases with the yoke material saturation limit. Increasing flux density beyond saturation levels will not increase the actuation force, but will only increase hysteresis losses. A filter wheel concept will have to scale the pole surface area so that teeth are saturated just enough for cogging. The size of the area depends on magnet MMF, air gap and yoke material.
- Low PM/coil MMF ratios indeed lead to an unwanted motor characteristic, with extra positions where $Fx = 0$. The MMF ratio under which this happens is much lower than in the analytical model. The filter wheel concept will require a large magnet to generate cogging, so will not suffer from this issue.
- The yoke reluctance makes that the inner two poles have more flux flowing than the outer two poles. At low air gap reluctance this leads to a base cogging which would make the motor unsuitable for the filter wheel application. A different motor architecture can solve this.
- The optimal tooth width/gap length ratio lies between 8 and 11. If the ratio becomes lower, flux will start crossing the gaps between teeth and actuation force will drop. The minimum teeth size -and maximum power density- is thus determined by how small the bearing system and manufacturing tolerance can make the air gap.

5

Investigating different tooth shapes

Szabo and Viorel showed a small FEA study with different tooth shapes for HLSM [17]. Trapezium shaped teeth showed promise for generating the same actuation force, but with a lower normal force. Research is also done which tooth shapes reduce cogging and torque ripple, such in [13]. However, increasing cogging forces has not seen much interest. This section therefore investigates the effect of tooth geometry on the cogging, actuation and normal force/displacement curves. Several questions are formulated:

- **Can cogging be increased or decreased by changing the tooth geometry?**
  A varying PM inductance generates cogging. For square teeth this is caused by fringing flux. A varying air gap length should also change the PM inductance, thereby increasing cogging.
- **How does tooth shape affect actuation and normal force?**
  Force is generated by a change in reluctance. This change may be increased by having another tooth shape. Literature indicates that normal force of trapezoidal teeth is lower.
- **What is the ideal tooth shape for our filter wheel design?**
  A tooth shape that generates the highest cogging would be ideal, as the required actuation force is very low.

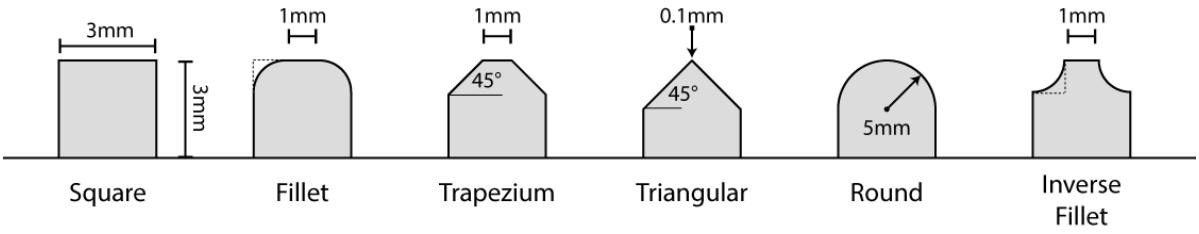

Figure 5.1: Different tooth shapes investigated in this study. All teeth have the same width and height.

5.1. Approach

The FEA sweep Matlab code will be expanded with parametrised tooth shapes. Several possible tooth shapes were chosen based on their perceived difference in air gap geometry. All teeth have the same envelope. Figure 5.1 shows the tooth shapes the that are tested.

A current sweep was done with each of the tooth shapes. To test a more realistic scenario 3x3mm teeth were chosen. These tooth dimensions also correspond to the breadboard's dimensions, which are shown in appendix D.3. This allows direct comparison of the sweep data and breadboard measurements.

- 10mm problem depth
- 0.15mm air gap
- 3x3mm wide tooth
- 950 KA/m coercivity magnet
- 20x10x5mm magnet
- 1600 coil turns
- 0..0.3A current for sweep

Metrics are then calculated for each tooth shape of the 0.3A forcer pass. Since the dimensions of the forcer are the same except for the teeth, the volume for all the motors when calculating the power density is taken to be the same.

The results shown compare motor output for different tooth shapes. All data of individual teeth and a table of metrics are displayed in appendix C.

5.2. Comparing motor characteristics of different tooth shapes

Comparing cogging forces of different tooth shapes

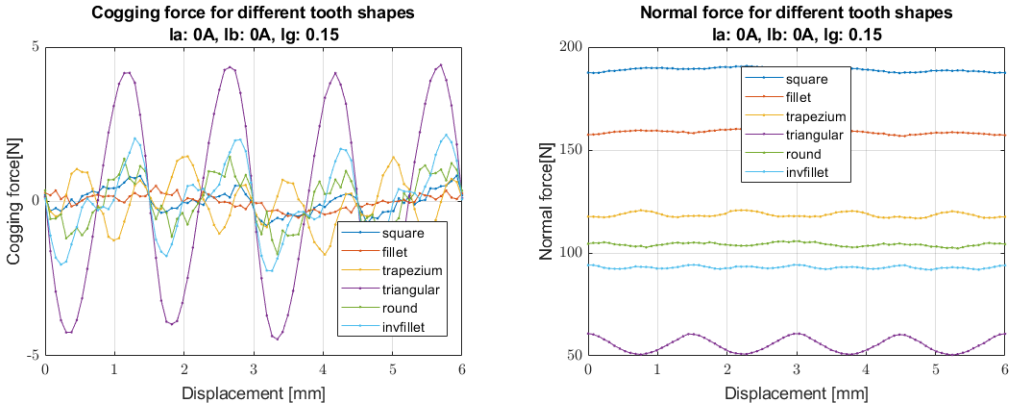

(a) Cogging force.

(b) Normal force.

Figure 5.2: Cogging and normal force of different tooth shapes with no power on the coils. Triangular teeth generate the highest cogging force by far, with the highest stiffness. Filleted teeth generate almost no cogging

Peak cogging force of triangular teeth is 5 times that of square teeth. The stiffness of the cogging for triangular teeth is also much higher than all other teeth. This will increase the repeatability and stability of the filter wheel's motions.

Filleted teeth show an unusually low cogging and the highest peak force of all. The lack of cogging makes them ideal for applications that require smooth motion. The higher peak force makes them highly interesting for all electromotors in general.

The cogging that is generated by filleted teeth is out of phase with the other teeth's cogging. This is investigated further in figure 5.4.

For a smooth cogging, tooth profiles and curvature should generate a continuously changing reluctance value in the PM flux loop. The teeth that have flat tops such as the trapezium and inverse filleted teeth show extra harmonics in the cogging, because air gap geometry is not varying constantly.

Normal force correlates with the amount of tooth material volume. Square teeth, having the highest material volume, have the most flux flowing and thus the highest normal force between forcer and platen. Triangular teeth and inverse filleted teeth have the smallest amount of tooth volume and the lowest normal force. The peak to peak normal forces during movement through a phase also depend on teeth geometry, with triangular teeth showing the highest oscillation.

Comparing actuation and normal forces of different tooth shapes at 0.3A

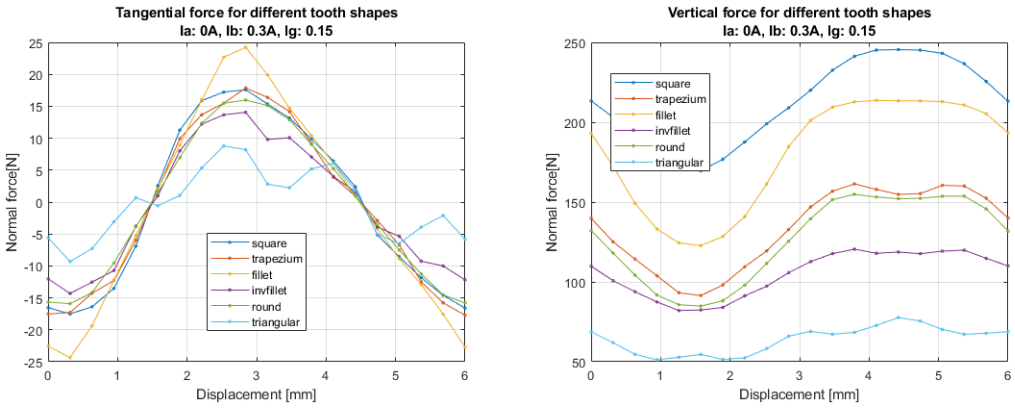

(a) Actuation force

(b) Normal force

Figure 5.3: Actuation and normal force of different tooth shapes at 0.3A. Filleted teeth generate a significantly higher actuation force, while triangular teeth generate a lower, 'ugly' actuation force. Normal force again correlates to tooth volume.

Filleted teeth show a 14% higher peak actuation force and power density than square teeth. The Fx/x is completely linear for these tooth dimensions. Triangular teeth are saturated so much that the actuation force is significantly lower than all other teeth. Instead, the large cogging harmonic creates extra forcer positions where $Fx = 0$.

Normal force again correlates with tooth volume, with different shapes yielding higher- or lower peak to peak values.

5.3. A closer look at filleted teeth

The results of filleted teeth show promise beyond HLSM motors. To further explore a sweep is done with several fillet top widths (=fillet radii). A top width of 0.01mm approximates a round tooth, a top width of 9.99mm a square tooth.

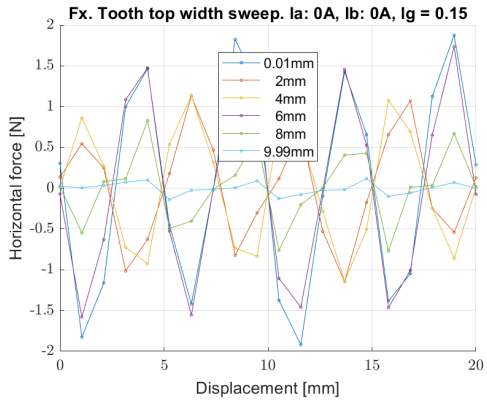

Figure 5.4: Cogging force of filleted teeth with different top widths (=fillet radii).

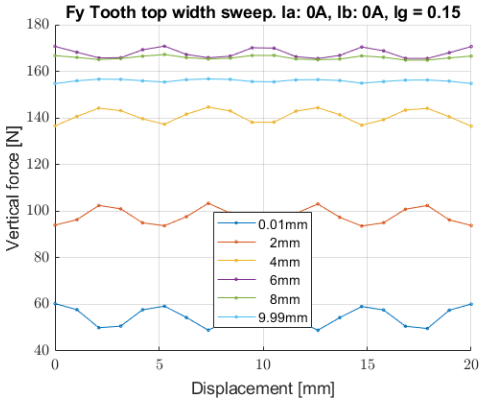

Figure 5.5: Normal force of filleted teeth with different top widths (=fillet radii).

Different roundings lead to vastly different cogging values. A tiny rounding of the teeth will almost completely reduce the cogging to zero. This indicates the tooth fillet radius strongly influences fringing behaviour. Also interesting is that the forcer position with peak cogging shifts half a phase depending on the top width. A visual inspection of the geometry shows that when the fillet radius increases, more flux will start flowing towards neighbouring teeth. When a threshold is reached, this will shift the phase of the coenergy, and thus the cogging.

This phase shift can also be seen in the vertical force. Having somewhat rounded teeth also leads to a higher normal force than having square teeth.

While our filter wheel application requires cogging specifically, these results seem highly promising for other applications and warrant further research into filleted teeth.

5.4. Conclusion different tooth shapes

- Non-square teeth generate varying air gap lengths, which leads to a non-constant PM inductino, generating higher cogging than square teeth.
- All non-square teeth have a lower normal force, because their increased reluctance lowers total flux.
- For even cogging without harmonics, teeth should have profiles that lead to continuous $\partial L_{pm}/\partial x$.
- Triangular teeth generate a 5 times higher cogging force than square teeth, with a much higher cogging stiffness. Their downside is having a low power density for actuation force.
- Filleted teeth have a higher peak actuation force, higher power density and show almost no cogging. For some fillet radii, the fringing effects are canceled by the change in air gap distance. This can extend the use of HLSM motors to other applications that require a smooth actuation force. The behaviour found is highly sensitive to fillet radius and warrants further research.

6

Breadboard design and testing

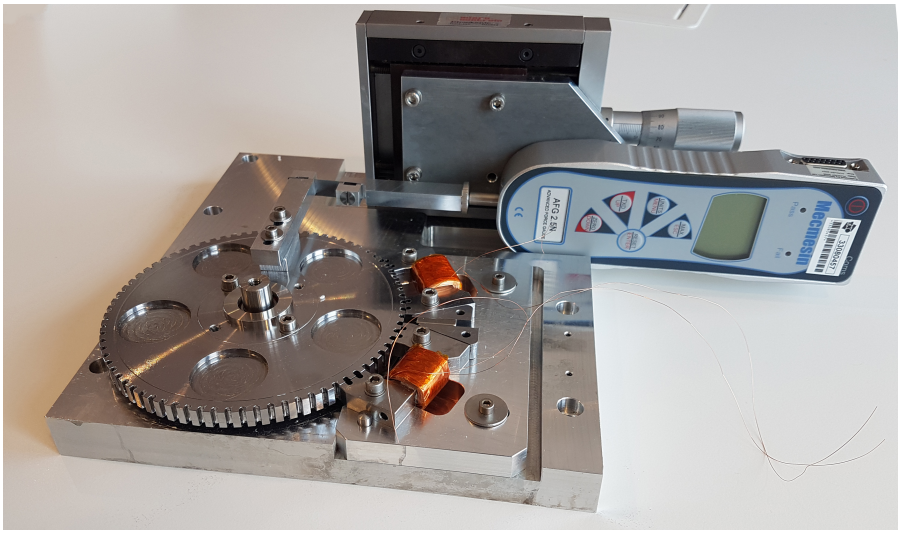

Figure 6.1: The breadboard including force probe (1). More photos of the breadboard can be found in appendix D.

Constructing a breadboard will answer several questions that cannot be answered by modeling:

- **Do the models completely explain the motor behaviour?**
  The analytical model and FEA parameter sweeps have provided a good understanding of HLSM behaviour.A real motor will validate these results..
- **Do the model and FEA predict real motor output correctly?**
  Some difference between FEA and breadboard is to be expected. The FEA is a linear, infinite thickness 2D model, while the breadboard is round and finite. Breadboard output will likely be lower.
- **How easily can a RHLSM be manufactured?**
  The big advantage of using current stepper motors is that they are easy to implement and design for. Ideally the RHLSM concept will not require tight tolerances or complex manufacturing steps. The motor concept is easy to produce, but the cogging may prove to be very sensitive to dimensional inaccuracies.
- **What other difficulties do we encounter?**
  A real world system is the best way to discover any hidden behaviours HLSM might have, and the only way to answer the main research question.

After the experiment the breadboard will serve as a demonstrator for potential clients.

6.1. Approach

The output of the breadboard experiment is a force/displacement curve of the actuation and cogging force. Two things are being measured:

- Cogging force.
- Actuation force for several currents.

Normal force and dynamic behaviour measurements require a more sophisticated setup than time allows for and will not be measured. To create a force/displacement curve, a series of static torque measurements will be taken over a full motor phase. This is repeated for different current levels. Torque is measured using a force probe mounted to a micrometer stage. The probe is connected to the rotor via a flexure, so that moving the stage will rotate the rotor. Positioning the rotor is done manually, after which the probe is read out using MATLAB.

Coil current is provided by a manually operated current source. The force probe is read out with Matlab R2019a. A full summary of the measurement plan can be found in appendix E. A diagram of the measurement setup is shown in figure 6.2

The raw measurement data is processed in the following way:

1. Scale linear displacement to angular displacement around the rim.
2. Mean shift to zero. This will filter out probe bias.
3. Taking the mean of back- and forth measurement. This will reduce the hysteresis error.
4. Scale amplitude to force measured at rim. The probe's moment arm is different than the moment arm of the forcer.

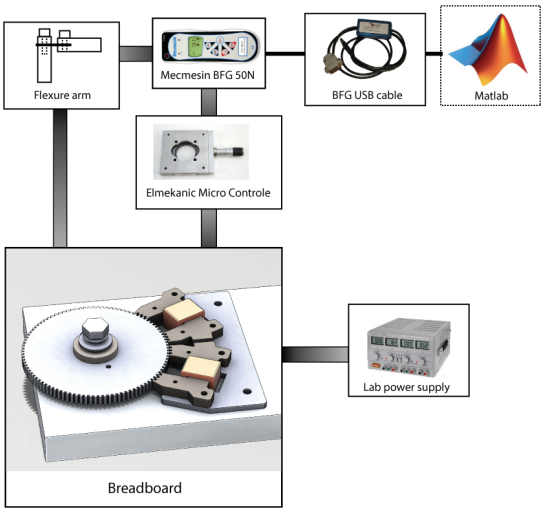

Figure 6.2: Diagram of the measurement setup.

Because the angles are small, stage displacement is taken to be the same distance as the arc distance along the rim of the rotor. After processing the measurements, analytical model and FEA studies are done with the same dimensions as the breadboard. Metrics of all three are calculated and a comparison is made. The main design decisions can be found in appendix D.2. The dimensions chosen are the same as used in the tooth shape sweep to allow comparison of results, and can be found in appendix D.3.

Expected breadboard output

Figure 6.3 shows the expected cogging and actuation force output.

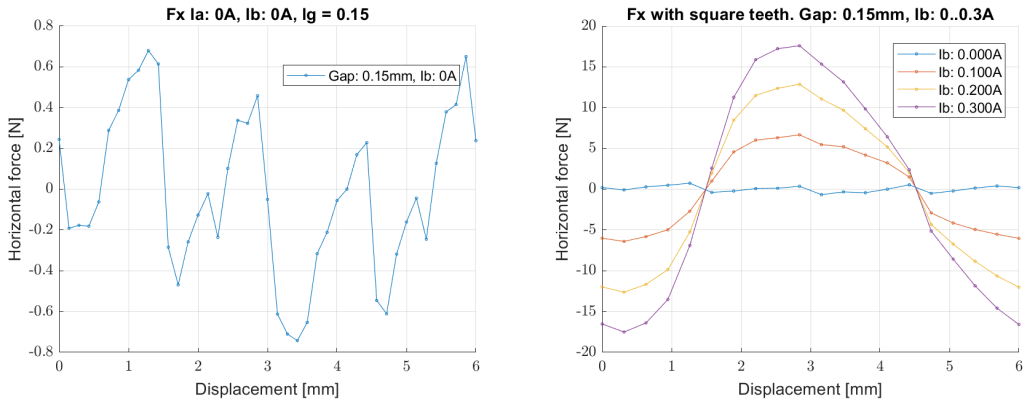

(a) Expected cogging force of the breadboard.

(b) Expected actuation force of the breadboard.

Figure 6.3: Expected breadboard cogging and actuation force force calculated using a 'perfect' square tooth FEA model. 6.3a shows that at these parameters FEA yields no clear cogging behaviour.

Cogging force at these dimensions is not a smooth curve. Slightly different parameters yield very different results.

6.2. Breadboard measurement results

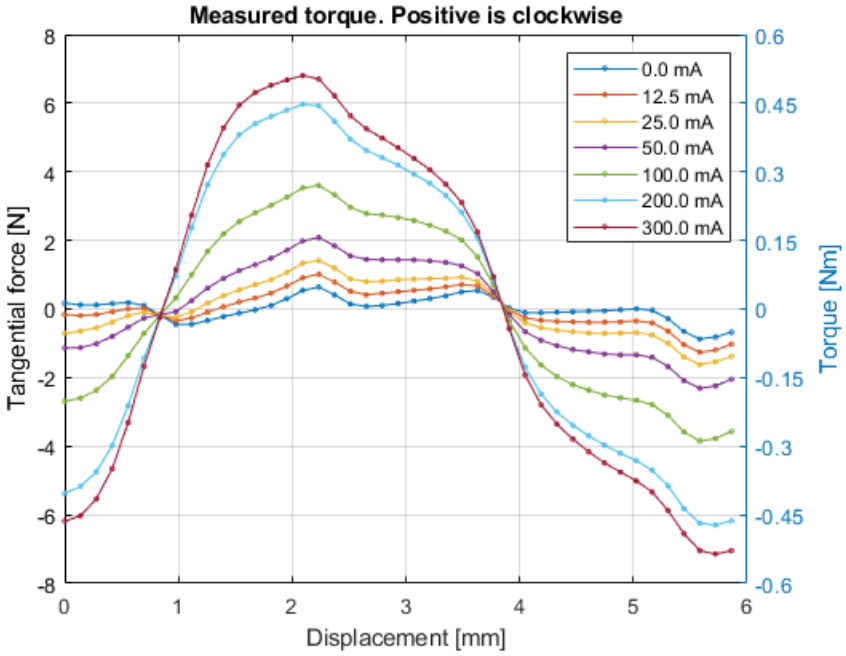

Figure 6.4: Current sweep measuremet of the HLSM breadboard. Positive is clockwise torque.

Several things stand out in the results:

- Force increases linearly with current until saturation, as predicted by the analytical model and FEA.
- The material seems to saturate at around 0.2A, which is much earlier in the FEA.
- Peak acutation force is a factor 2 lower than the FEA results of figure 6.3.
- An extra harmonic is showing in the force/displacement curve at all current levels.
- An overall drift in horizontal force is perceived, caused by the flexure bending exerting an extra force on the probe.
- The curve does not cross zero at $x = 1.5$ and $x = 4.5$ as expected. This is caused by how the phase location of the rotor was determined.

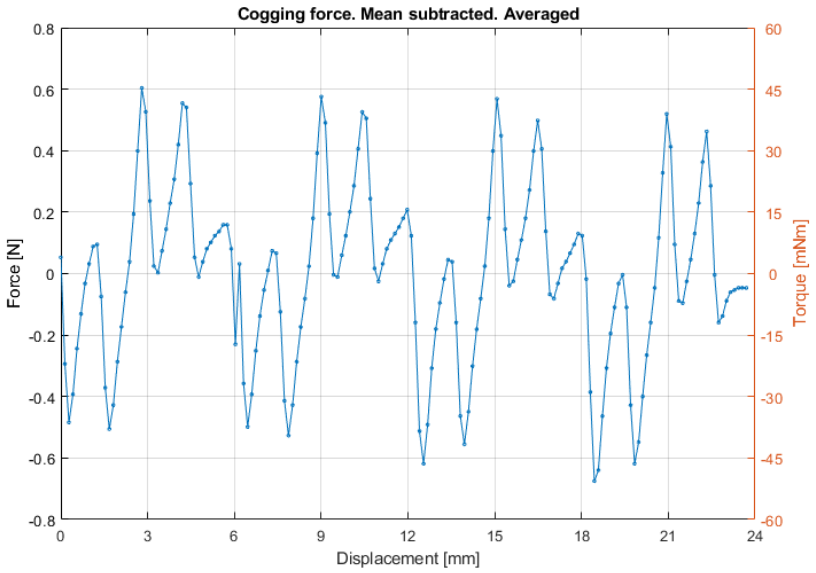

Figure 6.5: Cogging measurement done with a longer, thinner flexure to reduce parasitic forces and allow a greater range of motion.

Cogging of the breadboard shown in figure 6.5 indeed has a period of a quarter pitch length. The cogging force/displacement curve is sine-like, with extra harmonics and a signal modulation over a full phase. This modulation looks almost like the base cogging found in the FEA parameter sweeps.

Tests also showed that this modulation changes with mounting. The poles with the highest cogging stiffnes has a slightly smaller air gap than the others. This difference is in the order of <50 micrometer. The slight drift in force amplitude is the parasitic force of the flexure.

6.3. Comparing results between FEA models and measurements

Before saturation the measured actuation force in figure 6.4 differs a factor 2 with the FEA's predicted output of figure 6.3. Furthermore table 6.1 shows that the stiffness of the actuation force differs a factor 4. The measured cogging magnitude corresponds to FEA values, but figure 6.5 shows a very different shape of the curve. It appears as if a an extra signal is modulating the cogging force.

The difference between predicted and measured actuation force can be explained by the yoke material having a lower maximum saturation density than the material model used in the FEA. The datasheet of the forcer material mentions a maximum saturation density of 2.15T, while the material model's increases up to 2.5T. The datasheet furthermore shows that high levels of permeability are not reached before annealing. Annealing has not been done and no tests were conducted to verify the forcer and platen material's properties. Secondly the difference between models and reality can also account for the results. The breadboard is round instead of linear and it has a finite thickness. Real flux will fringe both in- and out of plane, which will lower the overall $\partial E/\partial x$ and actuation force.

A lower material saturation can also contributes to the shape of the measured cogging force. The extra modulating signal corresponds to the base cogging found in the FEA parameter sweeps of figures B.1 and B.15 in appendix B. The higher yoke reluctance causes the outer poles to have a lower flux density than the inner two poles.

A second cause is that the shape of the cogging curve is highly sensitive to manufacturing and assembly errors. Blunt CNC tooling during the milling of the iron parts has caused all teeth to become wider then spec. The tooth width and spacing varies up to 0.2mm, 7% of the nominal width. The tooth width deviations were measured using calipers and transferred to the FEA model. The calculated actuation force is shown in figure 7.1 and shows similar harmonics as measured in the breadboard, that persist at all current levels.

Next to varying widths, all teeth have fillets with different radii. After milling the rotor teeth were manually deburred with a file. The results for filleted teeth in figure 5.4 show that this greatly influences the cogging force, with very small fillet radii yielding hardly any cogging at all.

Remounting the yokes also changed which pole experiences the stiffest cogging. This means the air gaps under the poles have changed during mounting. The maximum difference caused is in the order of <50 micrometer. Remounting the yokes at 0.1mm -a 50 micrometer difference- already yields over twice the cogging force magnitude.

	Peak FX [N]	FX work done [J]	Stable stiffness [N/m]	Unstable stiffness [N/m}
FEA cogging	0.68	0.002	6.29E3	2.6E3
Measured cogging	.6	0.0019	1.94E3	1.3E3
FEA 0.2A	12.92	0.052	2.63E4	2.45E4
Measured 0.2A	5.96	0.0338	7.16E3	7.08E3
FEA 0.3A	17.71	0.0705	3.076E4	3.16E4
Measured 0.3A	6.8	0.038	7.66E3	8.3E3

Table 6.1: Table with FEA metrics vs measured breadboard metrics. Measured actuation force is 46% of the expected value.

6.4. Conclusion breadboard testing

- The breadboard shows that actuation force scales linearly with current and has the same sine-like actuation force/displacement curve as predicted by Pelta in 2.9a and the FEA [14].
- Even though motor behaviour is as predicted, actuation force magnitude is a factor 2 lower than the FEA shown in in figure 6.3b. This lower magnitude can be explained by a lower than assumed maximum saturation of the yoke material, and the difference between models and reality.
- Measured cogging force is of similar magnitude as predicted by FEA in figure 6.3a, but the shape of its force/displacement curve is very different.
  The difference is caused by the yoke material, the width and shape variations of the teeth, and the mounting error of the two yokes. The shape and magnitude of cogging is highly sensitive to these latter two.
- Manufacturing a RHLSM breadboard proved to be easy, with no unexpected difficulties arising. The sensitive cogging force indicates that tight tolerances on tooth geometry, air gap and mounting are critical.

7

Results of modeling, FEA and breadboard summarized

This chapter summarizes the important findings from the analytical model, finite element analysis and breadboard experiment.

- The analytical model has shown what elements generate force and how this shapes the motor's actuation and normal force/displacement curves. Most importantly it serves as a base to understand the behaviours seen in FEA. The model also suggests there may be optimal ratios for current, magnet size and air gap that lead to the most power dense motor. Fitting a different reluctance model can make the model a reasonable predictor for HLSM actuation force.
- The finite element analyses show that fringing, saturation, material properties and air gap reluctance are central to the output of this motor type. This makes finite element analysis a vital tool for use in HLSM design. FEA also shows that different tooth geometries lead to very different force outputs, with triangular teeth best suited for the filter wheel application, and filleted teeth showing promise for systems that require smooth motion.
- The breadboard testing has shown that the difference between simulation and reality is large. It also shows that the actuation and cogging force characteristics are sensitive to manufacturing and mounting errors. Manufacturing a HLSM with a usable cogging force might prove difficult.

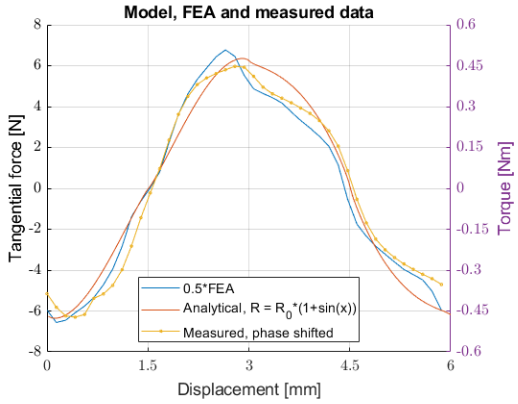

Figure 7.1: Fit analytical model, FEA results and breadboard measurement results. Transferring tooth shape irregularities to the FEA models yields similar harmonics in the Fx/x as measured in the breadboard. The sine-reluctance model can be fit to the measured data to predict realistic results.

The different results of this research are illustrated in figure 7.1. The tooth width deviations from the breadboard were measured using calipers and transferred to the FEA model. This yields similar harmonics in the actuation force/displacement as measured in the breadboard. However, the breadboard's

output is half that of the FEA. The reciprocal-of-overlap model does not predict motor output correctly and is not shown. A current sweep comparison between the fit analytical model and breadboard output is done in appendix D.4, and shows that a good analytical model can predict the motor output.

7.1. Main findings about motor working principle

Cogging in HLSM is generated by PM inductance having 4 local maxima in a phase. Two things contribute to this: saturation and having non-square teeth.

- Saturation will lower the reluctance of the teeth. This will make flux fringe further out and cross the air gap in different ways. This changes the PM reluctance for different forcer positions, so that its inductance varies.
- Non-square teeth lead to air gaps that vary in length over the motor's phase. This also changes reluctance in the PM flux circuit, making PM inductance vary.
- Non-square teeth have a smaller material volume, and are therefore quicker to saturate at the same PM MMF. This is a secondary cogging increasing effect.
- To cause fringing, a minimum flux density is required. Figure B.3 shows that for square teeth and pure iron, this requires a large magnet.
- Filleted teeth are special and may not always generate cogging. Some fillet radii cancel the fringing effects completely and generate no cogging at all, despite high flux densities in the teeth.

The actuation force is generated by the coil's self-induction and the mutual coil-PM induction. The ratio between force contributions shapes the actuation force/displacement curve. All design parameters influence how much each contributes to the actuation force. This ratio can be controlled by changing the coil and magnet MMF.

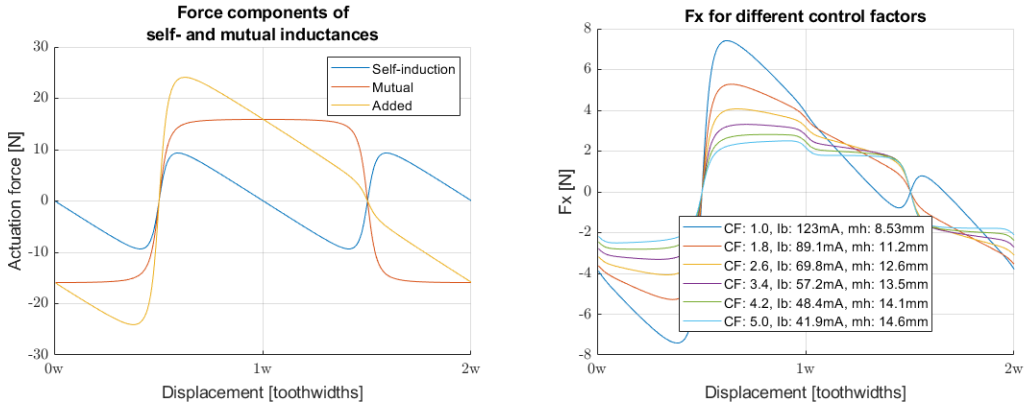

(a) Force components of actuation force.

(b) Different coil-PM MMF ratios change each one's contribution.

Figure 7.2: Forces generated by the coil and mutual coil-PM induction. Their ratio determines the shape of the motor characteristic. Extra forcer positions where no actuation force is generated occur if the coil force becomes bigger than the mutual coil-PM force.

- A large mutual force contribution leads to a block shaped actuation force with a high stiffness.
- A high coil force contribution will lead to a more sawtooth shaped actuation force with a lower stiffness, but a higher peak force and power density.
- If the coil force becomes bigger than the mutual force, extra forcer positions where $Fx = 0$ occur, as shown in figure 7.2a.

Different tooth shapes lead to vastly different motor behaviours. Triangular teeth generate the highest cogging and are deemed best for the filter application. Filleted teeth have the highest power density, with some fillet radii generating almost no cogging. This makes them promising for applications that require smooth motion.

- Triangular teeth generate the highest cogging force, but have the lowest power density. Their normal force is also lowest of all teeth shapes. This makes them suitable for filter wheel applications, where a high cogigng force is more important than a high power density. The low normal force helps to create a long bearing life time.
- Filleted teeth have the highest power density and peak force of all teeth shapes. Depending on fillet radius they can generate almost none, or a high cogging. Not only does this make HLSM suitable for applications that require smooth motion, this tooth shape might be useful in standard SRMs as well. The cogging force magnitude is very sensitive to fillet radius. Their peak to peak normal force is highest of all teeth, which puts extra stress on the central bearing.

Several design rules for optimal motor performance have been found.

- The higher the yoke material saturation limit, the higher the power density.
  At higher maximum flux densities, reluctance of the yoke and platen decreases for the same material volume. More current then increases $\partial E/\partial x$ and therefore force.
- An optimal design scales the pole surface area so teeth are at saturation flux density.
  A larger pole surface area will lower the reluctance of the air gaps, which increases energy and force in the system. If the surface area becomes too big, the reluctance becomes so low that magnetic coenergy becomes constant for all forcer positions. $\partial E/\partial x$ then decreases and so will the cogging and actuation force.
- Actuation force can be sacrificed for a higher cogging by using yoke material with a lower magnetic permeability. At low permeabilities the difference in reluctance between the inner and outer poles will generate an extra, unwanted force with a period of one pitch length.
- Power density and peak force are highest when the coil and mutual coil-PM force contributions are equal. The MMF ratio required for this changes with air gap length. The exact ratio at which this occurs is best determined using FEA.
- Power density may be increased by increasing the air gap length.
  The increased coil and magnet MMF that a larger air gap requires increase actuation force faster than $\partial L/\partial x$ will decrease. In reality $\partial L/\partial x$ will decrease faster than in the model, because the difference in gap lengths between in and out of phase becomes smaller. Depending on how the coil volume scales with coil MMF, and how fast $\partial L/\partial x$ decreases, the highest power density may thus be achieved using a medium length air gap. Further research will have to clarify what combination of PM MMF, coil MMF and air gap yield the highest power density.
- Electrical efficiency goes up with magnet size, becuase a larger part of the work is done by the magnet. This increase is limited by increasing cogging forces, until the actuation force is no longer usable.
- The optimal tooth width/air gap gap length ratio for actuation force lies between 8 and 11. If the ratio becomes lower, flux will start crossing the gaps between teeth and actuation force will drop. It is unclear how this is influenced by flux density, and whether this ratio applies when coil and PM MMF increase with air gap.

8

Concept design

A concept filter wheel design with a RHLSM actuator into its structure is proposed. This design serves as a showcase for what is possible with hybrid linear stepper motors and filter wheels. Requirements and legacy design are taken from proprietary company documents and will not be shared.

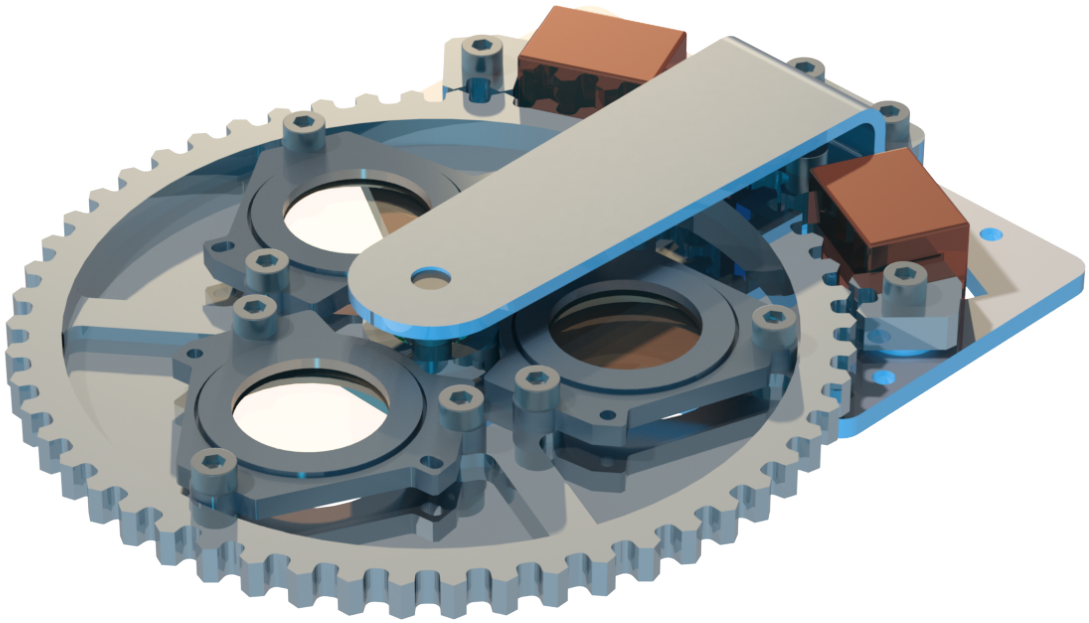

Figure 8.1: The filter wheel concept with integrated rotational hybrid linear stepper motor.

8.1. Concept design

The proposed design has several key focus areas: simplicity of design, ease of manufacturing and compatibility with current hardware. The programme of requirements of the literature review has put several requirements on the actuation and cogging forces. Based on these force requirements, the analytical model is run and FEA studies are done to find the design parameters required. Because of the large deviation between FEA and measured results, a safety factor of 4 is applied for actuation and cogging forces. In the proposed FSO terminal, the time to rotate the filter wheel is 10 seconds. The actuation force required is therefore very litte and dominated by the central bearing's friction. This makes reaching the required cogging force magnitude the main challenge.

- **Peak cogging magnitude 1.25N (0.33N required)**
  Based on an estimated filter wheel weight and a 1% mass imbalance, a 100g static acceleration requires this minimum braking force to prevent filter wheel rotation during launch Most of the braking force is provided by the bearing friction. A lower friction will require a higher cogging force.
- **Peak actuation force 4.8N (1.2N required)**
  Determined by wheel mass, bearing friction and actuation time with safety factors. This is dominated by the bearing friction, so may reduce significantly.
- **Volume of <285**cm^2
  This is the legacy design envelope.

These requirements lead to several key design decisions:

- **A high PM/coil MMF ratio**
  This will lead to a motor with a high cogging and electric efficiency.
- **Large triangular teeth**
  Large, triangular teeth yield the highest cogging of all tooth shapes.
- **One-sided forcer**
  This is the simplest construction. The normal force will also put a constant load on the bearing system, which can act as a radial preload to eliminate play. The wheel axle is supported on both ends so that the axle supports can remain thin.
- **Monolithic wheel**
  Making the teeth, spokes and hub of the filter wheel of one material eliminates different CTE's conflicting during large temperature swings. It also simplifies manufacturing and assembly of the system.
- **Lower number of coil turns with a higher current**
  For the same NI product, having fewer coil turns means a lower coil induction. This reduces harmful voltage spikes during commutation.

8.2. Dimensions and expected performance

The power requirements lead to the following concept design dimensions:

Table 8.1: Dimensions of the concept design.

Dimension	Value
Machine depth	5mm
Teeth	2x3mm
Magnet size	20x5x5mm
Air gap	.1mm
Coil turns	400
Coil current	3A

Output was verified using the FEA code of the parameter sweeps:

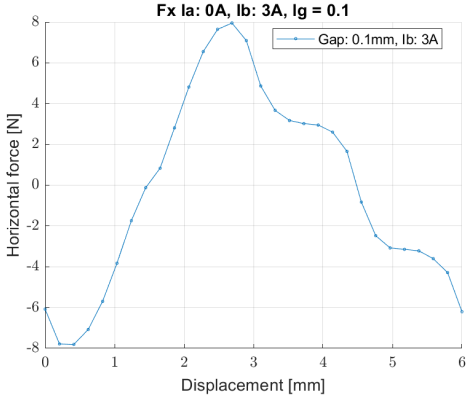

Figure 8.2: Actuation force.

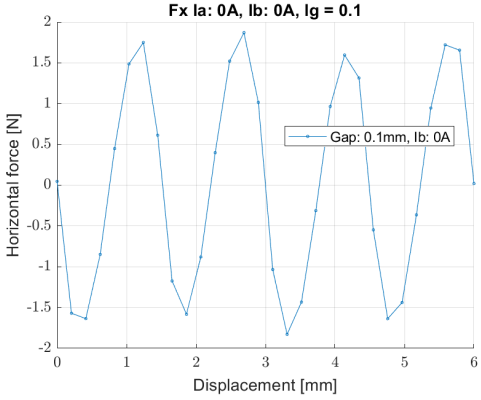

Figure 8.3: Cogging force.

Figure 8.4: Expected actuation and cogging forces of the concept design. Normal force between rotor and forcer is 51N and is not shown.

The concept design scores the following on metrics.

Table 8.2: Table with metrics of the concept design.

	Peak FX [N]	FX work done [J]	Peak FY [N]	P2p FY [N]	Stable stiffness [N/m]	Unstable stiffness [N/m}	FXwork/volume [J/m3]
Cogging	1.87	0.007	30.66	3.65	9.9E3	6.333E3	55.6
0.3A	7.95	0.025	51	18	1.2E4	1E4	176

8.3. CAD model renders

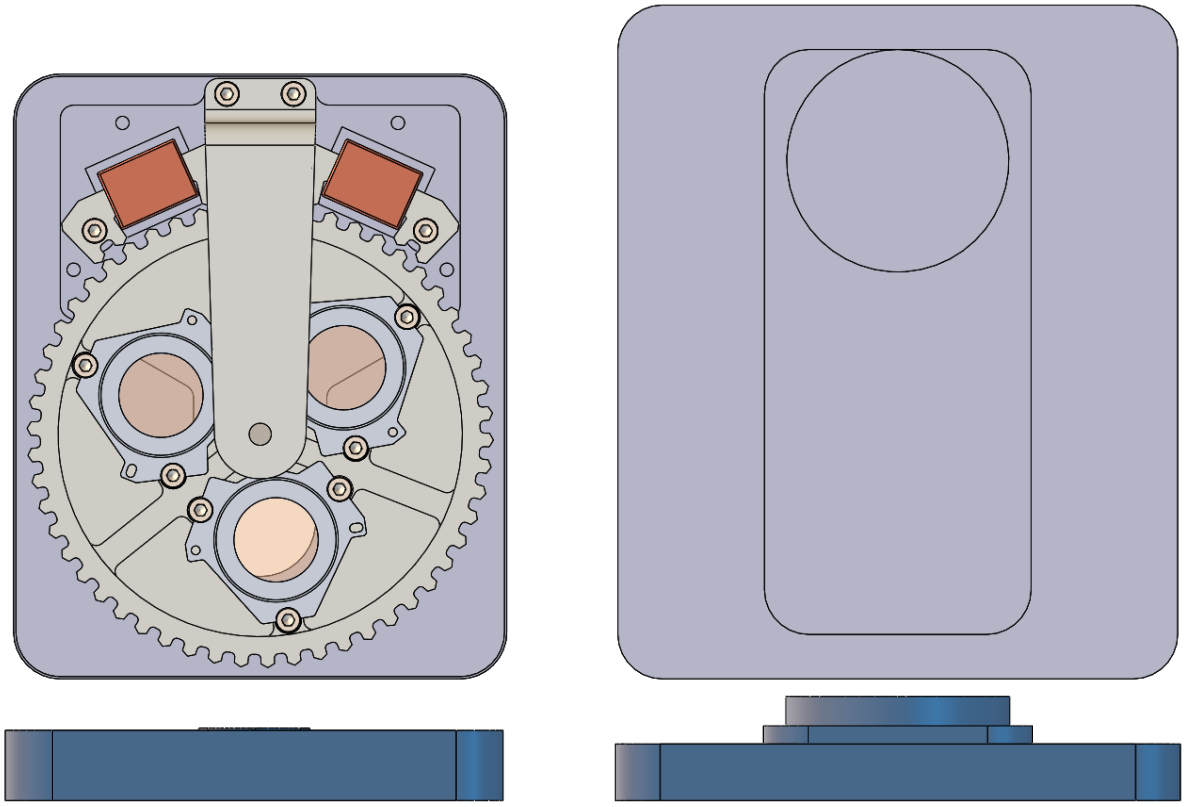

Figure 8.5: Top and side views of the concept design. The legacy design envelope is shown on the right. Even with a safety factor of 4 for actuation and cogging force, the RHSLM actuator leads to a smaller system.

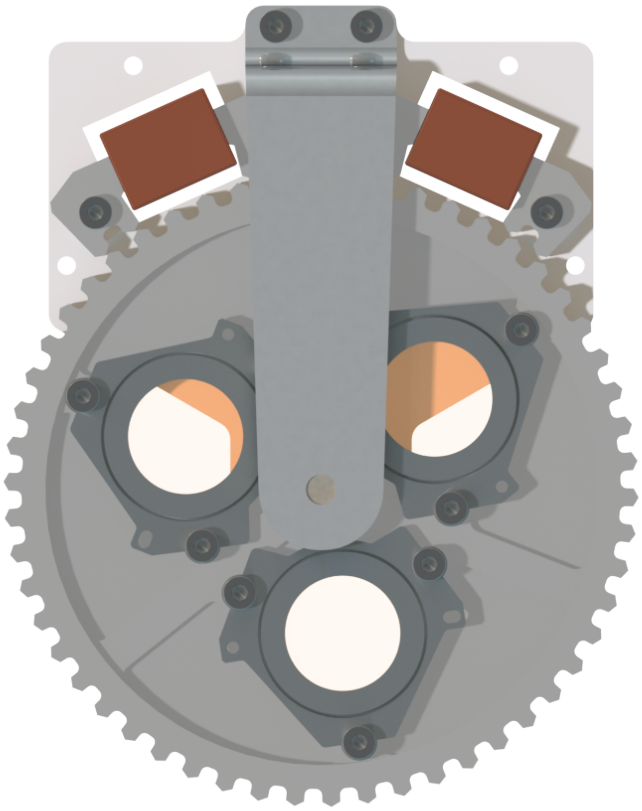

Figure 8.6: Top view of the concept design.

9

Conclusion

Is rotating a filter wheel using an integrated HLSM a viable system architecture for filter wheels and possibly other space-based mechanisms?

The RHLSM driven filter wheel is a mechanically simple, robust and compact design. The design shows great potential for a long life time and component cost reduction, and might find use in applications beside filter wheels as well.

A RHLSM's unique properties are best utilised in mechanisms that move in discrete steps, and have long periods of inactivity interspersed with short motions. The cogging force will then hold the wheel in position during vibrations or external motion.

However, the cogging force in a RHLSM is generated by hard to model effects such as fringing, flux density, material saturation and air gap reluctance. Predicting a motor's cogging force output is therefore best done using FEA, wich is time consuming. The cogging force output in the FEA and breadboard proved highly sensitive to tooth shape deviation and mounting errors.

For the category of discrete motion applications the RHLSM is a versatile, scalable design. The motor characteristic can be easily adjusted by changing the ratio between flux generated by the permanent magnet and flux generated by the coils. The actuation and cogging force magnitude is easily scaled by increasing current, pole area and magnet size.

The shape of the teeth has a very large impact on the motor characteristic. Triangular teeth generate the highest cogging force and are therefore deemed best for the filter wheel application. Filleted teeth show promise for yielding a higher power density and generating almost no cogging. The resulting smooth force/displacement curve makes the hybrid linear stepper motor suitable for a multitude of other applications.

Several design rules for optimal motor performance have been found.

- The higher the yoke material saturation limit, the higher the potential power density.
- An optimal design has a coil and magnet MMF that has teeth at saturation flux density. A higher MMF wil only increase cogging.
- Electrical efficiency goes up with magnet size, until the increased cogging makes the actuation force no longer usable.
- Power density and peak force are highest when the coil and mutual coil-PM force contributions are equal.
- Power density may be highest at a medium length air gap. Further study will have to clarify this.
- The optimal tooth width/air gap length ratio for actuation force lies between 8 and 11. It is unclear how this is influenced by flux density, and whether this ratio applies when coil and PM MMF increase..

9.1. Further research and recommendations

Several findings in this report warrant further investigation.

- Filleted teeth show promise for a higher peak force, power density, a smoother motor characteristic and lower cogging. A further study can investigate at what radius the generated actuation force generated is highest, how this works and what this means for cogging. The results will be important for all electric motor designs, as reducing cogging is a much researched topic in the field.
- The analytical model indicates that power density may be highest at a medium length air gap. A further study can clarify what magnet MMF, coil MMF and air gap yield the highest power density.
- The effect of magnetisation of the yokes has not been investigated. The high flux densities used to induce fringing will permanently magnetise the yokes. The direction of magnetisation will influence the shape of cogging seen in the motor. Because the direction is reversed every other step, the motor experiences a maximal magnetic hysteresis, fully traversing the hysteresis loop every phase. This can lead to eddy current losses and heating of the yoke iron.
- The effect of the shape of the material's magnetisation curve on the motor characteristic has not been researched. The permeability of the material might have a large influence on the cogging.
- Viorel and Szabo note that there is an optimum slot/pitch ratio for actuation force production [17]. The effect of different slot widths on the force generation is left out of this study.
- A better motor architecture could be designed that does not have different reluctances for the inner and outer poles.
- Commutation strategies have not been investigated in this study. Only one coil was energised at constant current. Further research may quantify the effect of simultaneous coil powering, microstepping or torque sharing functions.

Bibliography

[1] Raga Ahmed. “Variable-Reluctance Motors in Controlled Linear Motion Applications Variable-Reluctance Motors in Controlled”. PhD thesis. Atlanta: Georgia Institute of Technology, 2013.

[2] Ioana Benția, Loránd Szabó, and Mircea Ruba. “On a rotary-linear switched reluctance motor”. In: *SPEEDAM 2012 - 21st International Symposium on Power Electronics, Electrical Drives, Automation and Motion* June (2012), pp. 507–510. ISSN: 01406736. DOI: 10.1109/SPEEDAM.2012.6264442.

[3] Charles S. Clark and Béla I. Privári. “NIRCam cryo filter wheel assembly design and performance”. In: September 2013. Palo Alto: Lockheed Martin Space Systems Company - Advanced Technology Center, 2013, 88630E. DOI: 10.1117/12.2024462. URL: http://proceedings.spiedigitallibrary.org/proceeding.aspx?doi=10.1117/12.2024462.

[4] Tesat-Spacecom GmbH & Co. *TESAT Laser products*. 2019. URL: http://www.tesat.de/en/products/laser-products.

[5] A.J. Coates et al. “The PanCam Instrument for the ExoMars Rover”. In: *Astrobiology* 17.6-7 (2017), pp. 511–541. ISSN: 1531-1074. DOI: 10.1089/ast.2016.1548. URL: http://online.liebertpub.com/doi/10.1089/ast.2016.1548.

[6] Uday S. Deshpande, Jimmie J. Cathey, and Eike Richter. “High-Force Density Linear Switched Reluctance Machine”. In: *IEEE Transactions on Industry Applications* 31.2 (1995), pp. 345–351. ISSN: 19399367. DOI: 10.1109/28.370283.

[7] Faulhaber. *The 3D view of Mars*. URL: https://www.faulhaber.com/en/markets/aerospace-aviation/mars-rover/ (visited on 07/07/2019).

[8] A E Fitzgerald, Charles Kingsley, and Stephen D Umans. *Electric Machinery Sixth Edition McGraw-Hill Higher Education*. 7th ed. New York, NY: McGraw-Hill, 2003, p. 27. ISBN: 0073660094.

[9] Andrew S. Gibson et al. “Life-Test Investigation and Status of the Niriss Dual Wheel Cryogenic Mechanism for Jwst”. In: *Conference proceedings of the 15th European Space Mechanisms & Tribology Symposium* September (2013), pp. 25–27. URL: http://www.esmats.eu/noordwijk/index.php.

[10] Rory Holmes et al. “A filter wheel mechanism for the Euclid near-infrared imaging photometer”. In: July 2010. San Diego: Max-Planck-Institut f¨ur Astronomie, K¨onigstuhl 17, 69117, Heidelberg, Germany, 2010, 77391A. DOI: 10.1117/12.856941. URL: http://proceedings.spiedigitallibrary.org/proceeding.aspx?doi=10.1117/12.856941.

[11] Chang Chou Hwang, Ping Lun Li, and Cheng Tsung Liu. “Design and analysis of a novel hybrid excited linear flux switching permanent magnet motor”. In: *IEEE Transactions on Magnetics* 48.11 (2012), pp. 2969–2972. ISSN: 00189464. DOI: 10.1109/TMAG.2012.2195716.

[12] Stefan Kuiper. *European space-grade stepper motor suppliers*. Delft, 2019.

[13] J. F. Pan, Yu Zou, and Guangzhong Cao. “An asymmetric linear switched reluctance motor”. In: *IEEE Transactions on Energy Conversion* 28.2 (2013), pp. 444–451. ISSN: 08858969. DOI: 10.1109/TEC.2013.2252178.

[14] Edmond R. Pelta. “Two-Axis Sawyer Motor for Motion Systems”. In: *IEEE Control Systems Magazine* 7.5 (1987), pp. 20–24. ISSN: 02721708. DOI: 10.1109/MCS.1987.1105362.

[15] Rudolf Saathof et al. “Optical technologies for terabit/s-throughput feeder link”. In: *2017 IEEE International Conference on Space Optical Systems and Applications, ICSOS 2017* (2018), pp. 123–129. ISSN: 10543139. DOI: 10.1109/ICSOS.2017.8357221.

[16] Rudolf Saathof et al. “TNO optical communications space terminals - Current projects and future plans”. In: *2017 IEEE International Conference on Space Optical Systems and Applications, ICSOS 2017* (2018), pp. 255–259. DOI: 10.1109/ICSOS.2017.8357401.

[17] Lorand Szabo et al. *Hybrid Linear Stepper Motors*. June 1998. Cluj-Napoca: MEDIAMIRA, 1998. ISBN: 9739358128.

A

A criterion for stable motor behaviour and implementing different reluctance models

A.1. Deriving a criterion for stable motor behaviour

The occurrence and rotor positions where no actuation force is generated can be analytically derived. This derivation shows us what design parameters lead to a usable force/displacement curve, and if any parameter combinations should be avoided. This parameter combination can be considered the first design rule of hybrid linear stepper motors.

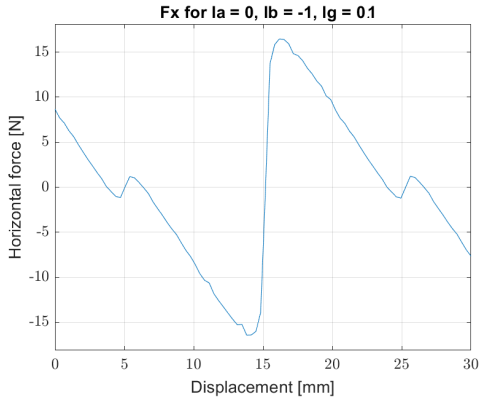

Figure A.1: Actuation force from the literature study's FEA. At $x = 5$ and $x = 25$ the forcer is in an unstable neutral position, because it experiences no force and a negative stiffness. Around these points are stable neutral positions, but they change with coil and magnet MMF. This makes it impossible to determine to what position the forcer will move.

Since force is the derivative of coenergy with respect to displacement, no force is produced when:

$$F_x = \frac{d}{dx} W_f = 0 \tag{A.1}$$

Because all terms without i_b drop out, we can write this as:

$$\frac{1}{2}\frac{\partial}{\partial x} L_b\, i_b^2 + \frac{1}{2}\frac{\partial}{\partial x} L_{bpm}\, i_b\, i_{pm} = 0 \tag{A.2}$$

With coil B inductance defined as:

$$L_b = \frac{N_b^2}{R} = \frac{N_b^2}{R_3 + R_4} \tag{A.3}$$

Mutual induction of coil B and magnet is the magnet flux through coil B

$$L_{bpm} = \frac{N_b}{i_{pm}} \Phi_{4,pm} \tag{A.4}$$

$\Phi_{4,pm}$ is the part of the magnet flux passing through pole 4. This can be calculated with the total magnet flux times the reluctance fraction of pole 4 over the total reluctance of poles 3+4.

$$\Phi_{4,pm} = \Phi_{pm} \frac{R_3}{R_3 + R_4} \tag{A.5}$$

Total magnet flux is:

$$\Phi_{pm} = \frac{H_c l_m}{R_{pmcircuit}} \tag{A.6}$$

Substitute into A.5:

$$\Phi_{4,pm} = \frac{H_c \, l_m}{R_{pmcircuit}} \frac{R_3}{R_3 + R_4} \tag{A.7}$$

Writing out terms for mutual induction:

$$L_{bpm} = \frac{N_b}{i_{pm}} \frac{H_c \, l_m}{R_{pmcircuit}} \frac{R_3}{R_3 + R_4} \tag{A.8}$$

We can then insert our expressions for inductance in the coenergy equation:

$$W_f = \frac{1}{2} \frac{N_b^2}{R_3 + R_4} i_b^2 + \frac{1}{2} \frac{N_b}{i_{pm}} \frac{H_c \, l_m}{R_{pmcircuit}} \frac{R_3}{R_3 + R_4} i_b \, i_{bpm} \tag{A.9}$$

Which simplifies to:

$$W_f = \frac{1}{2} \frac{N_b^2}{R_3 + R_4} i_b + \frac{1}{2} N_b \frac{H_c \, l_m}{R_{pmcircuit}} \frac{R_3}{R_3 + R_4} \tag{A.10}$$

Equating the derivative of coenergy to zero as in equation A.2:

$$\frac{d}{dx}\left(\frac{1}{2} \frac{N_b^2}{R_3 + R_4} i_b + \frac{1}{2} N_b \frac{H_c \, l_m}{R_{pmcircuit}} \frac{R_3}{R_3 + R_4} \right) = 0 \tag{A.11}$$

Taking out the constants and reordering terms:

$$N_b \, i_b \frac{d}{dx}\left(\frac{1}{R_3 + R_4} \right) = -\frac{d}{dx}\left(\frac{H_c \, l_m}{R_{pmcircuit}} \frac{R_3}{R_3 + R_4} \right) \tag{A.12}$$

If we assume the reluctance of the PM is dominated by the magnet length as in $R_{pm} >> R_{gaps}$, R_{pm} remains constant for all x and we can take it out of the derivative:

$$N_b \, i_b \frac{d}{dx}\left(\frac{1}{R_3 + R_4} \right) = -\frac{H_c \, l_m}{R_{pmcircuit}} \frac{d}{dx}\left(\frac{R_3}{R_3 + R_4} \right) \tag{A.13}$$

If $R_{pm} >> R_{gaps}$, then we can simplify $R_{pmcircuit}$:

$$R_{pmcircuit} \sim \frac{l_m}{\mu_m A_m} \tag{A.14}$$

This allows us to simplify expression A.13:

$$N_b \, i_b \frac{d}{dx}\left(\frac{1}{R_3 + R_4} \right) = -\frac{H_c \, l_m}{\frac{l_m}{\mu_m \, A_m}} \frac{d}{dx}\left(\frac{R_3}{R_3 + R_4} \right) \tag{A.15}$$

$$N_b i_b \frac{d}{dx}\left(\frac{1}{R_3 + R_4}\right) = -\mu_m H_c A_m \frac{d}{dx}\left(\frac{R_3}{R_3 + R_4}\right) \tag{A.16}$$

The left side is the force generated by the self-inductance of the coil. The right side is the force generated by the mutual inductance of the coil and magnet. Stability is guaranteed when the force of coil B does not exceed that of the mutual indunction. If we rearrange the terms we can derive a rule for stable motor behaviour:

$$N_b i_b \frac{d}{dx}\left(\frac{1}{R_3 + R_4}\right) < \mu_m H_c A_m \frac{d}{dx}\left(\frac{R_3}{R_3 + R_4}\right) \tag{A.17}$$

If these terms are equal the tangential force/displacement curve is linear, having the highest possible peak force. Note that this derivation only holds when the reluctance of the permanent magnet circuit is very high relative to the gaps and does not vary with forcer position. The parameters of the power ratio determine the shape of the F_x/x curve. Isolating the design parameters from equation A.1 gives:

$$\frac{\frac{d}{dx}\left(\frac{1}{R_3 + R_4}\right)}{\frac{d}{dx}\left(\frac{R_3}{R_3 + R_4}\right)} = \frac{\mu_m H_c A_m}{N_b i_b} \tag{3.2}$$

The left side is the dubbed *dRatio* and is the ratio of coil B's self- and mutual inductance changes. The right side is subbed *MMF ratio* and is a measure for magnet to coil MMF. If the dRatio and MMF ratio are equal, linear motor behaviour is achieved. If the MMF ratio increases or the dRatio decreases, the F_x/x becomes more block wave as in shown in figure 3.10. Increasing the air gap decreases the dRatio and thus shifts the motor characteristic away from instability. The dRatio depends on the reluctance model used, and since reluctance is highly non-linear and hard to predict will likely have to be determined by experiment. Nevertheless this inequality can be considered a design rule for HLSM motors.

A scale factor (CF) is introduced that scales the MMF ratio up. This increases the mutual induction's force component to create different motor behaviours.

$$MMF\,ratio = cf\frac{\mu_m H_c A_m}{N_b i_b} \sim cf\frac{B_r A_m}{N_b i_b} \tag{A.18}$$

In this model coil B current and magnet height are scaled as the two free variables with which to tune MMF ratio the shape of the Fx/x curve.

An algorithm has been written that finds the MMF ratio for a linear F_x/x. Because saturation is not taken into account, the current and magnet height are then scaled up or down with a fixed ratio so that the maximum flux density of poles 3 and 4 stays under a predetermined value. The algorithm works as follows:

1. Calculate model with input settings. This gives the reluctance of the poles throughout the phase.
2. Calculate $dRatio$ with the reluctance model used and input parameters.
3. Calculate design parameters for linear behaviour from values of $dRatio$.
4. Scale magnet height until $MMFratio = cf * drRatio$
5. Scale current and magnet height with MMF ratio until correct flux density is achieved:
   (a) Recalculate model with magnet height and current taken from calculated desired MMF ratio
   (b) Check if $(B_3 - B_{max}) < 0.01 \wedge B_4 - B_{max} < 0.01$ for all x
   (c) Scale current and magnet height up or down until $B_3 = B_{max} \vee B_4 = B_{max}$

By changing the control factor in the optimisation loop we can test various combinations of PM and coil flux, at the same maximum flux density. This allows us to compare different flux ratios on metrics such as work done, peak force, and power density of the motor.

A.2. Continuous expressions for overlap and reluctance

Implementing different reluctance models requires continuous expressions for all variables, such as pole-platen tooth overlap area. Overlap varies linearly with x when going in or out of phase. This looks like a triangular wave, modelled as:

$$A(x) = A_{max} * T(x) \tag{A.19}$$

With $T(x)$ a triangle wave that varies between $0..1$. To avoid dividing by zero, $T(x)$ will be scaled to range from $0.001…1$. The function used for this approximation is:

$$T(t) = \frac{acos(\lambda\, sin(t + \frac{\pi}{2}))}{\pi} \tag{A.20}$$

$T(t)$ is a triangle wave that varies from 0 to 1. λ determines the rounding of the corners. if $\lambda = 1$, the function has hard edges. If lambda decreases slightly, the wave will have rounded corners, while the maximum $\frac{ds}{\partial x}$ changes little. The main advantage over a numerically generated triangle wave is that this function is continuously differentiable. A value of $\lambda = 0.99$ is chosen.

Reluctance is modeled using function $R(x)$ that modulates a base reluctance between R_{min} and R_{max}. The function $R(x)$ can be arbitrary, but has to fulfill several criteria. The most important one criterion is that the function may not add up to a constant value when it is phase shifted 90° from itself. The sine function fails this criterion:

$$sin(t) + sin(t + \pi) = 0 \tag{A.21}$$

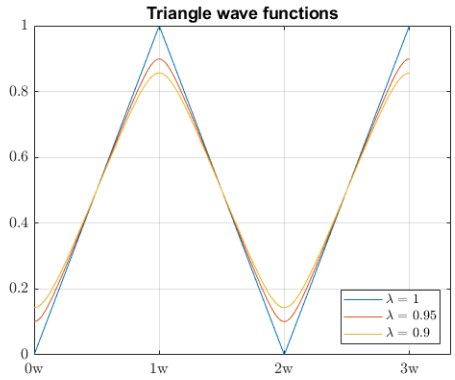

Figure A.2: Decreasing λ values give the triangle wave $s(t)$ rounded corners.

Using sine functions to model reluctance leads to constant PM inductance and therefore no cogging. FEA studies shown in figure 2.8b show that actuation forces in the system are continuous and without instant force jumps. As force is generated by the derivative of the reluctance, any modeling function should also be continuously differentiable. Together this leads to several criteria for a reluctance modeling function:

1. Periodic with period 2π.
2. Symmetric around $x = \pi$.
3. Varies between $0..h$ on interval $x = 0..\pi$.
4. $f(x) + f(x + \pi) \neq c$ or $f(x)' + f(x + \pi)' \neq 0$.
5. Continuously differentiable.

The reciprocal-of-overlap model is implemented with:

$$f(x) = 1/s(t)^{1+\delta} \tag{A.22}$$

$$s(t) = \frac{acos(\lambda\, sin(t + \frac{\pi}{2}))}{\pi} \tag{A.23}$$

With $s(t)$ the triangle wave shown in equation A.20. For $\delta = 0$ this function yields the standard reciprocal-of-overlap reluctance model as explained by Fitzgerald, with reluctance varying between $\frac{l_g}{\mu_0 A}$ and infinity. The rounding factor λ determines the sharpness of the force jumps seen this generates. δ can be increased to deviate from the ideal reciprocal.

The sine reluctance model is implemented as:

$$f(x) = A\, sin^{2+\delta}\frac{t}{2} \tag{A.24}$$

This function will yield a reluctance model that varies sinusoidally between R_{min} and $A * R_{min}$.
δ can be increased or decreased to let the reluctance deviate from an ideal sinusoid. The amplitude is set at a starting value of 8.

If $\delta = 0$, both functions do not satisfy criterion 4. By increasing δ, the reluctance of the PM flux loop will start to fluctuate more and more, which will yield cogging. The effect of the delta factor on total reluctance is only small, as can be seen in figures A.3. If a small value for δ already generates a high cogging, it means that our HLSM prototype will be very sensitive to manufacturing errors, as even a small deviation of the intended reluctance profile will show up in the force/displacement characteristic.

A.3. Modelling fringing using non-linear reluctance functions

The reciprocal-of-overlap and sine reluctance models are shown in figure A.3. Fringing around teeth can be approximated by inserting a small non-linearity in the tooth reluctance functions. The strength of this non linearity can be controlled by the parameter δ. Figure A.4 shows that the effect of δ is small compared to the magnitude of the reluctance itself.

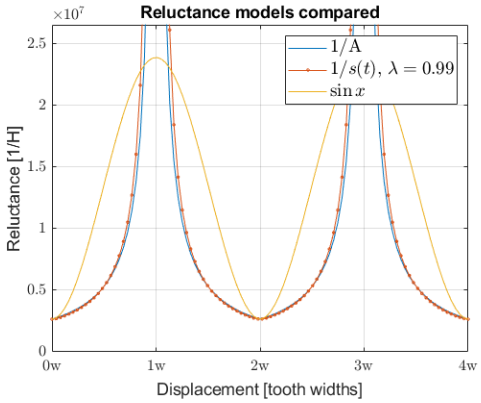

Figure A.3: Three different reluctance models compared: the standard reciprocal-of-overlap model $R = \frac{l_g}{\mu_0 A}$, the approximation thereof using a continuously differentiable function for overlap A, and the sine reluctance model.

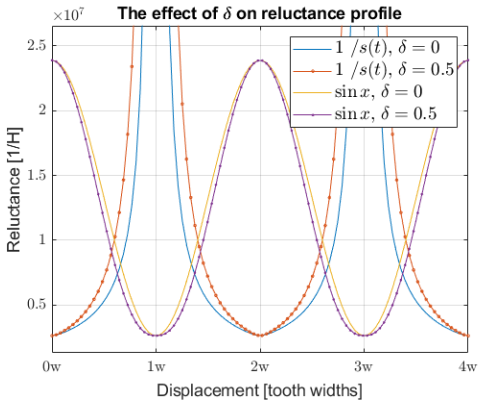

Figure A.4: A non-linearity can be introduced to the $f(t)$ reluctance models by adding a small value δ to the exponential. The effect of δ has on the overall magnitude of reluctance values is small.

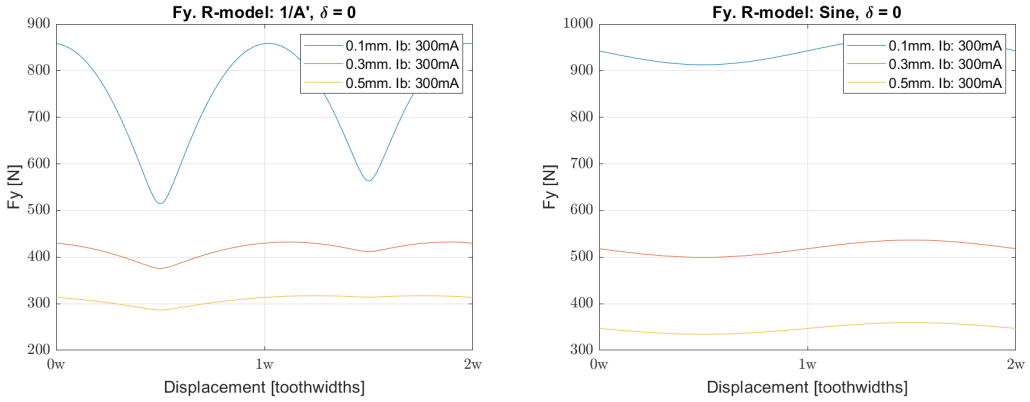

(a) 1D flux tube model.

(b) Sine model.

Figure A.5: Normal forces for reciprocal-of-overlap and sine reluctance models.

Normal force of both models shown in figure A.5, and is much higher than FEA predicts (the FEA data is not shown). This is likely due to fringing lowering flux densities around the teeth. Because the coil fluxes are determined by $R1 + R2$ and $R3 + R4$, which puts two air gaps in series, it is very sensitive to a change in air gap length. Magnet flux is dominated by R_m, so will not change much if the air gap length varies. The result is that normal force drops exponentially with increasing air gap lengths, and settles on a minimum level generated by the PM.

B

FEA parameter sweep data

This appendix contains all the plots for the finite element parameter sweeps. For most parameters two sweeps are done: once without current for the cogging, and once with 0.3A on coil B. For each sweep the horizontal (actuation/cogging) and normal forces are plot.

B.1. Air gap

Cogging

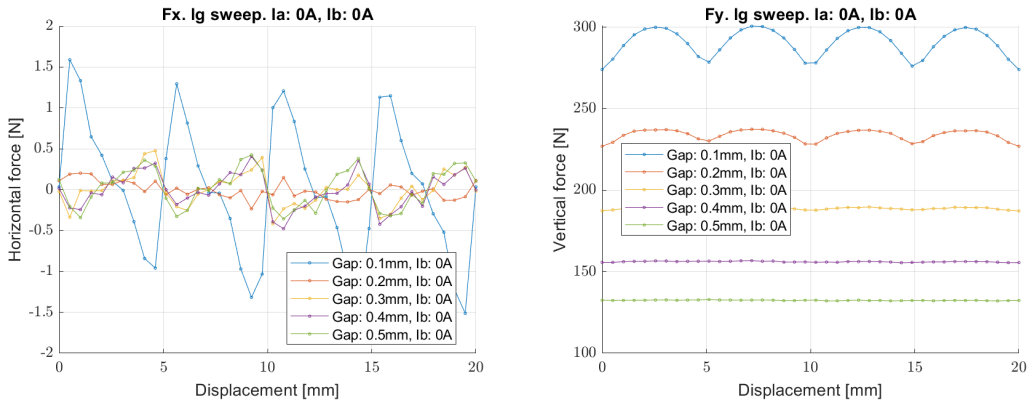

(a) Cogging force.

(b) Normal force.

Figure B.1: Air gap sweep for cogging force. Cogging drops exponentially with air gap.

Cogging reduces exponentially with air gap length. At larger gaps a small cogging opposite in phase appears with an amplitude of 0.5N. This *base cogging* will show up for some parameter configurations and is explained later. The lowest cogging amplitude is found around $l_g = 0.2$mm, because at that gap the base cogging and normal cogging combination is minimal. Normal force drops exponentially with air gap distance.

0.3A on coil B

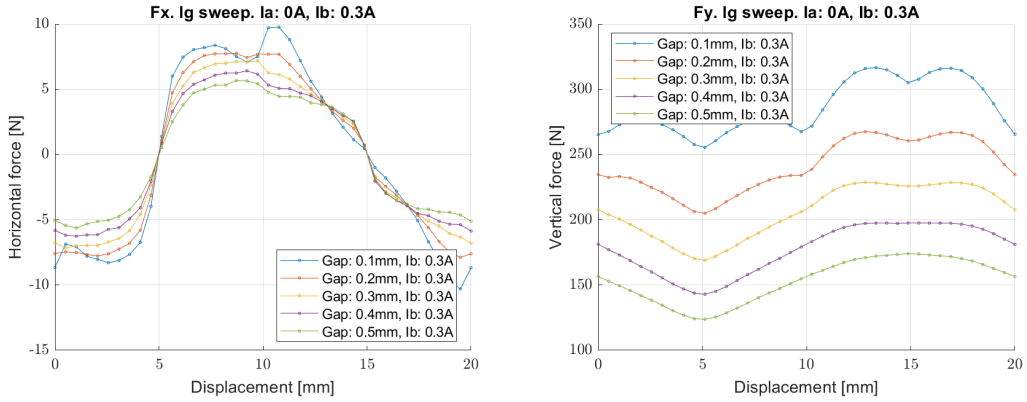

(a) Actuation force.

(b) Normal force.

Figure B.2: Air gap sweep for actuation force. Actuation force drops linearly with air gap, but the change is little.

At 0.1mm a cogging harmonic shows, which means that teeth are saturated and flux is fringing around the teeth. At larger gaps this harmonic disappears, so saturation levels are dropping. Even so, actuation force magnitude and stiffness remains high.

This confirms the findings of the analytical model shown in figure 3.1b: the stiffness in the actuation force is generated mainly by the mutual induction L_{bpm}. The mutual induction force component is insensitive to air gap, so only coil B's self-induction L_b drops with air gap. Therefore the total actuation force is relatively insensitive to air gap length.

Normal force at 0.3A decreases linearly with current, which confirms dropping saturation levels.

B.2. Magnet height

Cogging

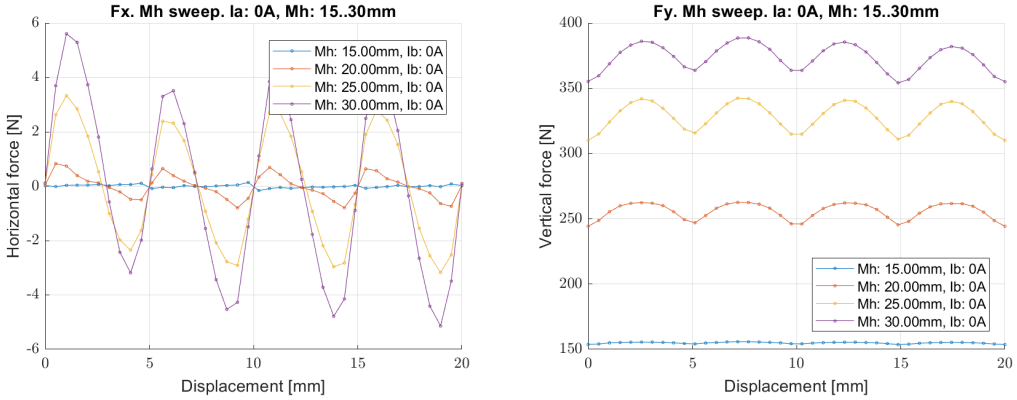

(a) Actuation force. (b) Normal force.

Figure B.3: Magnet height sweep for cogging force. Above a minimum size, cogging increases exponentially with magnet size.

Cogging only occurs from a minimum magnet surface area. This means a minimum saturation level is required before fringing effects become important. After this minimum, cogging force grows quickly until the yoke iron is fully saturated. This saturation also shows in the normal force: an exponential increase and then saturation.

0.3A on coil B

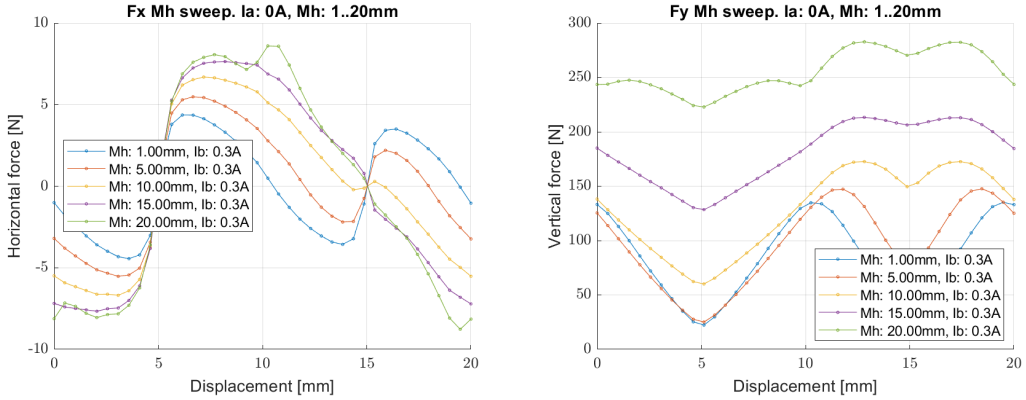

(a) Actuation force. (b) Normal force.

Figure B.4: Magnet height sweep for actuation force. Under a minimum size, extra forcer positions where $F_x = 0$ occur. Above this minimum actuation force scales linearly with magnet height.

Without magnet we can see the actuation force generated by the coil alone. This is sawtooth like and has several locations where $Fx = 0$.

This behaves the same as in the EMC, using a reciprocal-of-overlap model for reluctance: Coil B self induction L_b varies parabolically, coil B-PM mutual induction L_{bpm} is a block wave.

If the magnet grows in size, the blocky force contribution of L_{bpm} creates a stable, sine like motor characteristic. At 20x10mm magnet surface area, cogging harmonics show and actuation stops increasing with magnet size. At this point the yoke material is fully saturated.

B.3. Teeth size

In the teeth size sweep, pole area is kept constant, with successive sweeps testing increasing numbers of smaller teeth. Because the air gap distance is constant, the ratio of tooth width to air gap changes. The teeth size sweep makes use of a 30mm magnet height, so that the difference in cogging for different tooth sizes becomes more apparent. The force/displacement curves are normalised with respect to the motor phase.

Cogging

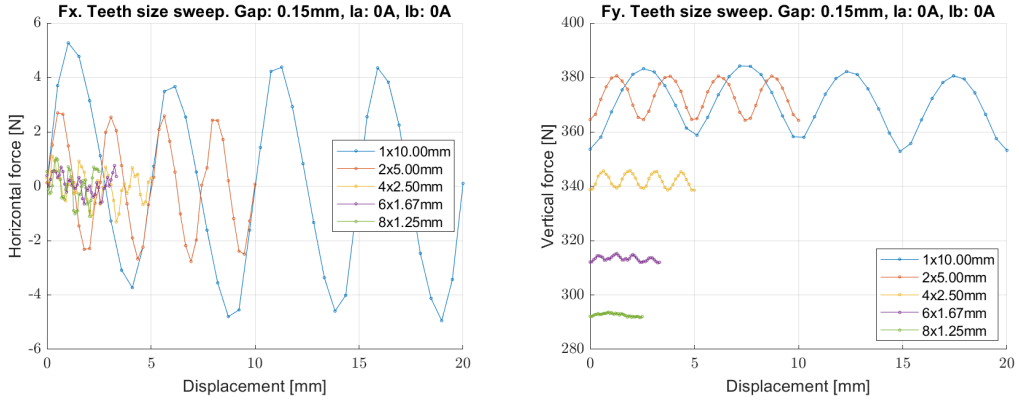

(a) Actuation force. (b) Normal force.

Figure B.5: Cogging forces of teeth size sweep.

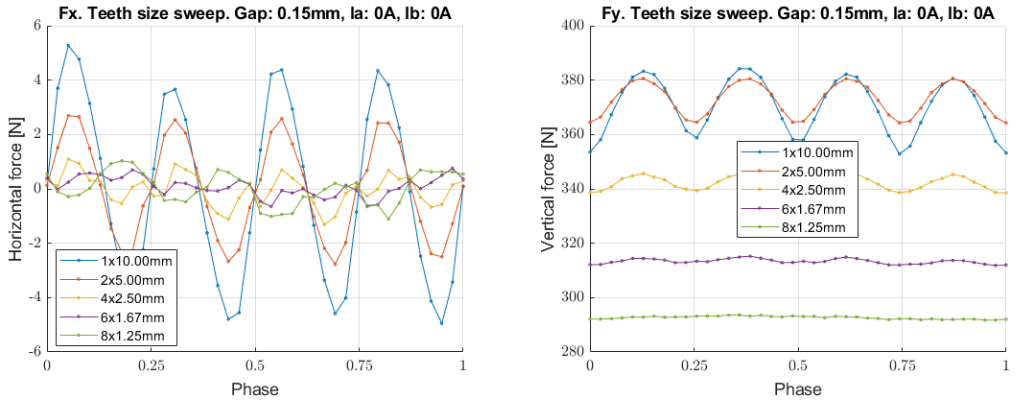

(a) Actuation force. (b) Normal force.

Figure B.6: Cogging forces of teeth size sweep with the phases normalised. Cogging drops linearly with tooth size until a small, erratic form of coggins is left.

Figure B.7: Teeh size sweep.

Cogging drops linearly with tooth width until a small, erratic form of coggings is left. This looks like base cogging caused by different reluctance paths, but also shows extra harmonics. Below 5mm tooth width, normal force also drops linearly.

The coenergy in figure B.8 shows the cause: for constant pole surface area, smaller teeth lead to a higher coenergy in the system, but also a more constant coenergy. Hence the cogging force drops.

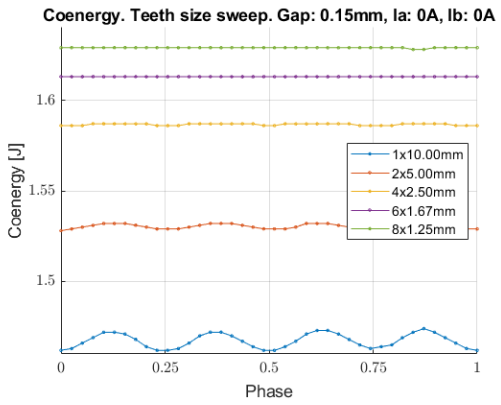

Figure B.8: Coenergy of teeth size sweep. Phases normalised.

0.3A on coil B

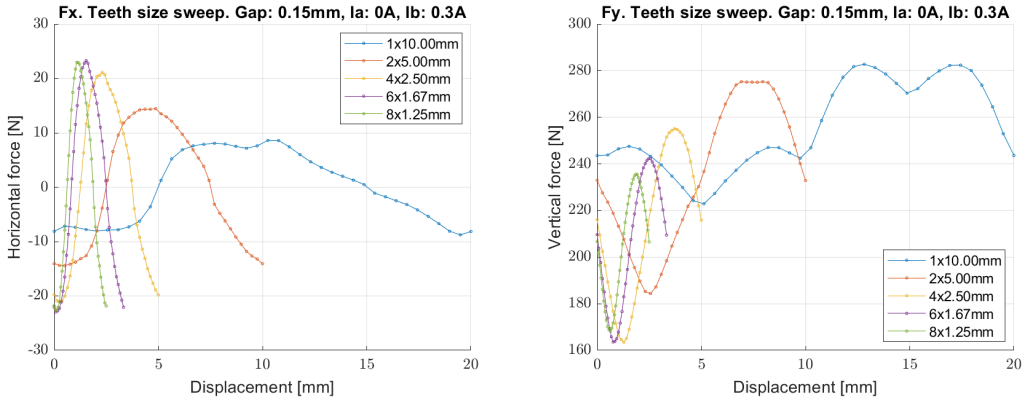

(a) Actuation force. (b) Normal force.

Figure B.9: Actuation forces of teeth size sweep at 0.3A.

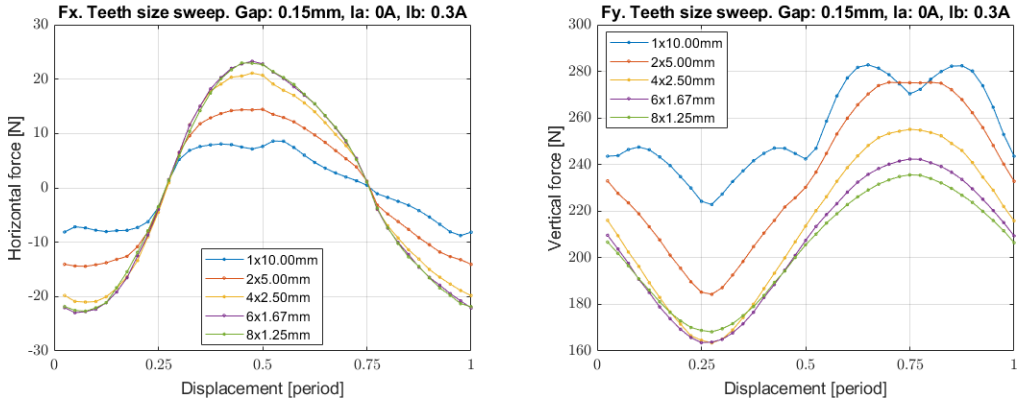

(a) Actuation force. (b) Normal force.

Figure B.10: Actuation forces of teeth size sweep at 0.3A, with phases normalised. Having more, smaller teeth increases the actuation force to an optimum.

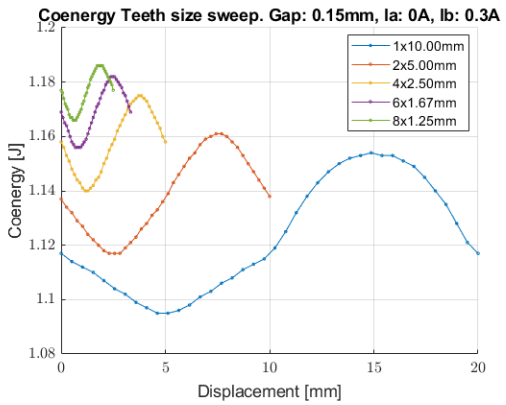

Figure B.11: Coenergy of teeth size sweep with 0.3A. $\partial E/\partial x$ increases because of the shorter motor phase.

The same plots are shown for the sweep with 0.3A on coil B. For the same pole area, having more, smaller teeth increases actuation force, because the dx in $\partial E/\partial x$ becomes smaller. Similar to the cogging, when teeth width goes to zero, $\partial E/\partial x$ will also go to zero. Below 1.7mm tooth width, the decrease of $\partial E/\partial x$ will overtake the decrease of dx, and actuation force does not increase. At infinitely small teeth, energy will be constant and no force will be generated at all. The maximum force is generated with teeth between 1.25-1.7mm wide, which corresponds to a ratio of 8-11 of tooth with to air gap length. This can serve as a rule of thumb for dimensioning HLSM motor poles. Why $\partial E/\partial x$ decreases with teeth size is investigated further in figure B.14.

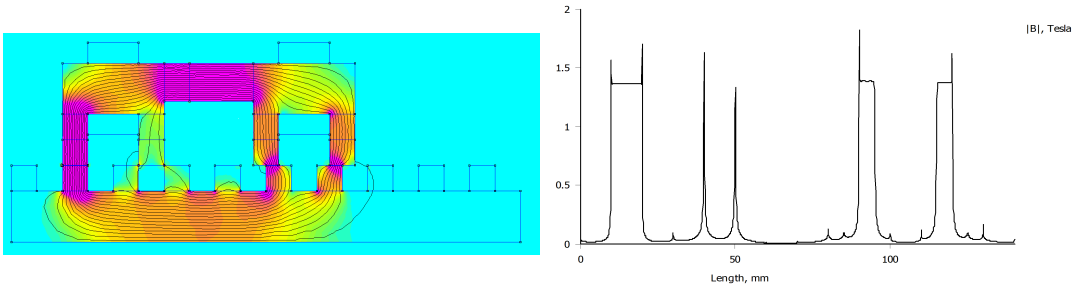

(a) Flux density of 1 tooth of 10mm wide.

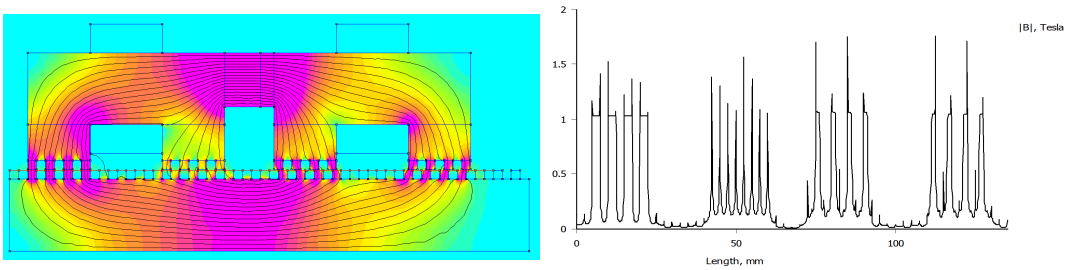

(a) Flux density of 4 teeth of 2.5mm wide.

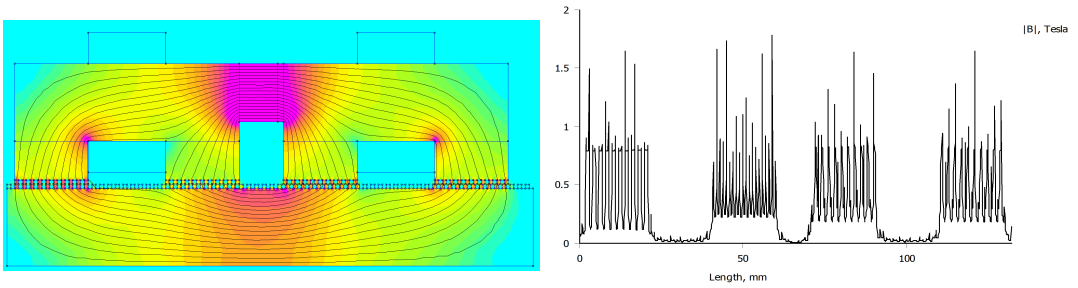

(a) Flux density of 8 teeth of 1.25mm wide.

Figure B.14: For the same pole surface area, smaller teeth lead to a lower flux density.

Smaller teeth lead to a lower overall flux density, because the flux starts crossing the air gap between the teeth. The lower reluctance leads to a higher magnetic coenergy, but the $\partial E/\partial x$ becomes smaller. Because the flux density is smaller, normal force is lower.

With tooth widths below 2mm the certain base cogging discovered earlier remains. This can be explained by the difference in the reluctance the PM flux encounters through outer poles 1 & 4 and inner poles 2 & 3. This property is a fundamental weakness of this architecture, and is also mentioned as such by Szabo and Viorel [17]. If the reluctance of the air gaps becomes smaller relative to the yoke iron reluctance, total flux flowing through poles 2 & 3 will be higher than flux through poles 1 & 4. Figure B.14a shows the inner two poles have flux flowing than the outer two.

B.4. Number of teeth

In the number of teeth sweep, extra teeth of 10mm wide are added to the pole. This linearly increases the pole surface area. As this does not influence the tooth width/air gap ratio, this sweep can also be considered a 'pole surface area sweep'.

Cogging

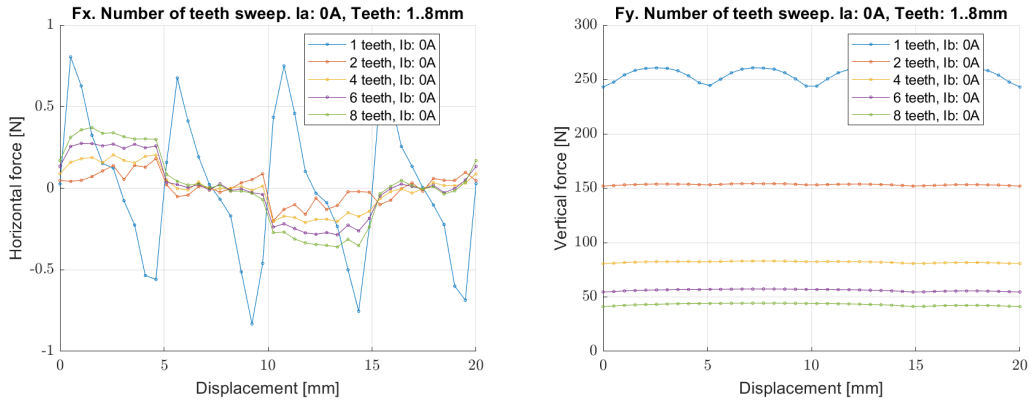

(a) Actuation Force.

(b) Normal force.

Figure B.15: Cogging with number of teeth(pole surface area) sweep. The low air gap reluctance makes yoke reluctance become important, leading to a base cogging.

With extra teeth cogging disappears and the same base cogging seen earlier is left. With increasing numbers of teeth, this base cogging becomes larger. The different reluctances of flux paths from poles 1 & 4 and 2 & 3 again explains this. From 2 teeth and up the reluctance is so low that most flux runs through poles 2 and 3. Between $x = 5..10$ and $x = 15..20$, the overlap of these poles with platen tooth is constant, leading to a constant reluctance.

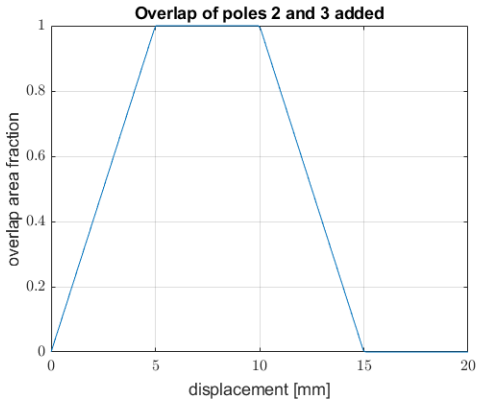

Figure B.16: Added overlap area of poles 2 and 3 from the analytical model. This makes reluctance of the inner poles' flux paths constant on some intervals.

The induction of the PM therefore remains constant and no actuation force is generated at these forcer positions. The effect grows stronger when yoke reluctance plays a larger role, which is when the pole area becomes bigger. Because the flux density lowers quicker than the flux magnitude increases, normal force also lowers with more teeth.

0.3A on coil B

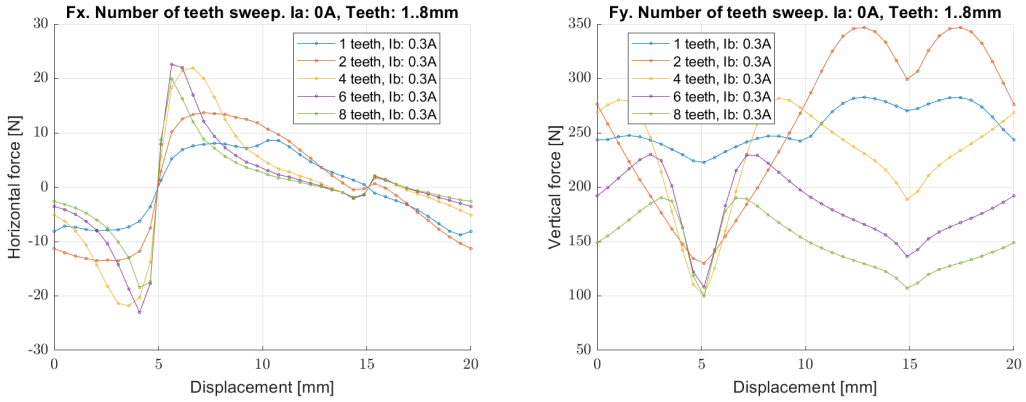

(a) Actuation Force. (b) Normal force.

Figure B.17: Actuation force with number of teeth(pole surface area) sweep. More teeth increase coil B's contribution to the actuation force until extra forcer positions with $F_x = 0$ occur.

With 0.3A in coil B we see an initial increase in actuation force, and a peak force around the point $x = 5$. At this forcer position, pole 4 is completely out of phase and coil B induction minimal. When the large number of teeth then simultaneously come into phase, coil B's induction quickly rises. Because of the large pole surface area, the energy in the system then quickly reaches the maximum value. The energy then remains relatively constant, so that actuation force drops below that of a configuration with a smaller surface area.

Since the reluctance of coil B is very low for a large pole surface area, the PM/coil MMF ratio is very low. This leads to forcer positions at $x = 13$ and $x = 17$ where $F_x = 0$, agreeing with the behaviours seen in the analytical model. At these positions the force component of the coil overpowers that of the mutual induction: $\partial L/\partial x * i_b^2 > \partial L_{bpm}/\partial x i_b\, i_m$. This can be seen better in figure B.18.

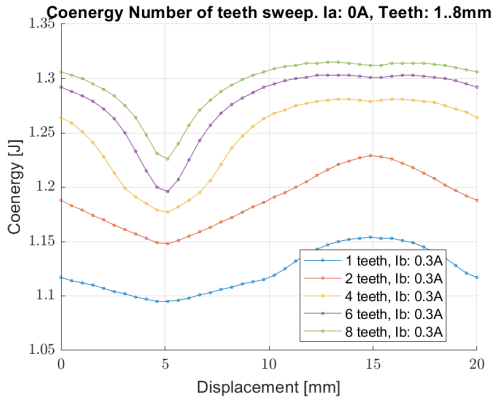

Figure B.18: Coenergy of number of teeth sweep with 0.3A. When pole surface area becomes too big, new optima appear that lead to unwanted motor behaviour.

For more than two teeth the coenergy shows a small dip around $x = 15$, leading to three positions where no actuation force is generated.

More pole surface area leads to more total flux, but the flux density can can go down. The normal force plot in B.17b indicates that flux density has an optimum: normal force peaks at 2x10mm teeth before decreasing.

B.5. Yoke material

A material sweep investigates the effect of lower yoke saturation on cogging and the discovered base cogging. Current sweeps were done with materials having various levels of saturation flux density. Their DC magnetisation curves are shown in figure B.22.

Cogging

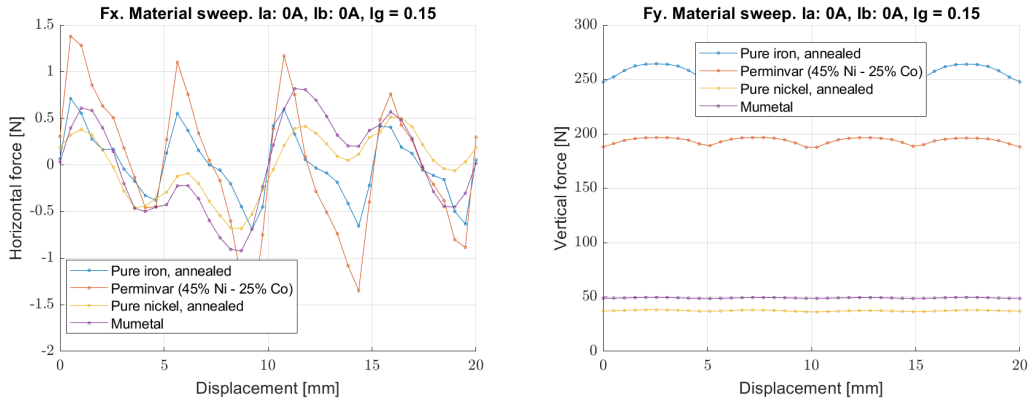

(a) Actuation Force.

(b) Normal force.

Figure B.19: Cogging for different material models.

Figure B.19 shows that a lower maximum saturation of the material leads to a higher cogging for the same magnet size. With a lower saturation density the flux will fringe around the air gaps earlier, leading to larger changes in magnetic coenergy, even though the total energy in the system is lower. Figure B.20 shows that if the saturation density of the forcer material gets too low, the flux fringes so much that $\partial E/\partial x$ will decrease. When that happens the reluctance of the yoke and platen material becomes dominant, showing as an extra influence on the actuation force.

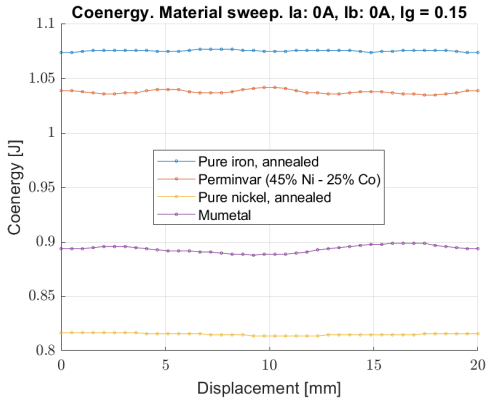

Figure B.20: Coenergy in material model sweep without power.

0.3A on coil B

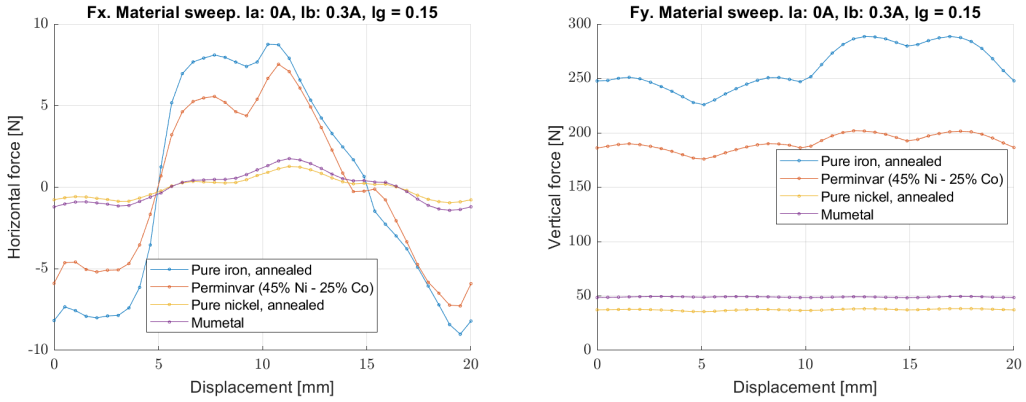

(a) Actuation Force.

(b) Normal force.

Figure B.21: Actuation force for different material models. Higher saturation material generates higher acuation force.

Actuation force directly relates to how much flux can pass through the yoke material. Hence, the highest material saturation leads to the highest actuation force. The electrical energy can be converted to magnetic energy more efficiently. The lower saturation density of perminvar makes more flux fringe around the teeth for the same PM size, leading to stronger cogging harmonics in the acutation force. When the saturation density gets very low, magnetic energy remains constant and very little force is generated.

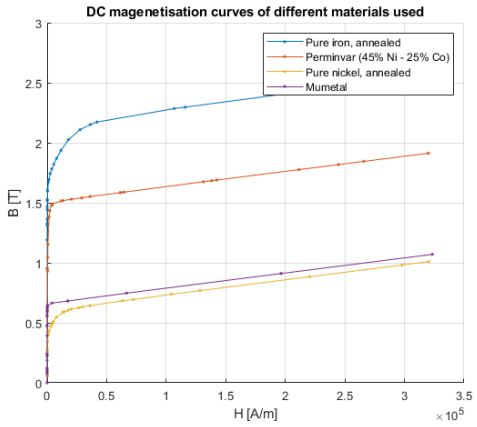

Figure B.22: Magnetisation curves of material models used.

C

FEA tooth shape data

This sections contains all the plots about tooth shape sweeps done using the FEMM 4.2 software. A current sweep was done with each tooth shape for $I_b = 0..3$A. The horizontal (actuation/cogging) and normal forces of each tooth shape are displayed side by side. Square teeth are taken as the baseline to which all teeth shapes are compared.

Square teeth

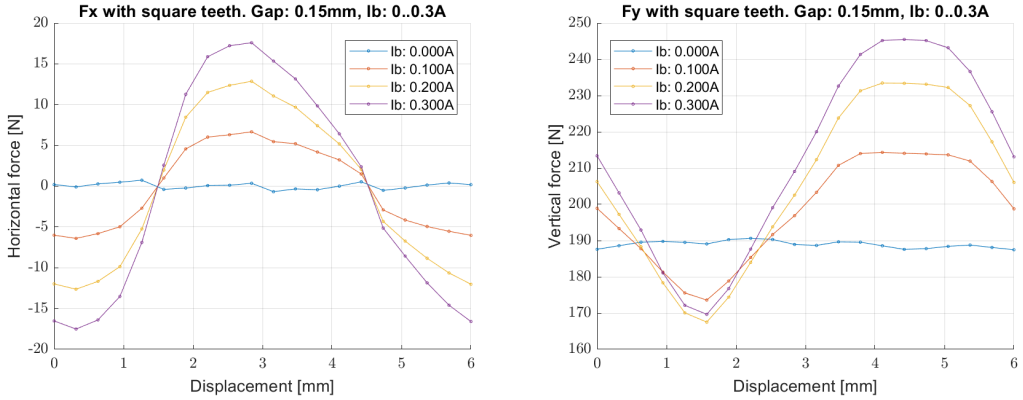

(a) Actuation force.

(b) Normal force.

Figure C.1: Actuation and normal force of square teeth for several currents. Square teeth serve as the basis to which all other teeth shapes are compared.

Square teeth serve as the basis to which other teeth shapes are compared. As could be seen in the parameter sweeps, the force/displacement curve is not entirely sinusoidal as described by Pelta [14], but shows a flattened bulge. This could be caused by saturation of the teeth, or the difference in flux path lengths of the poles 1 & 4 vs 1 & 3. Square teeth show the highest actuation force stiffness and the highest normal force of all tooth shapes.

Filleted teeth

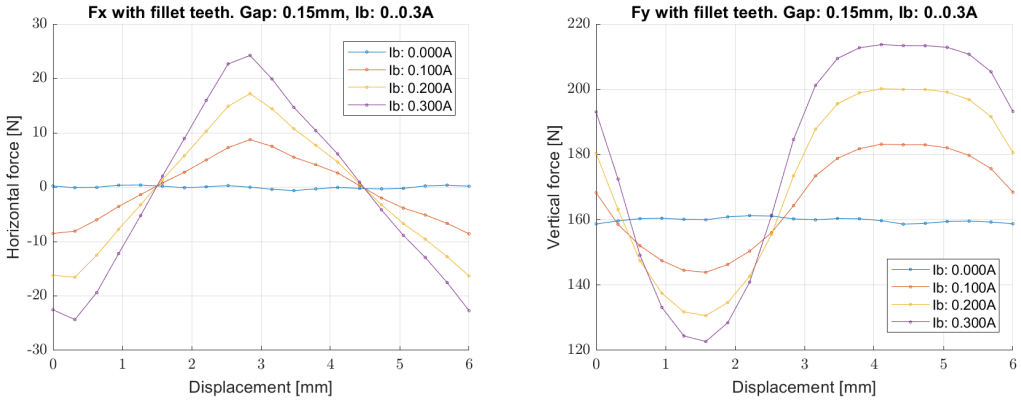

(a) Actuation force.

(b) Normal force.

Figure C.2: Actuation and normal force of filleted teeth for several currents. Filleted teeth show a significantly higher actuation force.

These dimensions of filleted teeth show almost zero cogging, and a significantly higher actuation force, at a reduced normal force and stiffness. The force/displacement curve is mostly linear and symmetric. Work done by the actuation force is higher, leading to the highest power density of all tooth shapes by a margin. The downside of this tooth shape is the high change in normal force, which might induce vibrations in the system during motion.

Trapezium shaped teeth

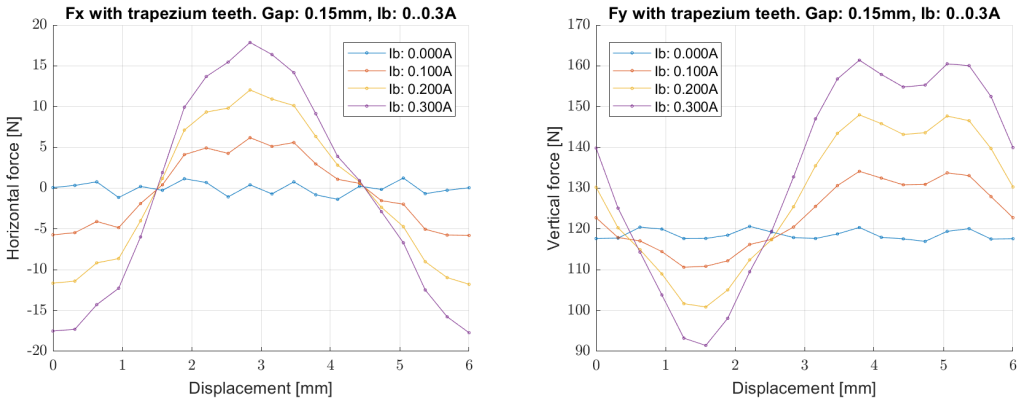

(a) Actuation force.

(b) Normal force.

Figure C.3: Actuation and normal force of trapezoidal teeth for several currents. Trapezoidal teeth indeed show a lower normal force as described by [17].

Trepezoidal teeth generate the same peak actuation force as square teeth, but with a significantly lower normal force. This agrees with the results mentioned by Szabo and Viorel in *Hybrid Linear Stepper Motors*, p.27 [17]. However, the stiffness and power density are slightly lower. Cogging peak force is significantly higher, but the shape of the cogging force looks irregular, which could be problematic for the filter wheel application. The chamfer angle and top width most likely play a significant part in shaping the force /displacement curve.

Triangular teeth

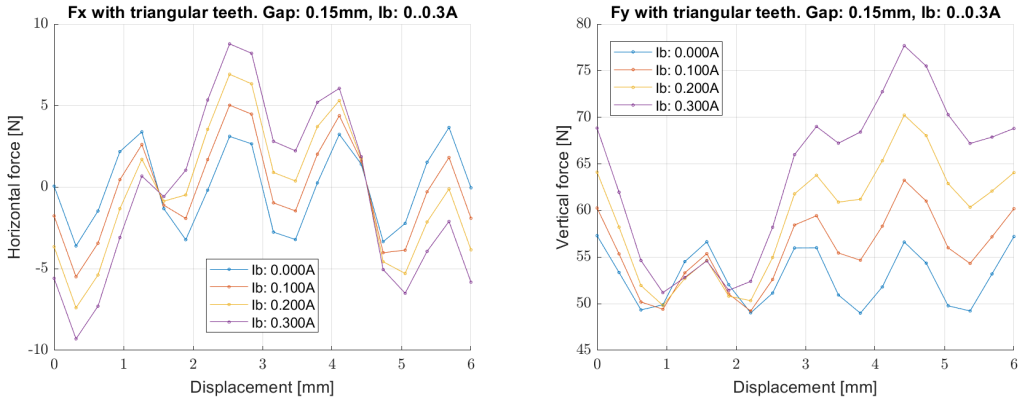

(a) Actuation force. (b) Normal force.

Figure C.4: Actuation and normal force of triangular teeth for several currents. Triangular teeth show very high cogging and low normal force.

Triangular teeth generate the highest cogging force by far, with a peak amplitude of 5 times that of square teeth. Because of the smaller amount of material volume, the actuation force under power is low as well, with a distinct cogging harmonic shown through. Because the total flux flowing is lower, the normal force is also much lower. The filter wheel concept requires only a small actuation force and a relatively high cogging force. Triangular teeth seem to be suitable for this, and the reduced normal force will mean a long life for the central bearing.

Round teeth

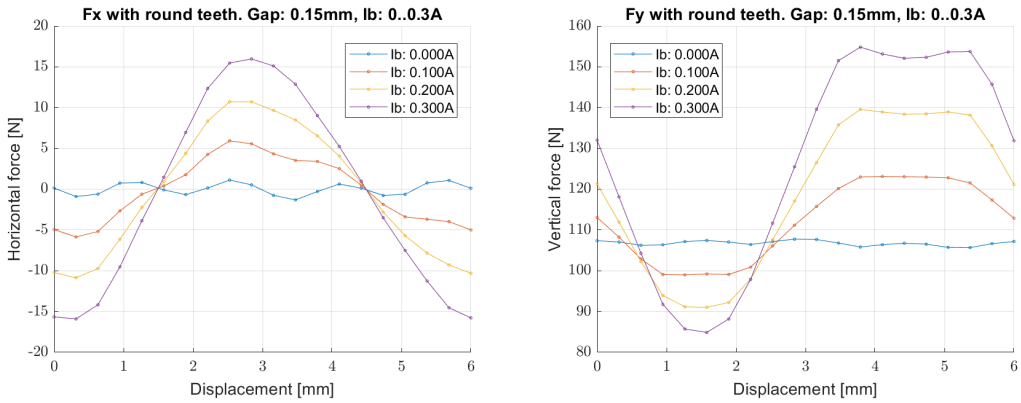

(a) Actuation force (b) Normal force.

Figure C.5: Actuation and normal force of round teeth for several currents. Round teeth show partly linear Fx/x and medium cogging.

Round teeth show higher, smooth cogging and a reasonably high actuation force, with a significantly lower normal force. The Fx/x is linear and appears very smooth, which would lead to a low torque ripple design. This tooth shape could be an good candidate for an easy to control system that does require medium strong cogging force.

Inverse filleted teeth

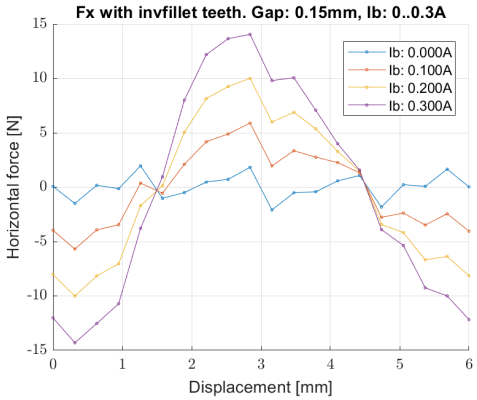

Figure C.6: Actuation force.

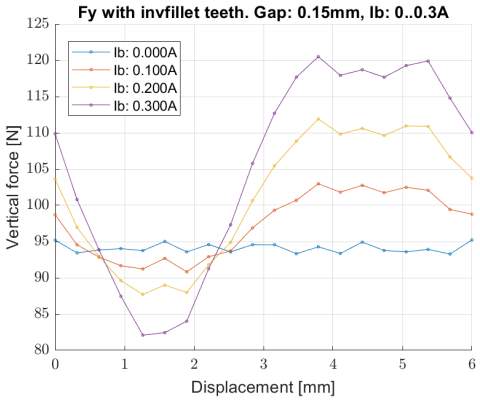

Figure C.7: Normal force.

Figure C.8: Actuation and normal force of inverse filleted teeth for several currents. This tooth geometry leads to cogging with extra harmonics. The cogging force's stable stiffness is very high.

Inverse filleted teeth show similar behaviour as trapezoidal teeth, but with a different harmonic in the cogging. The peak amplitude of cogging is higher, supporting the theory that a faster changing air gap distance increases the cogging amplitude. The non-continuous profile of the tooth likely contributes to the erratic cogging behaviour shown.

C.1. Filleted teeth actuation force

Figures C.9 show actuation force with 0.3A on coil B for several top widths (=fillet radius).

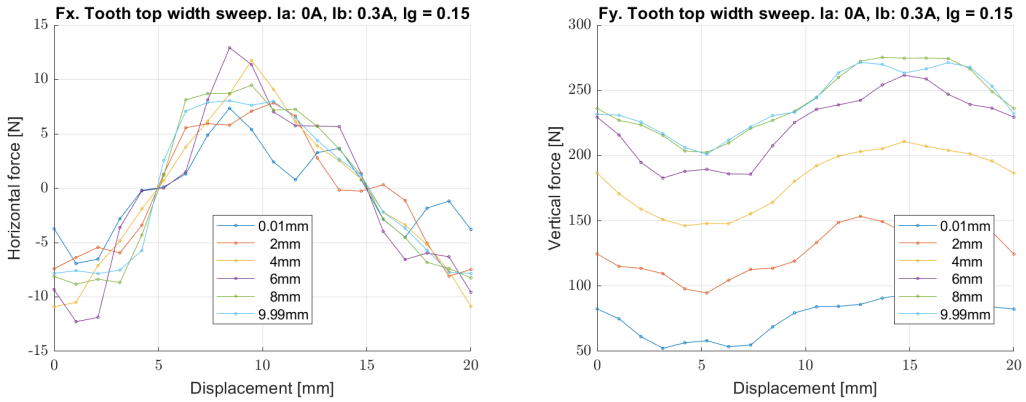

(a) Actuation force for different top widths of filleted teeth at 0.3A. (b) Normal force for different top widths of filleted teeth at 0.3A

Figure C.9: Actuation force has an optimum for top width of filleted teeth. Some top widths lead to a completely linear Fx/x.

The force output of filleted teeth is highly sensitive to fillet radius.

C.2. Metrics of different tooth shapes

These metrics are calculated from the sweep data shown in section C. The metrics serve to quantify the difference between the tooth shapes.

Cogging metrics of different tooth shapes

	Peak FX [N]	FX work done [J]	Peak FY [N]	P2p FY [N]	Stable stiffness [N/m]	Unstable stiffness [N/m]	FXwork/volume [J/m3]
Square	0.7353	0.001919	190.6	3.177	3750	1775	5
Trapezium	1.249	0.003725	120.6	3.672	6393	5363	10
Fillet	0.3992	0.001387	161.3	2.61	1290	1436	3.5
Inverse fillet	1.966	0.005064	95.23	1.951	13069	7006	13.6
Round	1.124	0.00367	107.8	2.075	4272	4676	9.8.
triangular	3.662	0.01286	57.3	8.316	18043	12507	34.5

Table C.1: Table with cogging metrics of the different tooth shapes.

The peak cogging force of triangular teeth is 5 times that of square teeth. The stiffness of the cogging for triangular teeth is also much higher than all other teeth. This will increase the repeatability and stability of the filter wheel's motions.

Filleted teeth show an unusually low cogging. This makes these teeth interesting for applications that need smooth motion instead of cogging.

0.3A metrics of different tooth shapes

	Peak FX [N]	FX work done [mJ]	Peak FY [N]	P2p FY [N]	Stable stiffness [N/m]	Unstable stiffness [N/m]	FXwork/volume [J/m3]
Square	17.59	0.07178	245.5	75.85	2.51E+04	3.16e+04	179.4
Trapezium	17.88	0.06788	161.4	69.97	1.93e+04	2.67E+4	168.18
Fillet	24.24	0.08275	213.7	91.01	1.74E+04	2.43E+04	204.11
Inverse fillet	14.05	0.05263	120.5	38.41	1.82E+04	2.35E+04	131.6
Round	15.97	0.06215	154.8	69.97	1.49E+04	1.89E+04	154.3
triangular	8.786	0.02745	77.69	26.5	2.31E+04	1.44E+04	69

Table C.2: Table with metrics for the different tooth shapes at 0.3A on coil B.

Filleted teeth also how a 14% higher peak actuation force and power density than square teeth. The Fx/x is completely linear for this tooth geometry. Stiffness of the acutation force is considerably lower than that of square teeth. The normal force of filleted teeth has a much higher peak to peak value, which will put extra stress on the bearing system.

Triangular teeth also have high actuation force stiffness, but the force/displacement characteristic shows extra points where $Fx = 0$, which is undesireable. For a slightly lower MMF ratio, triangular teeth might offer the same actuation force stiffness as square teeth, but with much higher cogging stiffness.

Overall triangular teeth show the best metrics for our application, while filleted teeth are highly promising for use in other applications.

D

Breadboard testing and measurement plan

D.1. Photos of breadboard

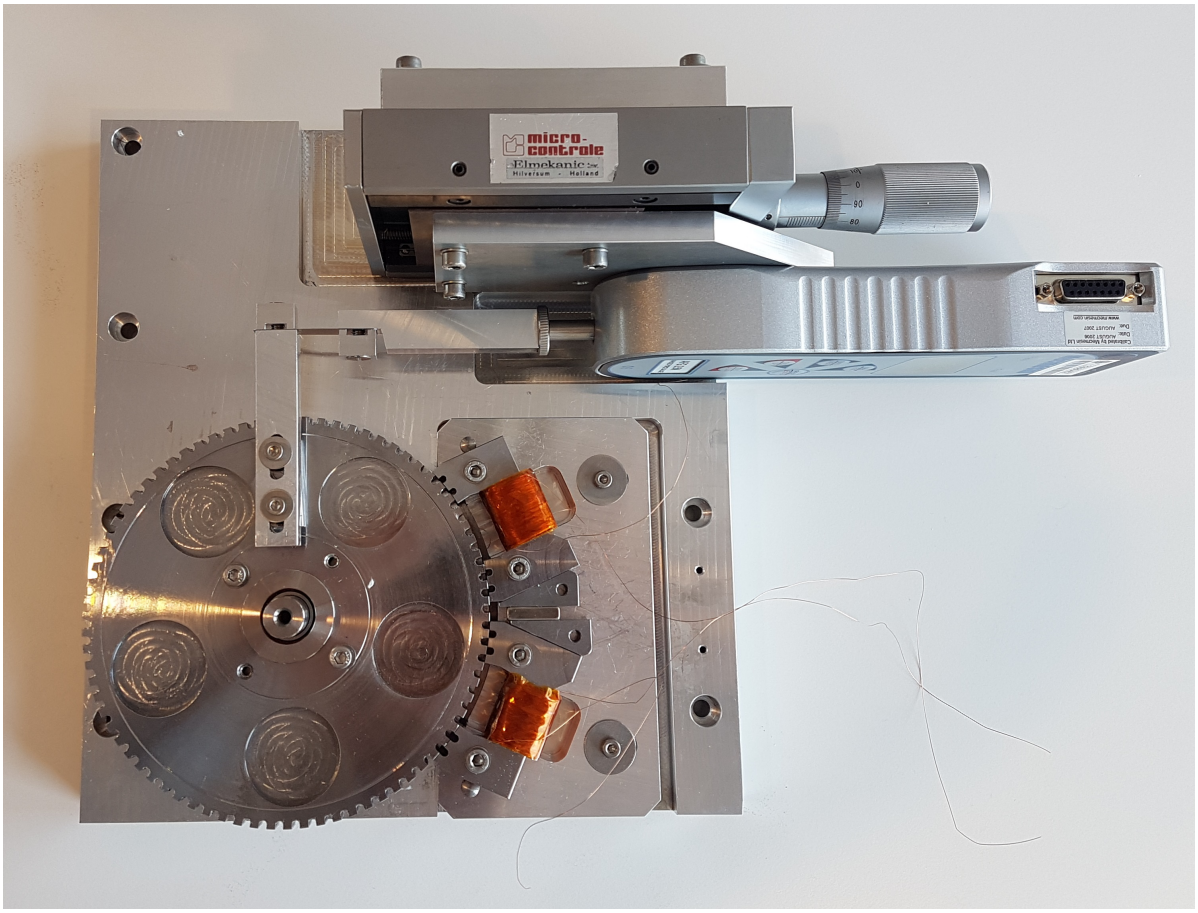

Figure D.1: The breadboard including force probe (2).

D.2. Design of the breadboard

The leading design choice for the breadboard is to manufacture in house, making use of TNO's CNC milling and coil winding machines. This put constraints on the materials and shapes used in the design. The main design considerations are listed below:

- **The breadboard will be a '2D' design**
  This is the most similar to the analytical model and FEA, so makes for the best comparison. It is also easiest to manufacture.
- **The system will have one 2D forcer similar to the FEA model**
  This allows us to easily adjust air gap distance. The potentially high normal force will be in the same direction.
- **Square teeth**
  The default tooth shape used in industry. The analytical model only deals with constant air gap length. Comparison is only possible with square teeth.
- **Measure torque at the rotor, not at the forcer**
  Measuring torque at the rotor means we can construct our force/displacement graph using only one sensor. Additionally it allows a rigid connection between forcer and housing. This greatly simplifies the design.
- **Measure actuation force using a probe connected to the rotor with a flexure**
  A flexure allows the a probe to measure both compression and extension, which results in the simplest possible setup. The flexure should be so thin as not to exert parasitic forces, but thick enough not to buckle under compression. Its stiffness is an order of magnitude above the expected motor stiffness.
- **Over dimensioned magnet and coils**
  To investigate behaviour under saturation, the magnet and coils should be big enough to saturate the forcer teeth.
- **Relatively large teeth**
  While this may decrease the power density, it reduces relative manufacturing errors. Large teeth also have a higher cogging force, making this easier to measure.

D.3. Dimensions of the breadboard

The dimensions chosen are the same as used in the tooth shape sweep to allow comparison of results.

- **Air gap 0.15mm**
  With a proper bearing system 0.15mm should be easy to achieve. The magnet height sweep in figure B.3 shows that with this air gap cogging will be of measureable magnitude.
- **3x3mm teeth**
  As small as is easily milled, but still large for an electric motor. For the same manufacturing process, larger teeth have a lower relative dimensional error. Figure B.5 shows that teeth 3mm wide teeth should be large enough to generate cogging at this air gap.
- **10mm thick system**
  The 2D FEA simulation assumes a system of infinite thickness. To reduce out of plane effects, the breadboard's thickness should be much higher than the tooth width.
- **Max current 0.3A**
  Determined by wire diameter compatible with coil winding machines present at TNO.
- **1600 windings**
  For the rated maximum current, 1600 windings are enough to saturate the air gap. Big coils allow testing many different PM/coil MMF ratios.
- **Magnet surface area 20x10mm. 5mm long**
  This is big enough to saturate the air gap. Figure B.3 shows that a minimum surface area of 15x10mm is needed to generate cogging.
- **Flexure of 10x15x0.2mm**
  The flexure has been designed to be an order of magnitude stiffer than the expected actuation and cogging forces. Its buckling load is twice the expected motor output.

D.4. Fitting the analytical model to breadboard results

The amplitude of the sine reluctance model of chapter A was fit to the measurement data. The standard reciprocal-of-overlap model was left out of this plot because it yielded an unstable motor characteristic and a maximum force output of 23N.

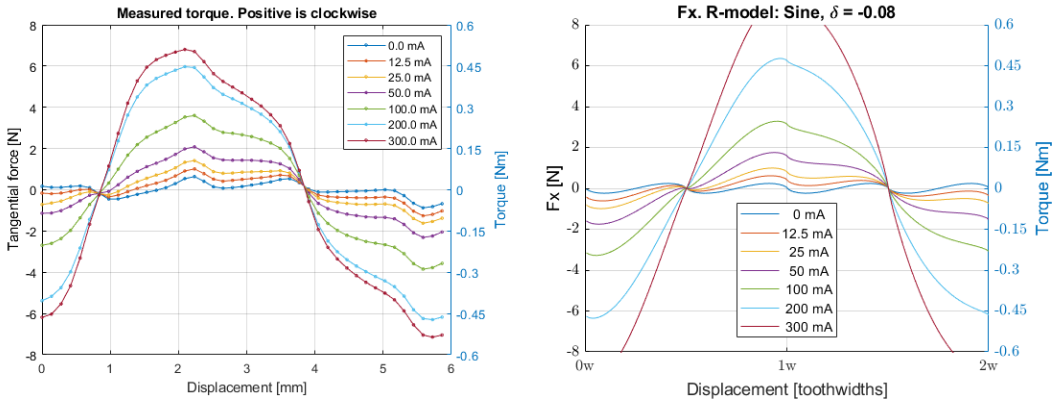

(a) Measured breadboard output.

(b) Analytical model fit to measurement data.

Figure D.2: Breadboard results together with a sine-reluctance model. Reluctance in the model varies between 1..2 times the value of $l_g/(\mu_0 A)$. $\delta = -0.08$. The magnitude of forces corresponds well until saturation.

Even though the sine-reluctance model is based on an assumed reluctance profile, when fit it is a much better predictor for breadboard output than the reciprocal-of-overlap model. A model like this can serve to estimate design parameters, to be validated with FEA before creating a prototype.

E

Measurement plan

The measurement plan is made in Dutch.

ONTWIKKEL EN MEETPLAN

INTRODUCTIE

Dit document is een handleiding voor het meten van de output van het filterwiel breadboard. Er zijn verschillende ontwikkelstadia van het breadboard, waarmee we telkens meer te weten komen over de motorkarakteristiek. De verschillende opstellingen staan in tabel 1.

TABEL 1: VERSCHILLENDE BREADBOARDOPSTELLINGEN

Opstelling	**Beschrijving**
1 Cogging	Met alleen het breadboard kan de cogging gemeten worden. Er is geen extra hardware nodig. Het uitlezen van de force gauge zou handmatig kunnen.
2 Vaste current met labvoeding	Met een labvoeding kunnen we een vaste stroomsterkte op 1 spoel zetten. Hiermee kunnen we snel een F/x curve meten die de werking van het prototype bevestigd. Het uitlezen van de force gauge zou handmatig kunnen. Dit kan eventueel herhaald worden voor verschillende stroomsterktes.
3 Digital current control met lineaire versterkers	Door met matlab/dSpace twee lineaire versterkers aan te sturen kunnen we voor elke rotorpositie een current sweep doen over beide coils. We hebben dan voor elke rotorpositie een 3D tabel met stroomsterktes en koppel. Dit is voor dit breadboard de meest complete set gegevens over de werking van de motor. Het uitlezen van de force gauge moet met Matlab.
4 Stappend in open loop	Een eerste open loop control implementatie kan met een druk op de knop de motor één stap verder- of terugdraaien. De grootte van de stroom kan dan constant zijn en kan extern geregeld worden.
5 Draaiend in open loop	Een signaalgenerator kan ofwel twee sinussen, ofwel twee stair waves genereren met een 90° faseverschil. Hiermee kunnen we de rotor laten draaien. Een druk op de knop verandert het faseverschil naar -90°, zodat de motor de andere kant op begint te draaien. Snelheid en amplitude kunnen digitaal worden ingesteld.
6 Stappend en draaiend in open loop	Een basic GUI met 4 knoppen en twee sliders • Stap naar links • Stap naar rechts • Draai naar links • Draai naar rechts • Stroomsterkte • Draaisnelheid Dit zal een dSpace programma zijn met knoppen. Dit geeft de beste demonstratie.
7 Repeatability	Een spiegel op de rotor gemonteerd en een statische laser laat ons de hoek van de rotor precies meten.

BENODIGDHEDEN

Opstelling	1	2	3	4	5	6	7
Geassembleerd breadboard							
Mecmesin BFG Force gauge 2.5, 50 of 500							
Force gauge adapter plaat							
Force gauge kabel							
Arm met flexure							
Elmekanic Micrometer controle stage							
L beugel voor micrometerstage							
Magneten met verschillende sterktes							
DC Labvoeding rated 1A							
2x lineaire versterker rated 1.5A							
Matlab interface force gauge							
Simulink state space model							
Simulink double sine output met faseverschil knop							
GUI met knoppen							
Spiegel, laser en montageplatform							

OPSTELLINGEN 1-3

Het breadboard is ontworpen met een Elmekanic Micrometer Controle stage, eigendom van TNO. Deze kan op het breadboard geschroefd worden met een L beugel. Met een adapter plaat is een Mecmesin BFG2.5/50/500 trekmeter op de stage te schroeven. Om de cogging te meten kunnen we de BFG2.5 nemen. Voor de krachtmetingen is de 50N geschikt. Via een flexure verbinding kan de rotor aan de trekmeter worden geschroefd. Schroef eerst de flexure verbinding aan de force gauge, zet het stage op 18.625mm en schroef de flexure arm aan de rotor. Zorg dat tijdens dit proces de trekmeter 0 Newton meet. De neutrale stand van het stage maakt an sich niet uit, als er maar +-4mm naar beide kanten kan worden bewogen.
Een blokmagneet zit tussen de twee kernen geschoven. Door de aantrekkingskracht blijft deze zitten. We kunnen de magneet verder, of minder ver in het gat schuiven om verschillende combinaties saturatie + phib/phib te testen.

Het breadboard is ontworpen op een air gap van 0.15mm, maar de uiteindelijke gap hangt af van de productie toleranties. De forcer kan los worden gemaakt en opnieuw worden gesteld met dikkere shims. Zo kunnen we motorgedrag bij een andere air gap testen.

In deze en elke andere opstelling zou de permanente magneetkracht kunnen worden gevarieerd door een andere PM te gebruiken, of de magneet tussen de kernen uit te schuiven.

OPSTELLINGEN 5-6

Voor stappend gedrag zou een krachtmeting nog wel interessant kunnen zijn. De rotor moet vrij kunnen draaien, dus de flexure arm aan de rotor moet sowieso los. De hele meetopstelling van stage, force meter en flexure arm kan het beste van de base worden gehaald.

OPSTELLING 7

Hiervoor moet een dop met spiegelmount worden geschroeft op de rotor. Daarvoor kunnen we 2/4 M5 gaten gebruiken. Op de mount schroeven we een spiegel. Aan de optische tafel wordt een laser bevestigd. Deze opstelling wordt gebruik om de hoek van de rotor exact te meten.

EEN METING DOEN

Met de micrometer schroef draaien we de rotor van -2.5°…+2.5° met een aantal stapjes. Voor elke rotorstand lezen we de krachtmeter af en lezen we het stroomverbruik en het voltage van de versterker af. Daarna draaien we in stapjes weer terug, en lezen we op elke stap weer de krachtmeter en versterker af.

We meten -2.5°…+2.5° rotatie van de rotor om 1 periode te meten. In die periode is pool 1 compleet in fase, uit fase en weer in fase gekomen. De flexure buigt dus ook -2.5°…+2.5°. Een grotere buiging kan, maar dan wordt de parasitaire kracht op de force gauge ook groter. De minimaal benodigde meetrange om het systeem te karakteriseren is een halve periode, vanwege de symmetrie van de beweging. Omdat de parasitaire kracht niet zo groot is (<1N) vergeleken met de actuatiekracht is het niet heel kritisch. Voor een cogging meting zou het eventueel interessant zijn.
De gekozen rotatie correspondeert met een verplaatsing van 7.2mm van de force gauge. Beginstand -2.5° is 15mm, 0° = 18.625mm, eindstand op +2.5° is 22.24mm. De exacte standen hangen af van hoe de flexure arm aan de rotor is geschroefd, en op welke stand de stage toen stond. Voor het doen van de meting is het erg handig dat de micrometer op een heel getal staat.

PERFORMANCE METRICS

Een aantal metrics zullen worden moeten worden berekent voor elke meting. Hiermee kan het motorconcept worden gekarakteriseerd. De verwachte waarden in groen gearceerd komen uit de FEA studie. De andere metrics zijn berekend op basis van het analytische model. Het uitgangspunt van de verwachte waarden is bij een 0.15mm air gap en 0.3A stroomsterkte.

Metric	**Toelichting**	**Verwachting**
Peak force and τ/θ curve without power	Maximale amplitude en vorm+periode van de τ/θ grafiek zonder stroom.	A = 0.8N, periode is 1/4^{e} pitch. Sinusvormig. Amplitude fluctuaties correleren met verschillende air gaps voor de 4 polen.
Peak force	Maximale amplitude τ/θ curve. Piekkracht ligt links van de plek waar pool 1 in fase komt.	17N. Peak force neemt lineair toe met stroomsterkte.
FXwork done between x = 0..2w	Integreer koppel over de afgelegde rotatie.	74mJ. Geleverde arbeid neemt toe met stroomsterkte.
Jerk around x = w/2	Sprong in koppel rond stabiele neutrale punt bij θ =w/2.	Jerk is afwezig, behalve in extreme gevallen waar de motor zelf niet bruikbaar is.
Stiffness around stable neutral point	Helling van de τ/θ curve rond stabiele neutrale punt onder stroom.	28kN/m. Stijfheid van cogging neemt af met grotere air gap. Neemt toe met magneetsterkte en stroomsterkte
Stiffness around unstable neutral point	Helling van de τ/θ curve rond instabiele neutrale punt onder stroom.	32 kN/m. Neemt toe met magneet- en stroomsterkte.
Electrical power dissipation static	Sommeer I*U wat de versterker levert over 1 periode bij statische kracht meting.	3.7 Watt. Power dissipatie neemt linear toe met stroomsterkte.
Electrical power dissipation dynamic	Voor verschillende steady state toerentallen meten we het gemiddelde stroomverbruik voor 20 seconden.	13W voor 60RPM. 41V 0.3A Opgenomen vermogen neemt toe met toerental, omdat eddy currents voor verliezen gaan zorgen en omdat er hogere piekspanningen ontstaan.
Efficiency: FXwork/Watt (avg)	Arbeid geleverd door motor in 1 periode, gedeeld door elektrisch vermogen.	1.95 cJ/Watt. Het grootste deel van de arbeid wordt geleverd rond het instabiele neutrale punt.
Force density: Newton/volume Newton(avg)/volume	Piekkracht gedeeld door volume van kernen.	497.000N/m3, of 0.5N/cm3
Power density: Fxwork/volume	Arbeid geleverd door de horizontale kracht delen door het volume van de kernen+spoel+magneet. Het volume wordt berekent met solidworks.	975J/m3
Repeatability	Gemiddelde, maximale en standaarddeviatie van de afwijking van echte positie t.o.v. doelpositie.	Max = 0.2 graden

Metingen

Er zijn een aantal metingen waarmee we de motor kunnen karakteriseren. Voor elke meting kunnen we de metrics berekenen.

Meting	**Toelichting en verwachting.**
1: Cogging	Het doel van de meting is om de cogging te bewijzen en te karakteriseren. We meten de vorm en magnitude van de τ/θ curve zonder stroom. Verwachting: Bij het doorlopen van 1 periode verwachten we 4 sinusperiodes te zien, corresponderend met de 4 polen die om de beurt met een tand uitlijnen. Resultaat: 3 tabellen met X-as posities en Y-as kracht. Elke tabel is met een andere magneetsterkte.
2: Koppel simpel	Het doel van de meting is het operating principle te bewijzen, door een eerste τ/θ curve te tekenen. Verwachting: We verwachten in 1 periode 1 sinusvormige grafiek te zien. Resultaat: tabel met X-as posities en Y-as kracht; een schatting van het gemiddelde voltage.
3: Koppel sweep	Het doel van de meting is om het effect van stroomsterkte op de aandrijfkracht te testen. Dit doen we door een τ/θ curve te tekenen voor verschillende stroomsterktes. Verwachting: Bij het doorlopen van 1 periode verwachten we 1 sinusvormige grafiek te zien, waarvan de amplitude lineair toeneemt met stroomsterkte. Resultaat: Voor elke stroomsterkte een tabel met op de X-as posities en Y-as kracht. Op de Z as staat voltage.
4: Repeatability	Het doel is om te onderzoeken hoe precies de rotor in een bepaalde stand kan worden gepositioneerd. Als blijkt dat de repeatability afhangt van het afgelegde aantal stapjes kunnen we een plot maken met op de X as aantal stappen, en op de Y as de error. Verwachting: iets rond de 0.2 graden. Resultaat: tabel met 30 metingen met verschillende afgelegde afstanden en een error waarden.
5: Snelheid en stroomverbruik	Doel is om een indruk te krijgen hoe makkelijk hoge toerentallen zijn te halen en hoeveel stroom dat kost. Dit doen we door de een steeds sneller sinusvormig en blokgolf signaal op de spoelen te zetten, tot aan de maximale rating van de versterkers. Door het aanstuurvoltage te meten voor verschillende snelheden kunnen we ook het energieverbruik berekenen. Verwachting: De spanning die de versterker kan leveren bepaalt waarschijnlijk het maximale toerental. Dat zal rond de 20W zijn. Stappend stroomverbruik zal rond de 4W liggen. Resultaat: tabel met 10 verschillende snelheden en hun gemiddelde stroomverbruik over 20 seconden.
6: Hoge I/hc ratio	Doel is om te kijken wat een hoge stroom/magneet fluxratio doet. Omdat de spoel niet meer MMF kan leveren, zullen we deze meting met kleinere magneten moeten doen. Verwachting: τ/θ wordt deels lineair. Voor kleine magneetsterktes zou er een omkering kunnen plaatsvinden rond het punt waar de horizontale kracht 0 is. Resultaat: Twee tabellen met op de X-as posities en Y-as kracht. Deze meting wordt gedaan met **kleine** magneten.
6: lage I/hc ratio	Doel is om te kijken of de τ/θ curve meer blokgolvig wordt bij een hoge magneet/stroom fluxratio. Verwachting: Mogelijk hogere stijfheid rond stabiele neutrale punten. Een duidelijke sprong in kracht rond het stabiele neutrale punt. Gekke vorm van τ/θ curve. Resultaat: Voor twee magneetsterktes een tabel met op de X-as posities en Y-as kracht. Deze meting wordt gedaan met **grote** magneten.
7: Effect van air gap.	Doel is om te kijken wat de invloed van air gaps is op de sterkte van de cogging en aandrijfkracht, en wat de invloed is van polen en tanden die niet goed in fase staan. Hiervoor worden metingen 1 en 3 opnieuw gedaan op air gaps 0.3mm en 0.45mm. Bij beide metingen staan de polen en tanden niet meer goed uitgelijnd, dus de vorm van de τ/θ curve zal gaan veranderen. Resultaat: Twee tabellen met op de X-as posities en Y-as kracht. Op de Z-as voltage.

UITVOEREN VAN DE METINGEN

METING 1: COGGING

a. Lijn tanden van spoel uit op juiste positie met micrometer schroef. Tanden van pool 1 zouden moeten uitlijnen op -2.5° rotatie van de rotor t.o.v. neutraal.
b. Noteer waarde krachtmeter.
c. Draai aan micrometer schroef totdat de rotor in de volgende positie staat.
d. Herhaal b-c totdat rotor op +2.5° staat.
e. Draai de verplaatsing om en meet weer met gekozen stapgrootte op het interval +2.5° …-2.5°.
f. Plaats magneet met sterkte 2 tussen de kernen en doorloop een nieuwe meetcyclus.

METING 2: BEWIJS AANDRIJFPRINCIPE

a. Lijn tanden van pool 1 uit met micrometer schroef.
b. Sluit labvoeding aan op spoel B en zet stroomsterkte op maximale stroom 0.3A.
c. Noteer waarde krachtmeter. Werp een blik op labvoeding en onthoud voltage.
d. Draai aan micrometer schroef totdat de rotor in de volgende positie staat.
e. Herhaal c-d totdat de rotor op +2.5° staat.
f. Draai de verplaatsing om en meet weer met gekozen stapgrootte op het interval +2.5…-2.5 graden.
g. (Plaats magneet met sterkte 2 tussen de kernen en doorloop een nieuwe meetcyclus.)
h. (Zet labvoeding op andere stroomsterkte en herhaal meetcyclus).

METING 3: EFFECT VAN STROOMSTERKTE OP AANDRIJFKRACHT

a. Lijn tanden van pool 1 uit met micrometer schroef.
b. Geef Matlab het sein voor een current sweep van beide coils. Bij elke stroomcombinatie wordt de waarde van de krachtmeter uitgelezen en de stroomsterkte en het voltage genoteerd.
c. Draai aan micrometer schroef totdat de rotor in de volgende positie staat.
d. Herhaal b-c totdat de rotor op +2.5° staat.
e. Draai de verplaatsing om en meet weer met gekozen stapgrootte op het interval +2.5° …-2.5°.

METING 4: REPEATABILITY

a. Zet de rotor in een willekeurige stand.
b. Noteer positie rotor.
c. Geef opdracht voor een x aantal stappen naar links, gevolgd door een x aanstal stappen naar rechts.
d. Noteer positie rotor.
e. Herhaal c-d met verschillende x en langere sequenties stappen.
f. Bereken de error tussen de begin- en eindpositie van de rotor.

METING 5: SNELHEID

a. Laat rotor draaien op constante snelheid die ingesteld is in dSpace.
b. Meet het opgenomen vermogen gedurende 20 seconden.
c. Verhaal a-b voor 1,2,5,10,20,30,60 rpm.

METING 6: HOGE I/HC RATIO

Herhaal meting 3, met een ¼ grootte magneet tussen de kernen geschoven.

METING 6: HOGE HC/I RATIO

Herhaal meting 3 met zoveel mogelijk magneet tussen de kernen geschoven.

METING 7: EFFECT VAN AIR GAPS

Een herhaling van metingen 1 en 3 met 2 verschillende air gaps. Hiervoor moet de forcer los worden geschroefd, en op en op een andere air gap weer worden vastgeschroefd. De uiteindelijke gap is afhankelijk van hoe het breadboard uit de werkplaats komt.